博士論文（要約）

Theoretical investigation on

surface/interface optimization and property analysis of

novel 2D materials

(新奇 2 次元材料の

表面／界面最適化と物性解析に関する理論研究)

ニ　タクオン
倪　澤遠

Ni Zeyuan (倪泽远)

Department of Materials Engineering

The University of Tokyo

May 2017

Table of Contents

1. Introduction

1.1. Two dimensional materials beyond graphene

1.1.1. Overview

As a "golden rule" that has dominated information technology revolution since the 1960s, Moore's law rules that the number of transistors per integrated circuit, usually as well as the speed of a microprocessor chip, will double every 18 months (Figure 1-1).[1] Unfortunately, such doubling starts to be harder and harder as the size of transistor is reaching the physical limit of several nanometers. With the traditional silicon technology, heat dissipation becomes a large problem due to the higher density of transistor per area,[1] as well as the current leakage due to the inefficient ability of switching off the current with ultrashort channels. The central problem is that

Figure 1-1: Moore's law for the transistors per microchip and the 'clock speed' (rate of executing instructions) of chips. The latter one continued until 2004, when the speed has to be limited to lower the heat dissipation. The former one is struggling to continue but facing several severe challenges from nano-scale quantum mechanics. From Ref.1.

classical transport theory no longer applies in such a nano-realm. Instead, electrons' behavior is governed by quantum mechanics, where the tunneling behavior contributes a lot to the current leakage. That's why the world faces the crisis of the cease in the Moore's law in the past decade, whose impact is way beyond simply the slow-down of the exponential increase in the number of transistors per area.

Two ways are being pursued to rejuvenate the scaling of transistors: using either novel device scheme or novel channel materials. The former way uses alternative device structures, such as fin, gate-all-around (GAA) and ultrathin Si on insulator (UTSOI) FETs,[2-4] to improve gating ability and thus the performance of traditional silicon microelectronics. The latter way try to replace the traditional silicon channel material by other materials with higher performance on some aspects, such as graphene, MoS_2, and phosphorene.[5-7] It is one of the most important stimulations for the spawn of novel layered materials in recent years, for layered materials are believed to have less harmful short-channel effects and higher controllability by gate due to their reduced dimension.[8]

Layered materials have existed for ages, but not until the synthesis of graphene, the first 2D material, have researchers noticed the true potential of them. [5,9] At the physical limit of thickness, the atomically thin 2D graphene exhibits various exotic properties, for example the ultrahigh mobility of $10^4 \sim 10^5$ cm^2/(Vs) in experiment compared to $10^2 \sim 10^3$ cm^2/(Vs) in silicon (Figure 1-4).[10] The electron transport of graphene can be described by the Dirac's equation with zero rest mass and a fermi velocity of $c \sim 10^6$
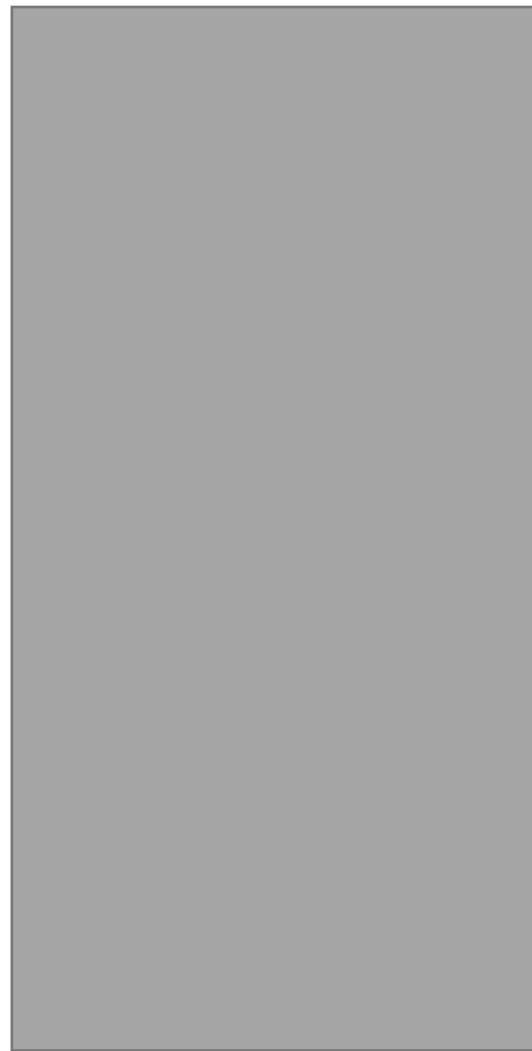
Figure 1-2: (a) 2D materials beyond graphene; (b) Publications of 2D materials over time. Novel 2D materials are gaining more and more global attention from 2011. From Ref. 9.

m/s. In that way, the carriers in graphene are named after massless Dirac fermions.[11] Furthermore, the electronic structure of graphene is topologically distinct from traditional band insulator due to the presence of time-reversal symmetry and the gap opened by spin-orbit coupling.[12–15] That is to say, the band structure of graphene cannot be adiabatically connected to those of band insulators or vacuum, and hence graphene is the representative of a new family of materials called topological insulators with non-trivial topological invariant (Z_2 invariant).[12] The edge states in graphene will exhibit an exotic property that electrons with opposite

Figure 1-4: Comparison of carrier mobility and band gap of graphene sheets, nanoribbons, and carbon nanotubes with other common channel materials for FET channel. From Ref. 10.

Figure 1-3: Schematic of quantum Hall (QH) and quantum spin Hall (QSH) effect. In QSH state, the spin and momentum of electrons are locked in the edge state, i.e. two opposite spin current transport in opposite directions in one edge. From Ref. [15].

spin propagate in opposite directions (Figure 1-3), so that graphene is predicted to exhibit the quantum spin Hall (QSH) effect at low temperature.[12] Details of topological insulators will be introduced in Section 1.1.4. These fascinating characteristics of graphene, including the massless Dirac fermions and QSH effect, have stimulated numerous scientific breakthroughs.[5,12]

However, the drawbacks of graphene, especially its inability to act as a semiconductor, stimulate chemists and materials scientists to investigate novel 2D materials beyond graphene. [16] There is a very wide spectrum of 2D materials, from insulators to metals, with chromatic properties: ultra-clean surface, flatness, flexibility, transparency, superconducting phenomenon, topological electronic structure. [9,16] In recent years, the family of 2D materials has been rapidly expanded to monoelemental layers (silicene, phosphorene, etc.), transition metal dichalcogenides (TMD) and MXenes. [9,16] (Figure 1-2a) The number of publications related to them starts to increase rapidly in recent years (Figure 1-2b), and their future applications have also gone beyond the continuing of Moore's law in microelectronics, extending to novel devices in light emission, energy storage, and so on. [9,16] As promising members of the novel layered materials, germanene, stanine and tungsten ditelluride are chosen to be my targets in this research.

1.1.2. Germanene and stanene

Germanene and stanene are monoelemental 2D materials with buckled structure (Figure 1-5a). [17] As the analogues of graphene and silicene, they also have the Dirac-cone in their band structures (Figure 1-5b&c), bringing them ultrahigh carrier mobility and non-trivial topological state with QSH effect. [17,18] Beyond the similarity, germanene and stanene have stronger spin-orbit coupling (SOC) and larger SOC gaps of over 23 meV and 73 meV,[18–21] respectively, compared to 1.55 meV in silicene and 8 μeV in graphene,[19,22] leading to the possibility of room-temperature 2D topological insulators.[14,23] Recently, they have been successfully synthesized on several metallic substrates, for example Pt(111), Au(111), and Al(111) surfaces for germanene [24–26] and Bi_2Te_3(111) surface for stanene (Figure 1-5d-f). [27] Their buckled structures make their band structures even more tunable than monolayer graphene by external electric field or surface atom adsorption.[28–32] In addition, germanene is predicted to have doubled intrinsic carrier mobility, one order of magnitude smaller electron-phonon coupling and three times longer spin dephasing length compared to graphene.[33–35] Very recently, germanene is synthesized on MoS_2, [36] which is the first time that a semiconducting substrate can be used for germanene in experiment. Although germanene becomes semi-metallic in experiment due to strain,[36] theoretical research predicts that

Figure 1-5: (a) Structure of germanene and stanene; (b, c) Band structure of (b) germanene and (c) stanene; [17,21] (d, e) Synthesis of germanene on (d) Au [25] and (e) Al [26]; (f) Synthesis of stanene on Bi_2Te_3. [27] (g) DFT band structure prediction of stanene on Bi_2Te_3. [27] The red dots are projection of stanene. Note that stanene becomes semimetallic on Bi_2Te_3. Figures (b-g) are from corresponding references.

germanene can keep its non-trivial topological state on MoS_2.[37] In theory, not only the band gap but also topological phase of germanene and stanene are tunable by a vertical electric field.[32] Intrinsically silicene, germanene and stanene are topological insulators with a band gap opened by SOC and $Z_2 = 1$. If a vertical electric field is applied to them, their band gap will first reduce to zero and then open again (Figure 1-6a). The critical point happens when the electric field $E = E_c = \Delta\lambda_{SO}$, where Δ is the buckling and λ_{SO} indicates the SOC strength. Beyond the critical point, germanene and stanene will become trivial band insulator with $Z_2 = 0$ due to the band closure. (Figure 1-6b)

However, two problems remain to be solved: (1) Germanene and stanene still lack suitable semiconducting substrates. In experiment, most of the reported substrates are metallic, except for MoS_2. On those metallic substrates, researchers fail to observe solid evidence of Dirac cone in germanene and stanene (Figure 1-5g for stanene on Bi_2Te_3). Even for germanene on MoS_2, the

existence of the hole-pocket at the Γ point induced by the ~5% strain renders the utilization of the Dirac cone properties at the K point difficult.[36] Unfortunately, traditional insulating or semiconducting substrates like SiO_2 and GaAs strongly interact with germanene and ruin the Dirac cone.[28,38] (2) Germanene and stanene should be supported or protected by solid substrates in practice, but the effect of substrate on the electronic state and Z_2 topological indexes of supported germanene and stanene remain to be investigated systematically. Currently, only the Z_2 invariant of germanene on MoS_2, h-BN and Al_2O_3 have been studied.[20,37,39] Whether germanene and stanene have different topological phases on other substrates and how to explain the interaction between germanene/stanene and 2D substrates in general are still open questions.

Table 1-1: Comparison of carrier mobility μ, spin-orbit-coupling coefficient λ_{SOC}, average electron-phonon coupling matrix element square at Fermi level $<g_\Gamma^2>_F$, spin dephasing length L_{sd} of graphene, silicene, and germanene. [18–22,33–35]

Name	μ (cm^2/Vs)	λ_{SOC} (meV)	$<g_G^2>_F$	L_{sd} (μm)
Graphene	3×10^5	0.008	0.04	0.5
Silicene	2×10^5	1.6	0.02	0.5
Germanene	6×10^5	23	0.002	1.5

Figure 1-6: (a) Band gap size of silicene, germanene and stanene under external electric field considering SOC. The critical point E_c where the gap drops to zero varies with the SOC strength and buckling of each material. From Ref. 32. (b) Topological phase transition of silicene, germanene and stanene under external electric field. Intrinsically they are topological insulators with $Z_2 = 1$. As the band gap close and re-open under a vertical electric field, a topological phase transition happens in them, turning them into trivial band insulators with $Z_2 = 0$. From Ref. 161.

1.1.3. Tungsten ditelluride WTe$_2$

Transition metal dichalcogenides (TMD) is an emerging family of two-dimensional (2D) layered semiconductors and semimetals, whose chemical compositions are denoted by MX$_2$ with M representing a transition metal element like Mo, W, and Nb, and X representing a chalcogen element like S, Se, and Te. There are several types of polymorphs for TMD: 2H, 1T, 1T' and Td (Figure 1-7a), and the most preferable phase at room temperature varies with the MX$_2$ type. Metallicity and other properties change with different phases, e.g. the semiconducting 2H-MoS$_2$ and metallic 1T-MoS$_2$.[40] In general, TMD are attracting the eyes of global researchers by their exotic properties like layer-dependent band gap[41], valley[42] and layer[43] pseudospin arising from inversion symmetry breaking and strong spin-orbit coupling (Figure 1-7b). The valley pseudospin of $\pm\frac{1}{2}$ is the additional degree of freedom indicating the inequivalent but energetically degenerated states at K and -K valleys at the corners of the hexagonal Brillouin zone.[44] The layer pseudospin, appears only in bilayer and multilayer TMD, is similar to valley pseudospin by replacing valleys with the odd and even layers of TMD with a spin-layer locking effect.[45] While semiconducting TMD gained a large part of the attention, semimetallic TMDs like WTe$_2$ was overlooked until recent years.

Figure 1-7: (a) Structures of TMD. 2H is the common structure for MoS$_2$ and WS$_2$, 1T' for MoTe$_2$, and Td for WTe$_2$. From Ref. 46. (b) Typical band structure near K and -K for semiconducting TMD like MoS$_2$. From Ref. 44.

Semimetallic WTe$_2$ is quite unique and has many interesting properties, even compared with other novel TMD family members. Unlike its cousins, which are usually centrosymmetric at room temperature, WTe$_2$ is non-centrosymmetric and semi-metallic in its most stable Td phase (space

group: *Pmn*2_1) under ambient conditions (Figure 1-7a, leftmost). [47,48] The W atoms undergo a Peierls's-like transition, which refers to the spontaneous dimerize of a chain of equally spaced atoms, to form a quasi-1D chain. [47,48] As a layered material, the interlayer interaction in WTe$_2$ is non-negligible in determining its electronic structure, rendering it "more than 2D". [49] Various kinds of exotic properties have been found in WTe$_2$. In experiment, an extremely large magnetoresistance (XMR) that does not saturate at strong magnetic fields of tens of tesla and reaches 10^5% at cryogenic temperature is observed in WTe$_2$, which is attributed to the balance of the electron and hole due to its semi-metallic nature (Figure 1-8a-b). [50] Such MR can be suppressed by the application of hydrostatic pressure.[51] As the temperature goes down, WTe$_2$ undergoes a Lifshitz transition, the change of Fermi surface topology, around 160K [52] and a semiconductor-superconductor phase transition at 6.5K. [51] In theory, the absence of parity makes

Figure 1-8: (a) XMR measured in WTe$_2$ at 0.53 K. Note that the XMR is not saturated even at ~50 T. From Ref. 50. (b) XMR measured in WTe$_2$ at 0.25K, and the fitting of two-band model. The experimental data of MR and the transverse resistance ρ_{xy} (blue solid lines) can be well reproduced by this model (red dashed lines). From Ref. 160. (c) Schematic of type-II (tilted) Weyl-cone. From Ref. 53. (d-e) DFT band structure of WTe$_2$ (d) without SOC and (e) with SOC. Electron and hole pockets are apparent. (f) Zoomed band structure around the two Weyl-points in WTe$_2$. From Ref. 53.

WTe$_2$ a possible candidate of the type-II Weyl-semimetal with tilted Weyl-cones in its band structure (Figure 1-8c-f). [53] Nevertheless, the properties of WTe$_2$, especially the exact surface structure with possible surface relaxation, remain to be confirmed or revealed.

1.1.4. Topological insulator

Traditional band theory exploits the translation symmetry of the crystal and classify electronic states, or Bloch states, by their reciprocal momentum k in a periodic Brillouin zone.[54,55] An insulator is defined in the band theory by the presence of an energy gap, called band gap, between the highest occupied state and lowest unoccupied state. Although traditional band insulators has various kinds of band gap with large or small gap size, they are actually transferable to each other and all to vacuum by tuning the Hamiltonian continually without closure of the band gap.[55] In contrast, some special matters cannot be adiabatically connected to conventional insulators and vacuum, like the quantum Hall (QH) state and QSH state.[13,55] Integer QH state can be realized in 2D electron gas under an external magnetic field. [56,57] The quantized Landau levels of electrons can be viewed as the "band structure" of the 2D electron gas.

One may ask that what is the difference between a QH state with the traditional band insulator. The answer is given by Thouless, Kohmoto, Nightingale, and den Nijs in 1982 (Thouless obtained the Nobel-prize in 2016 with this work): topology,[58] or more specifically speaking, topology of the phase of Bloch states in the reciprocal space. The electronic states of a 2D gapped system, defined on a torus k-surface due to the periodicity in both k_x and k_y, can be classified topologically in to two sub groups which are distinguished by a topological invariant $n \in \mathbb{Z}$ (set of integers) called Chern number.[55] Mathematically, Chern number categorize the topology of the 'fiber bundles', functions defined on a manifold.[59] In the language of physics, the manifold is the torus-like k-surface (2D 1st Brillouin zone itself, not a surface in the reciprocal space) and the fiber bundles consist of the (Bloch) wave functions at each k-point $|u_m(\vec{k})\rangle$, where m indicates the band number. Following the notation and arguments from Ref. 55,60, Chern number can also be physically associated to the Berry phase r_m, defined as the integral on a closed curve C on the torus $r_m = \oint_C d\vec{k} \, \mathcal{A}_m(\vec{k})$ without degenerate states, where the Berry connection $\mathcal{A}_m = i\langle u_m|\nabla_k|u_m\rangle$.[55,60] For easier description, Berry curvature is defined as $\vec{\Omega}_m(\vec{k}) = \nabla \times \mathcal{A}_m$, which can be viewed as the flux of the Berry connection. Then Berry phase can be rewritten as $r_m =$

$\int_S d\vec{S}\vec{\Omega}_m(\vec{k})$ by the Stokes theorem, where S is the area enwrapped by curve C. The Berry phase is always associated with a closed path and gauge dependent, while the Berry curvature is a local quantity, gauge-invariant and intrinsic property of the band structure defined at a point on the torus.[60] The Chern number of a single band m is defined as the total Berry curvature on the torus divided by 2π: $n_m = \frac{1}{2\pi}\int_{BZ} d\vec{S}\vec{\Omega}_m(\vec{k})$, and the total Chern number n of the system is the sum of n_m over all occupied bands. [55,60] Besides gauge-invariance, n is topologically invariant and also called TKNN invariant, because it does not change when the Hamiltonian of system changes smoothly.[55,60] States with non-zero n has non-zero QH conductance and thus are classified as topologically non-trivial QH states.

However, there are another type of topologically non-trivial state. The QH state require the break of time-reversal symmetry $\mathcal{T}$, but even if $\mathcal{T}$ is preserved in a system (thus $n = 0$ and trivial in the sense of QH), a second type of topologically non-trivial state is possible under the presence of the spin-orbit coupling (SOC). The explanation is given below following the arguments and notations from Ref [55]. For 1/2 spin systems, $\mathcal{T}$ symmetry's operator Θ has an important property $\Theta^2 = -1$, leading to the constraint known as Kramers' theorem that all eigenstates of the system are at least twofold degenerate.[55] This is because if a nondegenerate state $|\chi\rangle$ exist, then $\Theta|\chi\rangle = c|\chi\rangle$, but $\Theta^2|\chi\rangle = |c|^2|\chi\rangle = -|\chi\rangle$, which is impossible since $|c|^2 \neq -1$.[55] Without SOC, the degeneracy is just between up and down spins; with SOC, such degeneracy will lead to nontrivial consequences. Thus if there are edge states inside the band gap, at $\mathcal{T}$ invariant k points they are degenerate and called Kramers' pairs. On a path that connects the $\mathcal{T}$ invariant k points, they are no longer degenerate due to the SOC and form split edge bands. The number of Kramers pairs of edge modes that cross the fermi level defines the Z_2 topological invariant: even means $Z_2 = 0$ (trivial) and odd means $Z_2 = 1$ (non-trivial). One of the approach to calculate the Z_2 invariant, proposed by Fu and Kane,[61] is to use the overlap matrix of Θ from the occupied Bloch wave functions: $w_{mn}(\vec{k}) = \langle u_m(\vec{k})|\Theta|u_n(\vec{k})\rangle$. From $\Theta^2 = -1$ we know that $w^T(\vec{k}) = -w(-\vec{k})$. At the k-points where $\vec{k} = -\vec{k}$ (e.g. Γ and M points in graphene), w is antisymmetric. There are four such points for the 2D Brillouin zone and 8 for the 3D Brillouin zone, labeled by Λ_a ($a = 1\sim4$ (2D) or $1\sim8$ (3D)). Z_2 invariant ν for a 2D system is then calculated by $(-1)^\nu = \prod_{a=1}^4 \text{Pf}[w(\Lambda_a)]/\sqrt{\det[w(\Lambda_a)]}$ and can be generalized to 3D similarly. Here $\text{Pf}[w(\Lambda_a)]$ means the Pafaffian of $w(\Lambda_a)$ which has the property of $(\text{Pf}[w(\Lambda_a)])^2 =$

$\det[w(\Lambda_a)]$.

Materials with non-trivial Z_2 invariant are called topological insulators (TI). Characterized by the contrast of an insulating gap inside the bulk and a gapless helical edge or surface states protected by the time-reversal symmetry, they have simulated global research interest in theoretical and experiment investigation. Two-dimensional TI, or QSH state, was first predicted in graphene[12] but discovered in HgTe/CdTe quantum wells.[62] At the edge of the 2D TI with a band gap in the bulk part, there are topologically protected 1D gapless edge states within the bulk band gap. In the 2D case, two edge states with opposite spin at a given edge propagate in the opposite direction. Since the spin is "locked" to the moving direction, the edge states in QSH insulators are also called helical edge states (Figure 1-9). As introduced above, free-standing germanene and
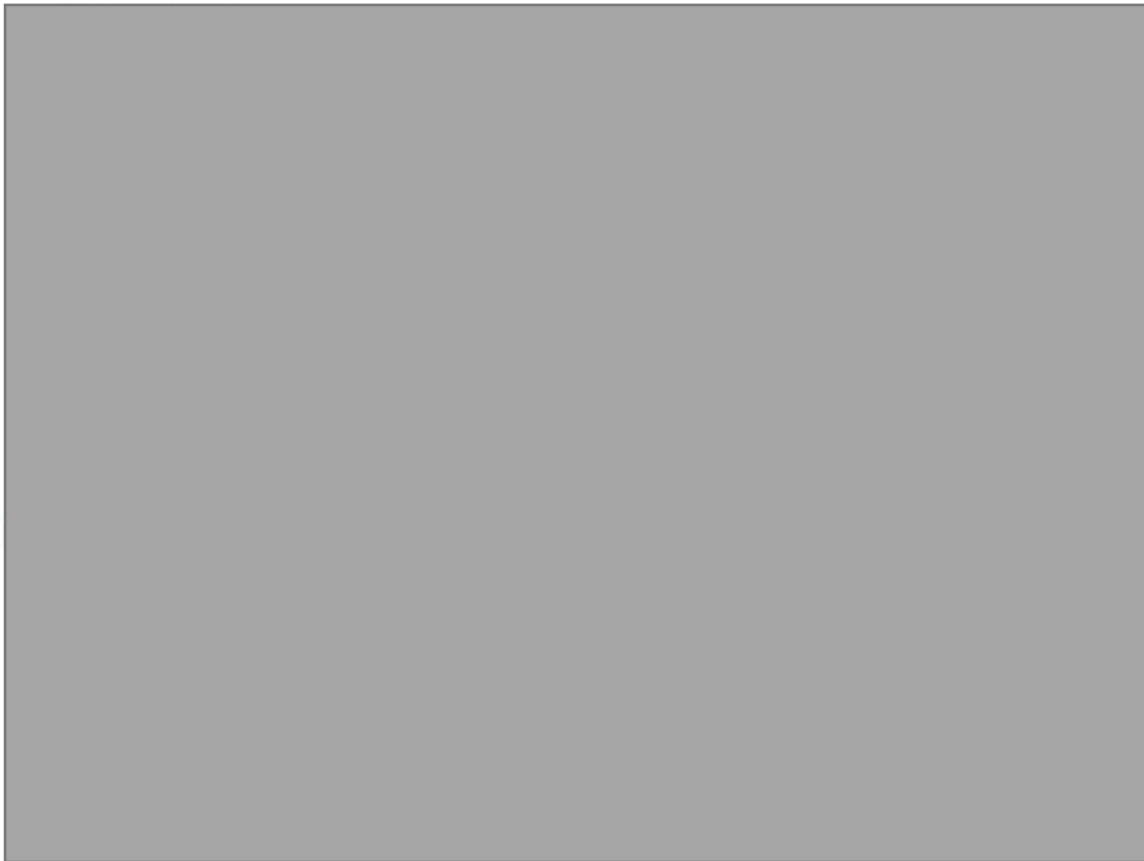
Figure 1-9: Schematic of the spin-polarized edge channels in a topological insulator. The carriers travel at the edge of topological insulator will have their momentum and spin locked: the carriers with the opposite spin will propagate in the opposite direction, forming the chiral spin current at the edge.   (http://science.sciencemag.org/content/suppl/2007/11/01/318.5851.766.DC1)

stanene are 2D QSH insulators in their intrinsic form, making them promising in the application of spintronic devices.

1.1.5. Purpose and organization of this dissertation

As mentioned above, there are still several problems left to be investigated for germanene, stanene and WTe_2. For germanene and stanene, two problems remain to be solved: (1) Germanene and stanene still lack suitable semiconducting substrates. (2) Germanene and stanene should be supported or protected by solid substrates in practice, but the effect of substrate on the electronic state and Z_2 topological indexes of supported germanene and stanene remain to be investigated systematically. For WTe_2, its the exact surface structure with possible surface relaxation remain to be confirmed or revealed.

The purpose of this dissertation is to investigate these problems, which can be divided into two parts:

- Look for semiconducting substrates for germanene and stanene, which is crucial for practical application in electronic devices
  - ◇ Search for suitable semiconducting layered substrates for germanene and stanene by experience and data mining
  - ◇ Understand the physics in the substrate interaction of germanene and stanene
- Explore novel surface properties in WTe_2
  - ◇ Examine the presence and impact of surface relaxation in WTe_2

The organization of this dissertation is as follows: Chapter 2 introduces the methods used in this work, including density function theory (DFT), Z_2 invariant calculation and materials informatics. In Chapter 3, the substrates for germanene found by intuitive guess, group-III monochalcogenides, are presented. The DFT calculation procedure to examine the behavior of germanene on a certain substrate is established in this part. In Chapter 4, the systematic materials search for the layered substrates for germanene and stanene is presented. Potentially suitable candidates are filtered out from the ICSD database by data mining. By using DFT and Z_2 invariant calculations, the electronic structure and topological phase of germanene and stanene on the candidate substrates are investigated. Furthermore, the low-energy tight-binding Hamiltonian of germanene is used to explain the band gap variance and topological phase transition on substrates. In Chapter 5, the surface relaxation of WTe_2 is investigated in cooperation with experimental measurements. The relaxation configuration measured by low-energy electron diffraction (LEED)

is cross-validated with the DFT optimized surface structure, and the surface Fermi surface given by DFT is apparently affected by the relaxation. Finally, Chapter 6 summarizes the dissertation and provides future research prospects.

2. Methodology

2.1. Density functional theory

The density functional theory (DFT) is currently one of the most omnipresent *ab initio* computational approaches to obtain the ground-state electronic structure of atoms, molecules and condensed matters. The word *ab initio* means "from the beginning", indicating that the method is independent of empirical parameters and only relies on the law of physics in the context of condensed matter physics. DFT can provide efficient yet relatively accurate computational predictions on various properties of materials, such as band structure, magnetism, and vibrational behaviors, for systems with 10~1000 atoms (the number varies with the evolution of computing technology and algorithm, though). The good balance between efficiency and accuracy along with the independency from experimental parameters makes DFT a suitable and powerful method for the theoretical investigation of low-dimensional materials in present work. In this section, the basic knowledge of DFT will be introduced.

2.1.1. Schrödinger equation of crystals

In the equilibrium state without external field, crystals and any other atomic systems with N electrons, whose positions are denoted as $\{\vec{r_1}, \vec{r_2}, .., \vec{r_i}, .. \vec{r_j}, .. \vec{r_N}\}$, and M nuclei, whose positions are denoted as $\{\vec{R_1}, \vec{R_2}, .., \vec{R_A}, .., \vec{R_B}, .. \vec{R_M}\}$, can be described by the time-independent many-body Schrödinger equation:

$$H\Psi = E\Psi, \qquad\qquad 2\text{-}1$$

where H is the Hamiltonian, and Ψ is the many-body wave function. The many-body Hamiltonian H is given as

$$H = H_{elect} + H_{ion} + H_{i-e} + H_{i-i} + H_{e-e}, \qquad\qquad 2\text{-}2$$

where the kinetic term of electron $H_{elect} = -\sum_{i=1}^{N} \frac{\hbar^2}{2m_e} \nabla_i^2$, kinetic term of atomic nuclei $H_{ion} = -\sum_{A=1}^{M} \frac{\hbar^2}{2M_A} \nabla_A^2$, electron-nuclei coulomb interaction $H_{i-e} = -\frac{e^2}{4\pi\varepsilon_0} \sum_{i=1}^{N} \sum_{A=1}^{M} \frac{Z_A}{|\vec{r_i} - \vec{R_A}|}$, nuclei-nuclei coulomb interaction $H_{i-i} = \frac{e^2}{4\pi\varepsilon_0} \sum_{i=1}^{N} \sum_{j>i}^{N} \frac{i}{|\vec{r_i} - \vec{r_j}|}$, and electron-electron coulomb interaction $H_{e-e} = \frac{e^2}{4\pi\varepsilon_0} \sum_{A=1}^{M} \sum_{B>A}^{M} \frac{Z_A Z_B}{|\vec{R_A} - \vec{R_B}|}$. Here, m_e is the mass of free electron, M_A is the mass of the Ath

nucleus, Z_A is the number of electrons of the Ath nucleus, and ε_0 is the vacuum permittivity.

The exact solution of equation 2-1 is very hard to obtain, even with the help of the most powerful ever modern supercomputers. Thus, several approximations are made to reduce the complexity. The Born-Oppenheimer (BO) approximation is one of the most commonly used approximations, which is not limited to the most commonly used DFT scheme, but also applied in many other methods. The core of BO approximation is the adiabatic separation of the nuclei's and electrons' motions.[63,64] The nuclei has a much larger mass compared to electrons, i.e. $M_A \gg m_e$, so the momentum of nuclei can be ignored in dealing with electrons, which means electrons feel a fixed crystal potential in BO approximation. Thus far, the ionic kinetic term $H_{ion} = 0$ is separated to the ionic Hamiltonian and is ignored in the electronic Hamiltonian, and the ionic-electron coulomb interaction H_{i-e} can be viewed as a part of the (static) external potentials V_{ext} exerted on the electrons, denoted as $H_{ext} = \sum_{i=1}^{N} eV_{ext}(\vec{r_i})$ under BO approximation. Besides the BO approximation, the ionic coulomb interaction H_{i-i} is a constant $H_{i-i} = C(\vec{R})$ irrelevant to the electronic state. As a result, the new Hamiltonian H_{BO} for the electron system can be rewritten as:

$$H_{BO} = H_{elect} + H_{e-e} + H_{ext}, \qquad\qquad \text{2-3}$$

Equation 2-3 is still hard to solve due to the existence of many-body term H_{e-e}. DFT, based on Hohenberg–Kohn theorem and Kohn-Sham equation, turns this many-body problem into a single-particle problem consisting of non-interacting Kohn-Sham quasiparticles to achieve its high efficiency, which is introduced below.

2.1.2. Hohenberg–Kohn theorem and Kohn-Sham equation

The Hohenberg-Kohn (HK) theorems established in 1964 are the heart of the most commonly used DFT scheme. [65] The theorems are presented as follows:

(1) The external potential V_{ext} and total energy E of any electron system is a unique functional of the electron density $\rho(\vec{r})$. It immediately leads to a corollary: the external potential and other properties of the electron system is exclusively determined by the ground state electron density ρ_0.

(2) The total energy E, if defined as a functional of the electron density $E = E(\rho(\vec{r}))$, reaches minimum E_0 (i.e. ground state energy) if and only if $\rho(\vec{r}) = \rho_0$. This theorem is origin of the name DFT in the meaning of determining energy by the functional of electron density.

The theorems were initially established at zero temperature and later extended to finite temperature.[66] It is straightforward that the combination of the two theorems can make up the

scheme for investigating the properties of materials by using DFT: first find ρ_0 that minimizes $E(\rho) = T(\rho) + V_{ext}(\rho) + V_{xc}(\rho)$ and then calculate other properties from ρ_0. Nevertheless, the exact form of $E(\rho)$ remains unknown even now. Although HK theorems are exact, in practice one has to rely on approximated energy functionals, especially in the kinetic term $T(\rho)$ and exchange-correlation term $V_{xc}(\rho)$. In the history, Thomas-Fermi approximation was used to calculate the kinetic term but has many deficiencies such as the absence of chemical bonding in molecules and crystals or the lack of a shell structure of atoms.[67]

Figure 2-1: Flow chart of the KS-DFT formalism.
(http://www.iue.tuwien.ac.at/phd/goes/dissse14.html)

The Khon-Sham (KS) approach provides a reasonable approximation to the kinetic term and thus become the core of modern DFT scheme.[67,68] The key point in the KS approach is to use a

non-interacting electron systems with the same number of electron instead of the real interacting system. Particularly, the ground state wavefunction of the N electron KS system can be explicitly written as a single slater determinant:[64]

$$\Psi_{KS} = \frac{1}{N!}\det[\phi_1\phi_2\ldots\phi_N],\qquad\qquad 2\text{-}4$$

The charge density is then:

$$\rho_{KS}(\vec{r}) = \sum_{i=1}^{N}|\phi_1(\vec{r})|^2,\qquad\qquad 2\text{-}5$$

The kinetic term $T_{KS}(\rho_{KS})$ is then naturally come back from density functional to the form of momentum operator H_{elect}, but act on the KS wavefunction. The complete KS energy functional is like:[64]

$$E(\rho_{KS}) = T_{KS}(\rho_{KS}) + \int d\vec{r}\,\rho_{KS}(\vec{r})V_{ext}(\vec{r}) + \frac{1}{8\pi\varepsilon_0}\int\int d\vec{r}d\vec{r}'\frac{\rho_{KS}(\vec{r})\rho_{KS}(\vec{r}')}{|\vec{r}-\vec{r}'|} + E_{xc}(\rho_{KS}),\quad 2\text{-}6$$

Where the third term is the Hartree term. $E_{xc}(\rho_{KS})$ is the exchange-correlation energy, defined as the difference between the non-interacting KS system and real BO system. Both the error in kinetic term and electron-electron interaction potential term contributes to $E_{xc}(\rho_{KS})$, with the latter one being the major part. With the above formalism, the ground-state charge density can be solved by the self-consistent iteration of Ψ_{KS} and ρ_{KS}, as shown in Figure 2-1.

2.1.3. Exchange-correlation functional

In KS scheme, the only unknown term is $E_{xc}(\rho_{KS})$. The exact form is unknown, but approximations are much easier to be found compared to the HK energy functional $E(\rho)$. Several typical approximations are commonly used in practice, such as local density approximation (LDA) , generalized gradient approximations (GGA), and hybrid functionals.

LDA is the simplest, yet still effective, functional with the form of $E_{xc}^{LDA} = \int d\vec{r}\epsilon_{xc}(\rho_{KS}(\vec{r}))\,\rho_{KS}(\vec{r})$, where $\epsilon_{xc}(\rho_{KS}(\vec{r}))$ is the exchange-correlation energy of a uniform electron gas with charge density $\rho_{KS}(\vec{r})$ numerically computed by quantum Monte-Carlo. One can deduce that E_{xc}^{LDA} of a certain point $\vec{r}_i$ is only related to its local density $\rho_{KS}(\vec{r}_i)$, hence the functional is named after "local density approximation". It is easy to know that LDA can provide a good approximation in the physical limit of "flat" charge density with slow change of value with regard to coordinate. The rank of the accuracy of functionals are often called the 'Jacob's ladder' of density functional theory (Figure 2-2). As the simplest exchange-correlation functional, LDA is on the first Jacob's ladder (Figure 2-2). The over-approximated LDA may introduce errors like over-binding, underestimation of lattice constants and wrong magnetism.

GGA is an extension and amelioration of LDA to non-uniform systems by taking the gradient of charge density into account, hence it is on the second Jacob's ladder (Figure 2-2). There are various forms of GGA functional, among them the PBE[69] form is used in this dissertation. The form of GGA functional can be written as $E_{xc}^{GGA} = E_x^{GGA} + E_c^{GGA}$, where $E_c^{GGA} = E_c^{LDA} + G_c^{GGA}$ is the sum of LDA correlation part and GGA gradient correction term, and $E_x^{GGA} = \int d\vec{r}\epsilon_{xc}(\rho)F_x^{PBE}(s)\rho$ is E_x^{LDA} modulated by the gradient enhancement factor $F_x^{PBE}(s) = 1 + \kappa - \kappa/(1 + \mu s^2/\kappa)$. Here, $s \sim |\nabla\rho|/\rho$, and the parameters for $F_x^{PBE}(s)$ are $\mu = 0.2195$ and $\kappa = 0.804$, obtained by fitting the behavior of E_x^{GGA} to several physical constrains.[69] The PBE functional is widely used due to its good balance in accuracy and speed in studying 2D materials like silicene and germanene.[17,28]
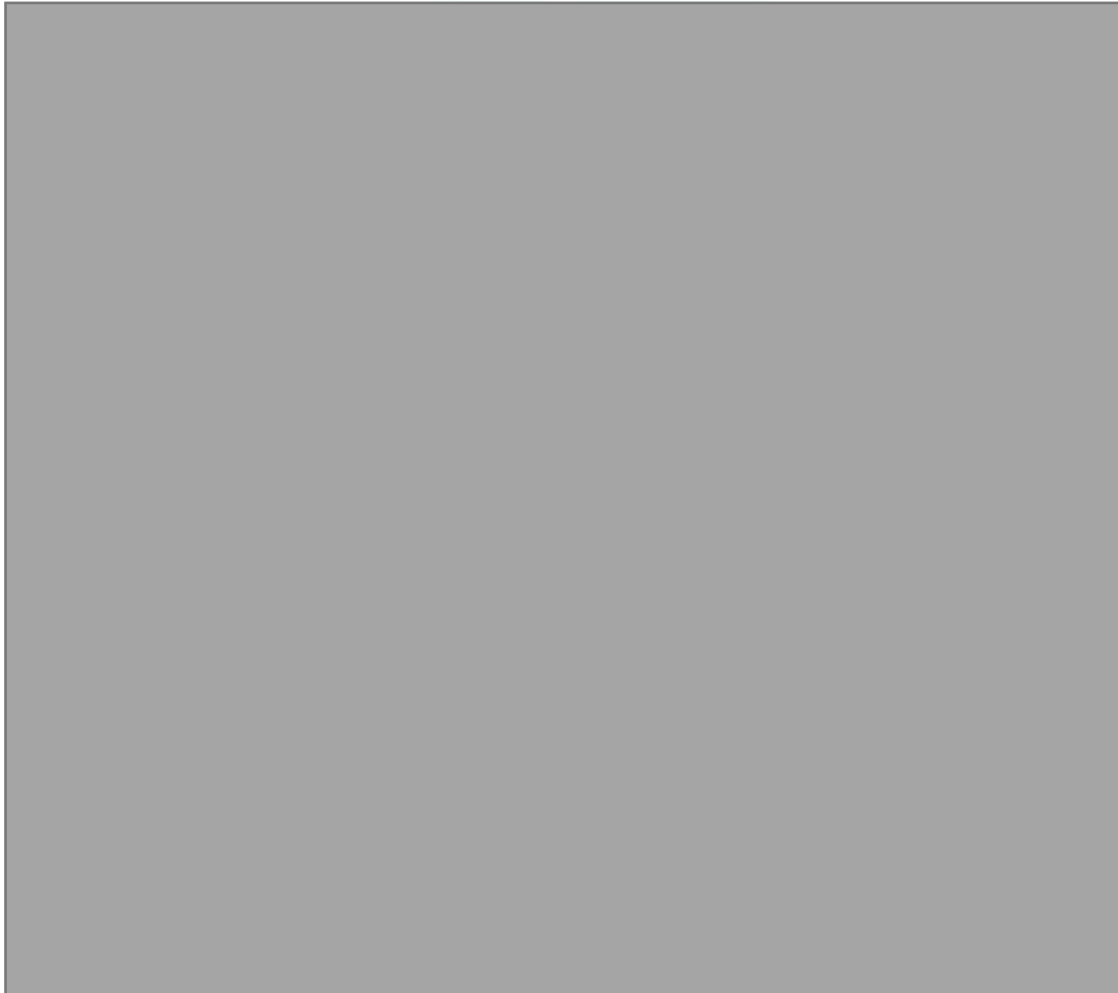
Figure 2-2: The Jacob's Ladder of DFT exchange-correlation approximation. The higher the position, the more factors are taken into account and the more accurate, as well as more time consuming, the functional is. (http://www.sas.upenn.edu/~jianmint/Research/)

Hybrid functionals includes a portion of exact Hartree-Fock exchange and thus ameliorate the underestimation of band gap by using GGA, taking the 4th order of the Jacob's ladder (Figure 2-2). There are also various kinds of hybrid functionals, and the one used in this dissertation is called HSE06. [70–72] The form of HSE06 is $E_{xc}^{HSE06} = \alpha E_x^{HF,SR} + (1-\alpha)E_x^{PBE,SR} + E_x^{PBE,LR} + E_c^{PBE}$, where $\alpha = 1/4$ is the portion of HF exchange introduced into the short-range (SR) part. In the long-range (LR) part, it is the same as PBE. The separation of SR and LR is determined by using the complementary error function $\mathrm{erfc}(x) = 1 - \mathrm{erf}(x) = \frac{2}{\sqrt{\pi}}\int_x^{\infty} e^{-t^2} dt$. The character of $\mathrm{erfc}(x)$ is that it drastically drops to nearly 0 when x is larger than a typical positive radius ω. Specifically, the gradient enhancement factor of the SR part of PBE exchange energy is the original PBE enhancement factor modulated by $\mathrm{erfc}(\omega)$, written as $F_x^{PBE,SR}(\rho, s, \omega) = -\frac{8}{9}\int_0^{\infty} yJ^{PBE}(\rho, s, y) \times \mathrm{erfc}(\frac{\omega y}{\sqrt[3]{3\pi^2\rho}}) dy$, where $J^{PBE}(\rho, s, y)$ is the original PBE exchange hole. The integration without complementary function gives the original form of the PBE gradient enhancement factor. The LR part is then the rest part of original PBE exchange energy $E_x^{PBE,LR} = E_x^{PBE} - E_x^{PBE,SR}$. A radius $\omega = 0.15$ bohr^{-1} is chosen for HSE06 so as to balance the accuracy and speed in molecules and solids. [73]

2.1.4. Van-der Waals correction for DFT

In low-dimension materials, especially layered materials, the long-range nonlocal van der Waals (vdW) interactions, including Keesom, Debye and London dispersion interaction, is crucial in stabilizing the system. [74] Unfortunately, it is very challenging to describe the vdW interaction accurately, especially in DFT: the commonly used exchange-correlation functionals based on local or semilocal electron density have insufficient ingredients to describe the nonlocal electron-electron interactions. For example, GGA overestimates the interlayer distance in graphite, while LDA tends to underestimate it. [75] The error of LDA is sometimes small and gives nearly correct vdW interaction distance in layered materials like graphene, but such cancellation is not widely applicable on other materials with many counterexamples reported. [76,77] Actually, inclusion of vdW interaction into DFT, even approximately, has been one of the most important research direction in this field recent years.

Figure 2-4: Comparison of the relative errors in the lattice constants calculated with different vdW-DF functionals. From Ref. 78.
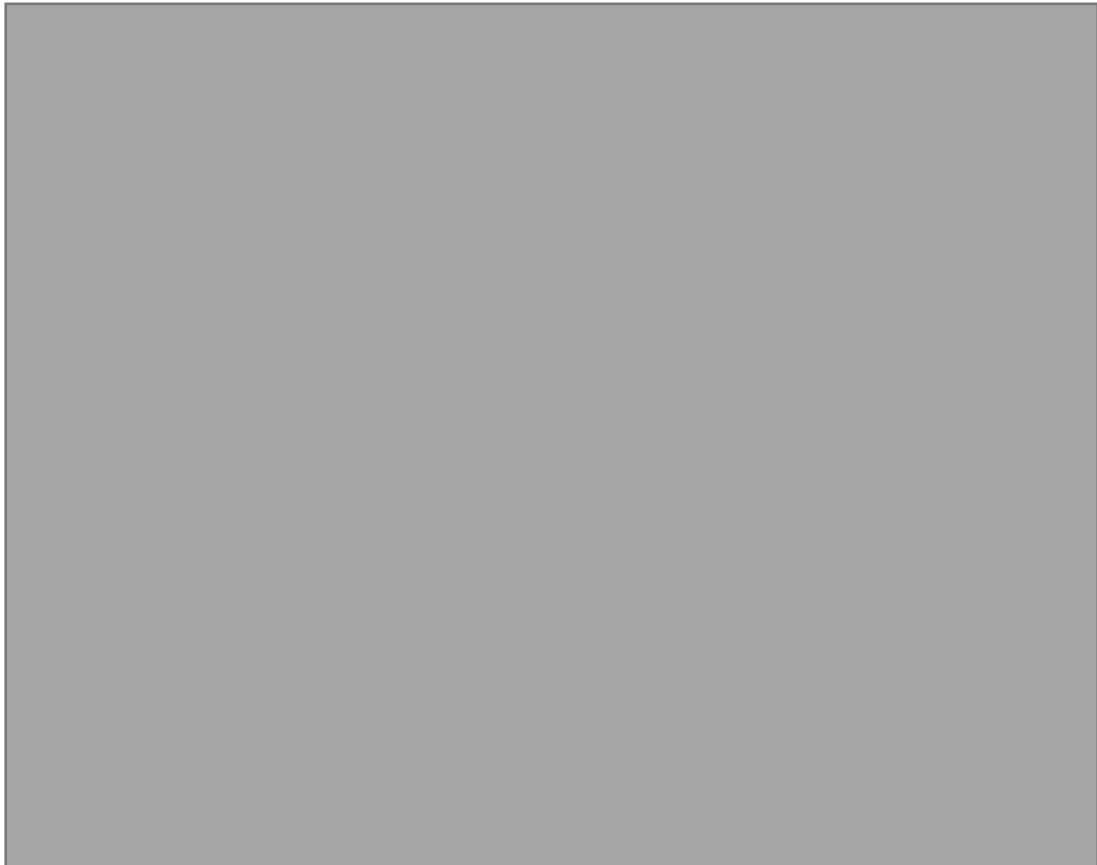
Figure 2-3: Interlayer binding energy of graphite as a function of interlayer separation d calculated by different functionals. Although the energy per atom given by vdW-optB86b seems to be a bit lower than the experimental value region, the interlayer distance given by it is very close to the experimental one. From Ref. 87.

As a correlation effect, vdW interaction is included in $E_{xc}(\rho)$.[79] There are several methods for the inclusion of vdW interaction, including (1) explicit density functionals, like vdW-DF; (2) DFT extended with atom-pair potentials, like DFT-D and TS-vdW; (3) perturbation theory in the random-phase approximation.[74] Among them, the vdW-DF method series, including vdW-DF, optB86b-vdW/optB88-vdW, vdW-DF2 and rev-vdW-DF2 functional,[80–85] is widely used and benchmarked on different kinds of materials. The optB86b-vdW functional is chosen to be used in this work, since it generally behaves better than vdW-DF and optB88-vdW in the lattice constant for common materials (Figure 2-4) and interlayer distance in graphite (Figure 2-3). [78] In optB86b-vdW, exchange-correlation functional takes the form of $E_{xc} = E_x^{GGA} + E_c^{LDA} + E_c^{nl}$, where E_x^{GGA} uses the revised exchange part of the B86b functional to fit the exchange enhancement factor to the 2/5 order behavior in the upper limit of density gradient, E_c^{LDA} is the LDA correlation energy, and E_c^{nl} is the nonlocal energy approximated by using a double space integration.[86] The revision of exchange part in GGA functional, as well as the inclusion of the non-local part E_c^{nl}, makes optB86b-vdW more accurate on the vdW interaction.

2.2. Z_2 topological invariant

The Z_2 topological classification is the key to distinguish TI from traditional insulators.[12] As described above, it divides time-reversal invariant insulators into two classes: ordinary (with even Z_2) insulators that can be adiabatically converted to the vacuum, and "topological" (with odd Z_2) ones that cannot be so connected.[88] The adiabatic conversion is applicable to all members within in one Z_2 class, but not possible for insulators from the two different Z_2 classes. There are several ways to calculate the Z_2 invariant of a system, but most of them are limited to centrosymmetric systems or have to introduce artificial changing procedures of spin-orbit coupling.[89,90] In this work, since the sytem of germanene/stanene with substrates usually does not have inversion symmetry, the algorithm developed by Alexey A. Soluyanov and David Vanderbilt implemented in Z2pack is utilized,[88] which does not have the limitations mentioned above. Below the algorithm is briefly introduced.

The method is based on the concept of time-reversal polarization (TRP) but in the form of movement of Wannier charge centers (WCC). It is explained below following the argument and notations of Ref. [88]. TRP was proposed by Fu and Kane.[61] They considered a family of 1D bulk-gapped Hamiltonian $H(x,t)$ that is periodic in both position x and cyclic parameter t, whose periodicity is $H(x,t) = H(x + 1, t)$ and $H(x,t) = H(x, t + T)$, respectively, with the

constraint $H(x, -t) = \theta H(x, t)\theta^{-1}$, where θ is the time reversal operator. It can be considered as an adiabatic pumping cycle, where t plays the role of pumping parameter or time, and time-reversal symmetry is kept only at $t = 0$ and $t = T/2$. The wavefunction of the system can then be described by the Bloch states $|\psi_{nk}\rangle = e^{ikx}|u_{nk}\rangle$. The Berry connection of the system can then be written as

$$\mathcal{A}(k) = i \sum_n \langle u_{nk}|\partial_k|u_{nk}\rangle \qquad \text{2-7}$$

Under a certain gauge, the occupied states of the system can be written in pairs of $|u_{\alpha k}^I\rangle$ and $|u_{\alpha k}^{II}\rangle$ that satisfy:

$$|u_{\alpha,-k}^I\rangle = -e^{i\chi_{\alpha k}}\theta|u_{\alpha k}^{II}\rangle,$$
$$|u_{\alpha,-k}^{II}\rangle = e^{i\chi_{\alpha,-k}}\theta|u_{\alpha k}^I\rangle. \qquad \text{2-8}$$

Here $\alpha = 1, \dots, N/2$ denotes half of the N occupied states. The partial polarization of the system can then be written as:

$$P_\rho = \frac{1}{2\pi} \oint dk\mathcal{A}(k) = P_\rho^I + P_\rho^{II} \qquad \text{2-9}$$

The TRP is introduced as $P_\theta = P_\rho^I - P_\rho^{II}$, and the Z$_2$ invariant of the system is then written as

$$\mathbb{Z}_2 = P_\theta\left(\frac{T}{2}\right) - P_\theta(0) mod\ 2 \qquad \text{2-10}$$

Equation 2-10 can be rewritten in terms of the Wannier charge centers (WCC). The Wannier functions of unit cell R are defined as

$$|Rn\rangle = \frac{1}{2\pi} \int_{-\pi}^{\pi} dke^{-ik(R-x)}|u_{nk}\rangle. \qquad \text{2-11}$$

By definition, the WCC is the expectation value $\overline{x_n} = \langle 0n|\hat{x}|0n\rangle$ of the position operator $\hat{x}$ in the state $|0n\rangle$ in the hone unit cell $R = 0$. Recall that we have I and II pairs of eigenstates, which corresponds to $\overline{x}_\alpha^I$ and $\overline{x}_\alpha^{II}$, respectively, we will have

$$\mathbb{Z}_2 = \sum_\alpha \left[\overline{x}_\alpha^I\left(\frac{T}{2}\right) - \overline{x}_\alpha^{II}\left(\frac{T}{2}\right)\right] - \sum_\alpha [\overline{x}_\alpha^I(0) - \overline{x}_\alpha^{II}(0)] \qquad \text{2-12}$$

In practice, it is not necessary to directly compute equation 2-12. For non-trivial materials, the number of WCCs pairs that wind around the $(\overline{x},t)$ torus during the t=0->T/2 TRP procedure should be odd, thus one can directly give the $\mathbb{Z}_2$ of the system by inspection of the cross of the trajectories of WCC and WCC gap-center (Figure 2-5). Details of the algorithm should be referred to ref [88].
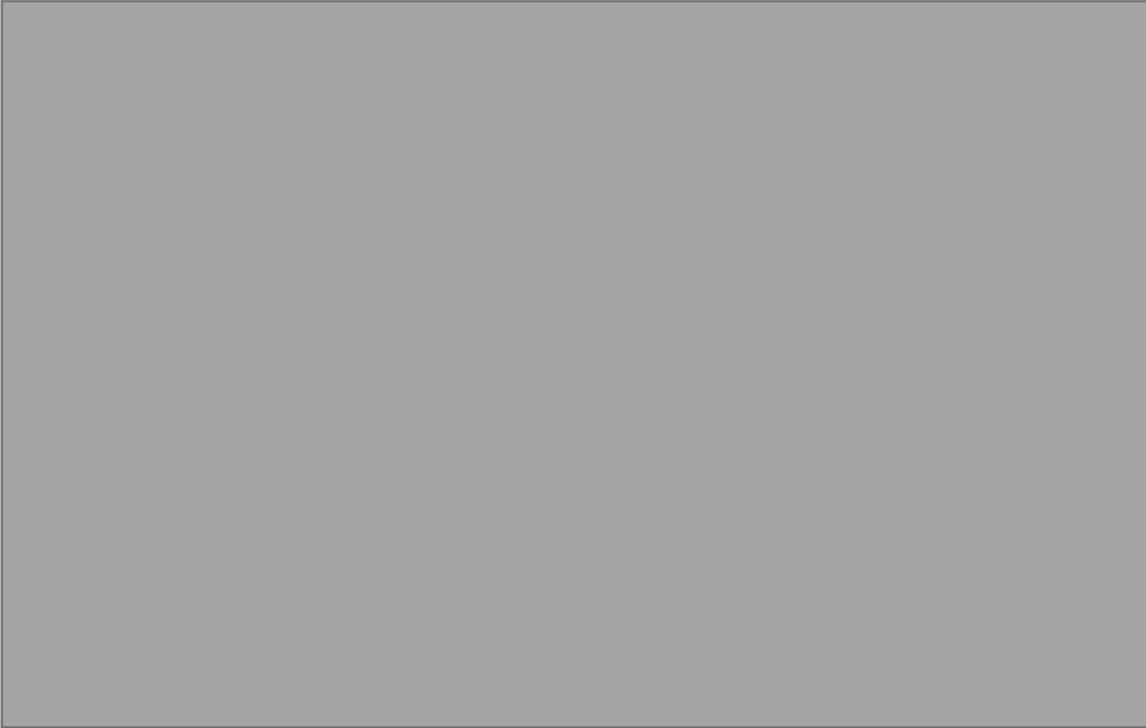
Figure 2-5: (From Ref. 88) Sketch of evolution of Wannier charge centers (WCCs) $\bar{x}$ vs. time t during an adiabatic pumping process. Regarding $\bar{x} \in [0,1$ as a unit circle and $t \in [0,T/2]$ as a line segment, the cylindrical ($\bar{x}$,t) manifold is represented via a sequence of circular cross sections at left, or as an unwrapped cylinder at right. Each red rhombus marks the middle of the largest gap between WCCs at given t. (a) $\mathbb{Z}_2$ insulator; WCCs wind around the cylinder. (b) Normal insulator; WCCs reconnect without wrapping the cylinder.

2.3. Materials search in 2D materials

As introduced above, the family of 2D materials drastically expands after the appearance of graphene, but there are still a lot of uncovered materials that are not well studied. However, to experimentally discover and investigate a certain 2D material is very time-consuming. Experimental study requires the synthesis of the material by methods such as chemical vapor deposition and van-der-Waals epitaxial growth, as well as characterization by relevant spectroscopy, such as X-ray surface diffraction, photoemission, low-energy electron diffraction, and scanning-tunneling spectroscopy.[91] Hence, experiments are good at making reliable and in-depth investigation for a certain system, but are difficult in systematical investigation of a large number of systems. Using experimental methods to achieve one of the goal of this dissertation, searching for the 2D substrates for germanene and stanene, might take very long time with few

findings.

On the contrary, computational methods are suitable and efficient for investigation of a lot of systems, as long as their chemical compositions and crystals are known. In combination with data-filtering techniques, computational methods have been applied in identifications of new scintillator materials, novel superconductors, topological insulators and 2D materials.[91–94] Among them, the data filtering of 2D materials from International Crystallographic Structural Database (ICSD)[95] by S. Lebègue *et al.* is typical and applicable to the 2D substrate search for germanene and stanene. [91] Since most of the compounds known as 2D (or layered 3D) materials have a bulk form where layers are held togethers by vdW forces, S. Lebègue *et al.* screen out materials on the basis of purely geometrical data by gradually refining the screening standard. Specifically, they first pick out materials with a low packing ratio, a parameter defined as sum of the volumes within the covalent radii of each atom in the cell divided by the total cell volume, of 0.15-0.50. A material with a low packing ratio means the material is more "loose", so it has a higher chance to be a layered material. In the second step, they list the compounds with large gaps (>2.4 Å) in the z direction of the crystal structure. In the last step, they inspect the geometric gaps along z and identify whether there could be covalent bonds within the geometric gap by calculating the

Table 2-1: (From Ref. 91) List of two-dimensional dichalcogenides found by S. Lebègue *et al.*.

distance between two atoms to the opposite side of the gap and comparing to the sum of the corresponding covalent radii. If no bonds are found, the material is likely to be 2D. Table 2-1 lists the 2D dichalcogenides found by the above algorithm. Finally the electronic properties of the 2D materials filtered out are examined by DFT.

The data filtering algorithm used by us in searching for the 2D substrate of germanene and stanene is similar but modified from the above one:

(1) Packing ratio is not used anymore in the first step. Instead, we choose those candidate substrates with similar lattice constant (<6% mismatch) to that of germanene/stanene. Furthermore, materials with heavy elements or ferromagnetic elements are excluded for the ease of calculation. The excluded elements are: Co, Cr, Fe, Mn, Mo, Ni, V, W, La, Ce, Pr, Nd, Pm, Sm, Eu, Gd, Tb, Dy, Ho, Er, Tm, Yb, Lu, Ac, Th, Pa, U, Np, Pu, Am, Cm, Bk, Cf, Es, Fm, Md, No, Lr, Rn, Fr, Ra, Rf, Db, Sg, Bh, Hs, Mt, Ds, Rg

(2) The same as the above method, the geometric gap along z is checked. The threshold is chosen to be 3.2 Å.

(3) An optimized covalent bonding check as the above method is utilized, which is more general and is not limited to z direction only. Specifically, a connection list is build from the atomic positions of the examined material by comparison of distances between atom pairs and the sum of corresponding covalent radii. Then, atoms that are connected to each other are grouped into clusters. By checking the ratio of number of clusters in 1x1x1 and 3x3x3 cell, one can judge the dimension of the material: 1 for 3D, 3 for 2D, 9 for 1D and 27 for 0D.

(4) Finally, DFT is used to examine whether the candidate 2D substrates is really suitable for germanene or stanene.

The detail of the algorithm will also be discussed in Chapter 4.

3. 2D substrates for germanene: Group-III monochalcogenides MX

3.1. Background

3.1.1. Substrate problem for germanene

Although germanene has various fascinating properties, some of which outperform graphene, it has a severe problem: the lack of suitable semiconducting substrates. In experiment, germanene has been synthesized on several metallic substrates, such as Pt(111), [24] Au(111), [25] and Al(111), [26] and only one semiconducting substrate, MoS_2. [36]

On metallic substrates, researchers fail to observe solid evidence of Dirac cone in germanene, probably due to the reconstruction of germanene induced by the relatively strong interaction between germanene and the substrate. For example, germanene on Al(111) surface is reconstructed to a 2×2 unicell due to the change of the height of Ge atoms (Figure 3-1). Likewise, germanene on Pt(111) surface is reconstructed to an even more disordered structure that the hexagonal ring is severely deformed to almost lost (Figure 3-2), [24] thus very unlikely to preserve the electronic structure of free-standing germanene. Besides, metallic substrates are unsuitable for many electronic applications, like the field effect transistor (FET). In FET, substrates are required to be insulating or semiconducting with a sufficient band gap to prevent current leakage of the channel material (i.e. germanene in this case). If the substrate is conducting, current will flow through the substrate even if the device is turned to the "off" state, resulting in a large off-state current and a ruined on-off ratio.

On the only semiconducting substrate MoS_2, germanene preserves a free-standing-like structure with hexagonal symmetry (Figure 3-3a) and possibly also the Dirac-cone-like band structure according to the DFT simulation based on their deduced structure (5×5 germanene on 6×6 MoS_2). [36] Nevertheless, the measured lattice constant of germanene on MoS_2, 3.86 Å, is significantly changed compared to the free-standing value ~4.0 Å. Such a large strain in MoS_2 makes germanene to be metallic due to the lift of eigenstates at the Γ point (Figure 3-3c). Remarkably, if a 27.8° rotated configuration of germanene on MoS_2 with <0.7% strain is used, the Dirac-cone-like band structure and the non-trivial topological phase in germanene can be well preserved.[37] Regretfully, such a configuration is not yet observed in experiment.

Figure 3-1: Structure of germanene synthesized on Al(111) surface. From Ref. 26.

Figure 3-2: Structure of germanene on Pt(111) surface. Light and median grey balls indicate lower and higher Ge atoms, respectively. Dark grey balls in the background are Pt atoms in the substrate. All figures are from Ref. 24.
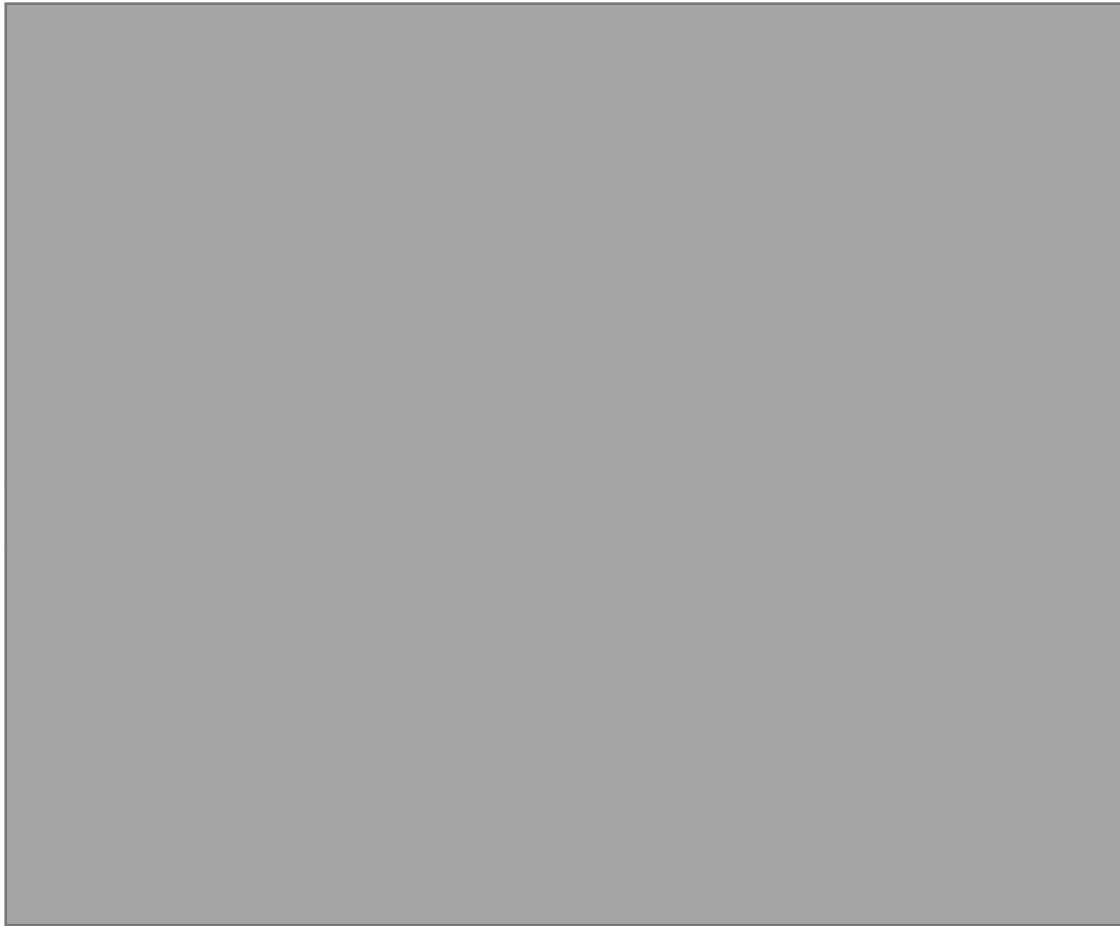
Figure 3-3: (a) STM image of germanene on MoS$_2$; (b) Density of states of germanene on MoS$_2$; (c) Band structure of the germanene part. Note that the lifting-up of eigenstates at the Γ point makes the utilization of the Dirac-cone difficult. All figures are from Ref. From Ref. 36.

There have been a few theoretical research attempts, mainly by using DFT, to find suitable substrates or to study the substrate interaction for germanene and stanene. In theory, many semiconducting substrates such as bare SiO$_2$ and GaAs will strongly interact with germanene and destroy its Dirac cone.[28,38] Substrates with a hydrogen passivated surface have been found to be promising to preserve the properties of germanene and its cousin materials. For example, Kokott *et.al.* have found that H passivated Si(111) and Ge(111) surfaces can serve as promising substrates for silicene, a cousin of germanene and stanene, to preserve the Dirac-cone.[96] Kaloni and Schwingenschlögl show that while the bare As-terminated GaAs(0001) surface will bond with germanene, germanene can preserve its buckled geometry and Dirac-cone like band structure on H passivated GaAs(0001) surface (Figure 3-4a~c).[38] For stanene, Matusalem *et al.* show that H-

passivated SiC(0001) could protect the Dirac-cone (Figure 3-4d~f).[97] On the other hand, suitable substrates without any surface passivation are few. By using DFT fitted tight binding low-energy Hamiltonian, Amlaki *et.al.* predict that germanene on MoS_2 can almost preserve the Dirac-cone, and the Z_2 invariant is dependent on the stacking angle between germanene and MoS_2.[37] Wang et.al. predict by DFT and model analysis that hexagonal boron nitride (h-BN) has little hybridization with silicene, germanene, and stanene.[20] Instead, h-BN induces topological phase transition in them and can form topological domain walls in them by using h-BN domains. [20]
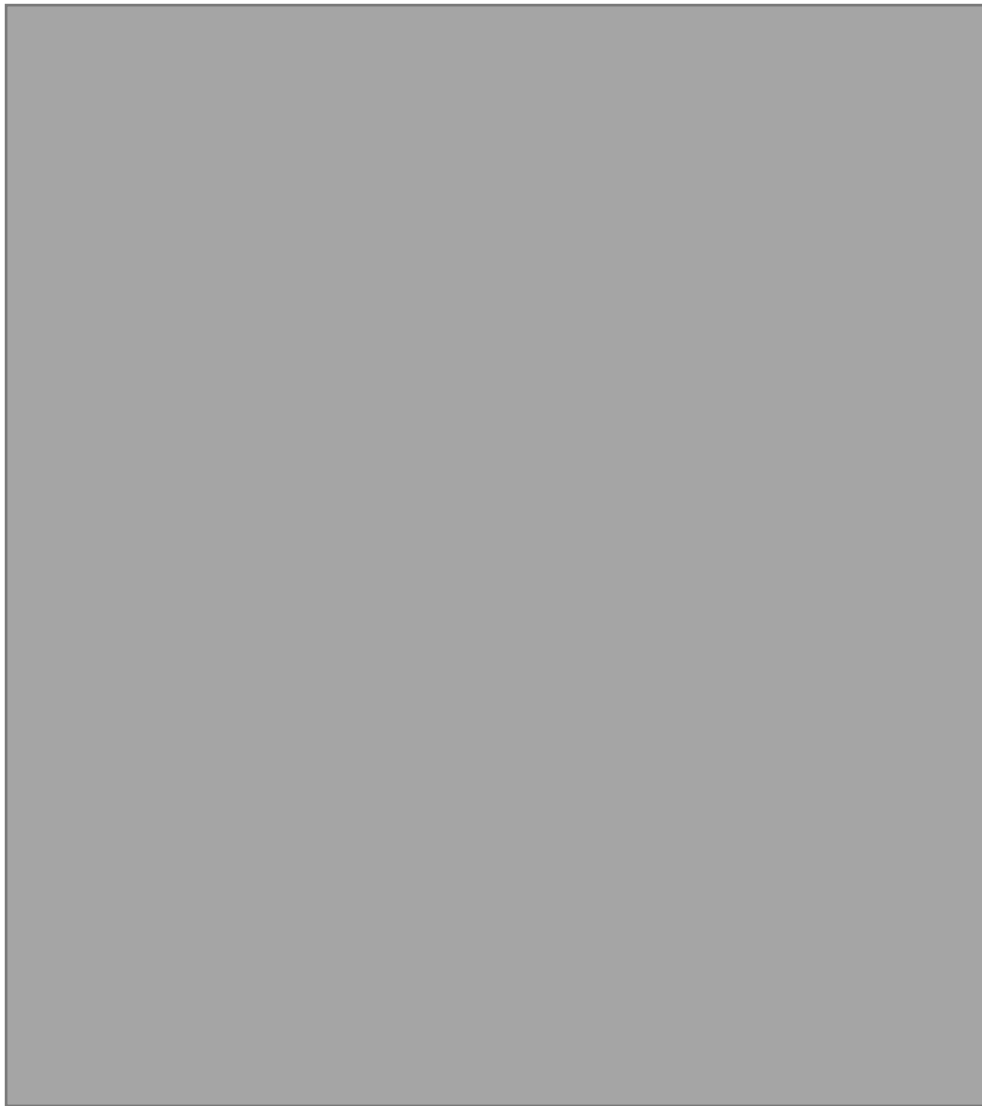
Figure 3-4: (a, b) Structures of germanene on (a) bare As-terminated and (b) H-terminated GaAs(0001); (c) Band structure of germanene on H-terminated GaAs(0001); (d) Stanene on H-terminated SiC(0001); (e, f) Band structure of stanene on (e) bare SiC and (f) H-terminated SiC(0001). (a-c) from Ref. 38. (d-f) from Ref. 97.

3.1.2. Group-III monochalcogenides

Group III monochalcogenides MX (M = Ga, In; X = S, Se, Te) in their 3D bulk form are layered materials stacked by vdW interaction and were previously studied for potential applications in energy converting field such as solar cells.[98] Great effort has been made in experiment to reduce their dimension to monolayer (ML) in experiment. Recently, ML and few-layer GaS [99,100], GaSe [99,101,102] and InSe [103] with an atomically flat surface has been successfully fabricated (Figure 3-5), making them a new family of 2D materials. By using DFT and HSE06 functional, ML MX are predicted to be semiconductor or even insulator with a large bandgap of 2 ~ 3 eV (Figure 3-6). [104] Some of the MX like GaS and GaSe are predicted to have weak interaction with silicene in theory.[105,106] With their clean surface and large band gap, ML MX seem promising to be the suitable substrates for germanene, the interaction between them and germanene is yet to be investigated.

Figure 3-5: (a, b) AFM image of (a) few-layer InSe and (b) ML InSe. From Ref. 103. (c) STM image of ML GaSe. From Ref. 102.

Figure 3-6: Positions of band edge in monolayer intrinsic MX with respect to the vacuum level calculated with the HSE06 functional. The band edge of monolayer MoS_2 is also given for reference. The standard redox potentials for water splitting at pH = 0 are shown as dashed lines for comparison. Insets are structures of monolayer MX. From Ref. 104.

3.2. Computational details

We use the DFT method implemented in Quantum ESPRESSO[107] to do geometry optimization and electronic structure calculation and VASP[108] to do hybrid functional calculation. In Quantum ESPRESSO calculation, ultrasoft pseudopotentials with nonlinear core correction are employed. The optB86b-vdw[78,80–82] exchange-correlation functional is used in geometry optimization to take the van der Waals interaction into account. The generalized gradient approximation exchange-correlation functional of the Perdew, Burke, and Ernzerhof (PBE) parametrization[69] is used in electronic structure calculation with spin-orbital coupling (SOC). The energy cutoffs are chosen to be 952, 952, 1360, 816 eV for GaS, GaSe, GaTe and InSe, respectively, after convergence test. A Monkhorst-Pack[109] (MP) k-point grid of $21 \times 21 \times 1$ is chosen. The dipole correction[110] is engaged and found to have negligible influence in our system. In VASP calculation, the projected augmented wave (PAW) [111] pseudopotential is employed. The Heyd-Scuseria-Ernzerhof (HSE) functional [70,71,73] is used in hybrid functional calculation without SOC due to computational overburden. The corresponding MP k-point and q-point grids are both

$27 \times 27 \times 1$. The q-point grid is used in calculating the non-local Fock exchange energy $E_x^{HF} = -\frac{e^2}{2} \sum_{nk,mq} f_{nk} f_{mq} \times \iint d^3\vec{r} d^3\vec{r}' \frac{<nk\vec{r},mq\vec{r}'|nk\vec{r}',mq\vec{r}>}{|\vec{r}-\vec{r}'|}$, where k and q sum over the grid of k-(q-)points that samples the Brillouin zone; m, n denote the band number; f_{nk} is the occupation number of $|nk>$.[112]

3.3. Results of germanene on MX

3.3.1. Structure and stacking configuration

The initial structures of free standing ML MX ((GaS, GaSe, GaTe and InSe)) and germanene are adopted from previous literature [17,104] (Figure 3-7a and b). They have similar honeycomb structures and lattice constants of 3.58 ~ 4.06 Å, not far from that of germanene (4.02 Å), so only the 1×1 stacking (Figure 3-7e) is considered in this work. There are three high symmetric points in one hexagonal cell and two different atoms in germanene after stacking, so there are $\binom{3}{2} = 6$ high symmetric stacking configurations in total (Figure 3-7c). The six configurations are characterized by their stacking mode (AA or AB) and the type of the Ge atom (top "t" or bottom "b") which overlaps the substrate atom (metal M or chalcogen X) in the top view: AA-t (AA-X-t or AA-M-b), AA-b (AA-X-b or AA-M-t), AB-M-t, AB-M-b, AB-X-t, and AB-X-b.

We begin from the investigation of the most energetically favorable configurations of germanene on ML MX. First, the lattice constant is determined. We choose one stacking configuration (AA-t) to obtain the most preferable lattice constant and apply it to the other configurations. The optimized lattice constant is shown in Table 3-1. GaS and GaSe have smaller lattice constant with germanene than in their free standing or bulk case, while GaTe and InSe are almost unchanged. This is probably due to the fact that the free standing germanene is predicted to have a lattice constant of 3.97 ~ 4.03 Å [17,33], larger than those of GaS and GaSe and close to those of GaTe and InSe. The lattice constant of germanene on GaTe with AB-M-b configuration is also examined and the result is similar to the above. Second, we fix the lattice constant and optimize the geometry using all the six configurations as the initial ones. The configuration with the lowest energy is found the same for all the four MX, which is shown in Figure 3-7d and e and is named as the AB-M-b configuration (AB stacking, M atom above b-Ge). The total energy differences between the most favorable configuration and the others, which are presented in Figure 3-7f, are about 0.1 eV except for the AB-M-t configuration. Although the energy difference

between AB-M-b and AB-M-t configurations is only ~0.02 eV, they cannot be easily transformed into each other. This is because they are not related by any in-plain translation but a space (to p37)
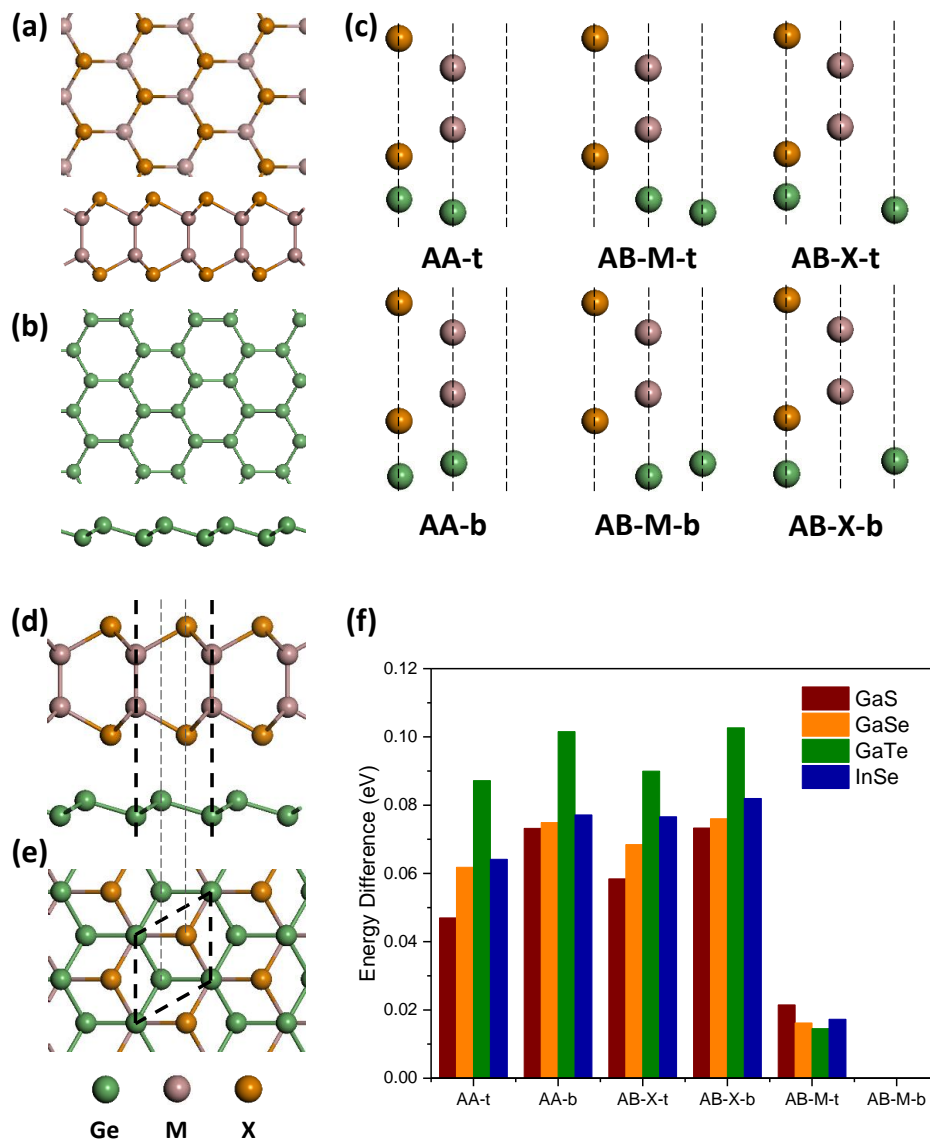
Figure 3-7: Top and side views of free standing ML (a) MX and (b) germanene. (c) All the six high symmetric stacking configurations of germanene on MX. (d) Side and (e) top views of 1×1 stacked ML germanene and MX with the most preferable stacking. Thick dashed lines denote the lattice, and thin dashed lines denote the high symmetric positions in hexagonal cells. M = Ga, In; X = S, Se, Te. (f) Energy difference between AB-M-b configuration and the other configurations.
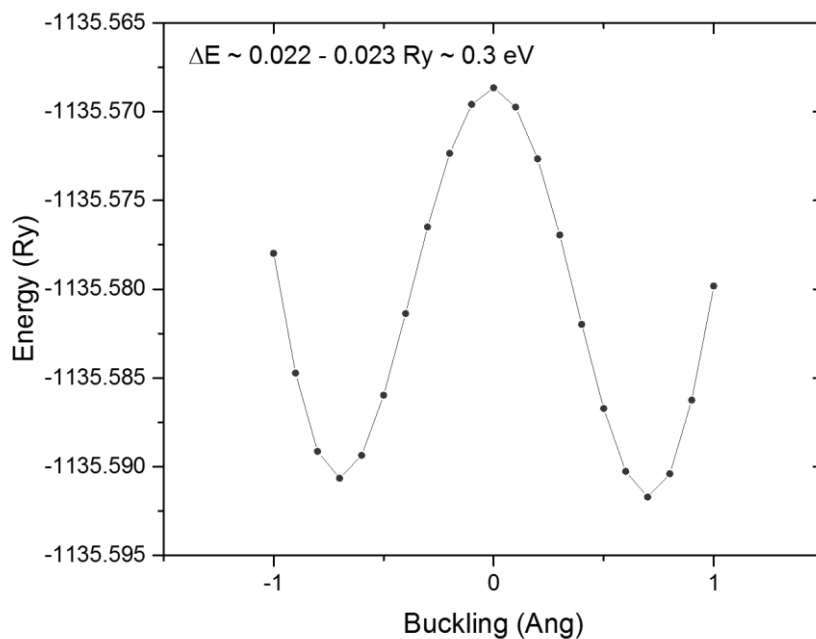
Figure 3-8: Total energy of germanene on GaTe with different buckling height. The whole system is geometrically optimized while germanene is fixed. The left and right minimums correspond to AB-M-t and AB-M-b configurations, respectively.
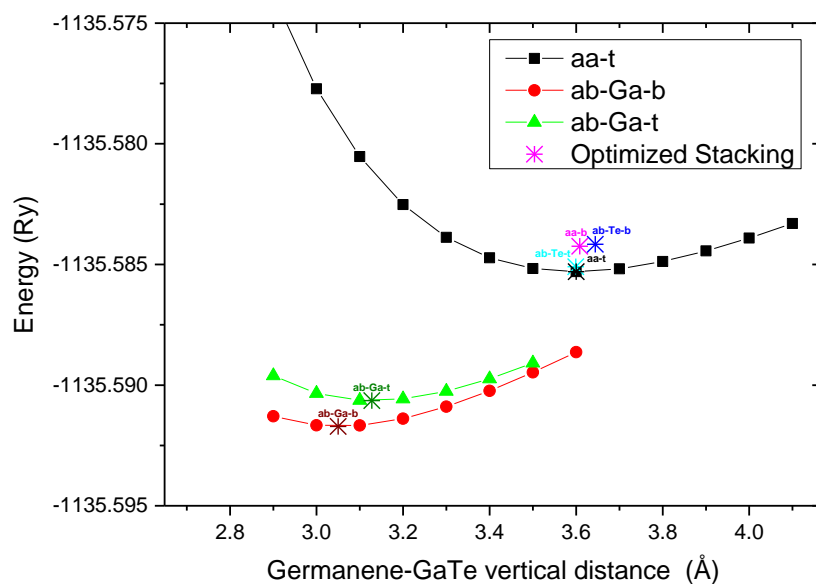
Figure 3-9: Total energy of GaTe-germanene system with all 6 kinds of stacking. Stars denote the energy given by geometry optimization. Lines denote the energy change by changing the vertical distance between optimized and fixed germanene and GaTe.

inversion of the germanene part, and the transformation energy barrier between them is about 0.3 eV (Figure 3-8). The diagram of total energy vs. the distance between germanene and GaTe at the six high symmetric stacking configurations further proves that the geometry optimization is reliable and the most stable configuration in them is indeed ab-M-b (Figure 3-9). Other non-high-symmetric configurations are also considered for germanene on GaTe and are found to be less favorable (Figure 3-10). Hence, we focus on the AB-M-b stacking of germanene on all kinds of ML MX in the followings. The vertical distance between MX and germanene is 2.90 ~ 3.05 Å, and the nearest distance between Ge atom and X atom is about 3.63 ~ 3.85 Å. Such a far distance suggests the weak interaction between germanene and MX substrates. The buckling of germanene is enhanced from the free-standing value of 0.64 ~ 0.69 Å [17,28,33] to 0.77 ~ 0.89 Å on GaS and GaSe, which can be understood easily from the smaller lattice constant than in the free-standing case. However, the germanene's buckling is still slightly enhanced to 0.71 Å on GaTe and InSe, where the lattice constants are larger than that of the free-standing germanene. This implies that the interaction between substrate and germanene is non-negligible.
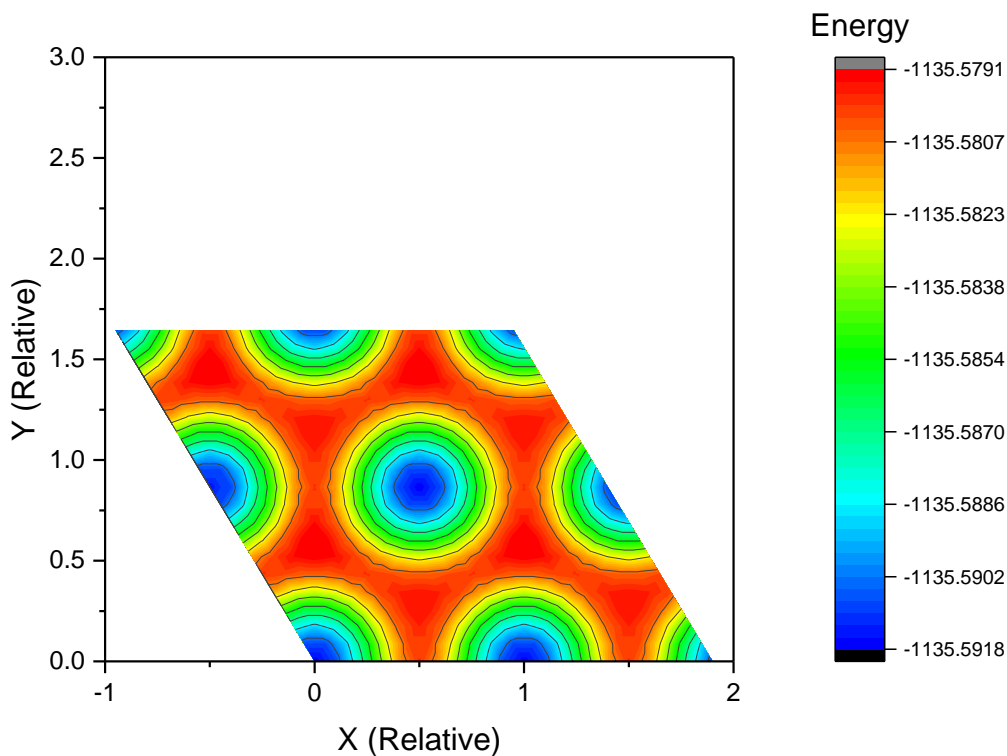
Figure 3-10: Energy map of germanene on GaTe with different lateral relative position while keeping the vertical distance between germanene and GaTe. The configuration at X=Y=0 is the AB-M-b configuration. The unit of energy is Ry.

Table 3-1: Structural parameters of bulk MX in experiments, ML MX in theory from previous literature, and germanene on ML MX in this work. Experimental data are provided by the Inorganic Crystal Structure Database (ICSD) [95].

	MX only		germanene-MX		
	lattice (Å)		lattice (Å)	z-distance (Å)	germanene buckling (Å)
	Bulk experiment	ML DFT (HSE)	ML This work		
GaS	3.59	3.58	3.78	2.90	0.89
GaSe	3.74~3.76	3.75	3.89	2.99	0.77
GaTe	4.06	4.06	4.06	3.05	0.71
InSe	4.00~4.05	4.02	4.03	2.92	0.71

3.3.2. Electronic structure and effective mass.

Next we investigate whether germanene also has a well-preserved electronic structure. The charge transfer from germanene to MX estimated using the Bader charge analysis [113–115] are as small as 0.02 (GaTe and GaSe), 0.03 (InSe) and 0.04 (GaS) electrons (Table 3-2). Since the total dipole is mainly induced by the charge transfer, the strength of the dipole correction in the Hartree potential is in the same sequence as above, specifically 0.03 (GaTe) < 0.08 (GaSe) < 0.14 (InSe) < 0.23 (GaS) eV/Å (Table 3-2 and Figure 3-13). The differential charge densities $\rho_{diff} = \rho_{germanene\text{-}MX} - \rho_{germanene} - \rho_{MX}$ (shown in Figure 3-15) reveal that the charge density in the interspace between germanene and MX increases, while the density near both Ge and X atoms decreases.

The band structures of germanene on ML MX are presented in Figure 3-11. All of the four compound systems have Dirac-cone-like band structures at the K-point with a "gap" opened (named as the Dirac-gap to prevent confusion with the band gap). Such Dirac-gap can be attributed to germanene according to the projected band structure shown in the left panel of Figure 3-11, which shows the Ge contribution is over 89% at the Dirac point of germanene and rule out the possibility that these states mainly come from the MX substrates. The Dirac-gap appears in germanene on all kinds of MX, but only germanene on GaTe and InSe is actually semiconducting. Germanene on GaS and GaSe is metallic due to the bands crossing the Fermi level near the Γ-point. This metallic behavior is caused by the cooperation of the deformation of germanene and

the interaction with the MX substrate. Germanene on GaS and GaSe in a 1x1 cell has a compressive strain of 6% and 3%, respectively. As mentioned previously, germanene changes from Dirac material to metal under a compressive strain beyond 5% due to the band lifting at the Γ-point ("self-induced doping"), though no Dirac-gap opens.[116] The band structures of the germanene-part of the germanene-GaS and -GaSe systems have similar band lifting at the Γ-point (Figure 3-14). It is worth mentioning that germanene on GaTe and InSe also has a little band lifting at the Γ-point in spite of the fact that the strain is no larger than 1% (Figure 3-14), which can only be explained by the interaction between germanene and MX.

Table 3-2: Charge transfer from germanene to MX in number of electrons, and the Dirac-gap, SOC-split and effective masses at the Dirac point of germanene on MX. Note that although germanene has a gap at the Dirac point on GaS and GaSe, it is still metal due to the band lifting near the Γ point crossing the Fermi level, so their gap sizes and effective masses have no practical meaning except for comparison.

		GaS	GaSe	GaTe	InSe
Charge transfer (e)		0.04	0.02	0.02	0.03
Dipole correction (eV/Å)		0.23	0.08	0.03	0.14
Dirac-gap (eV)	PBE	0.14	0.13	0.12	0.11
	PBE+SOC	0.11	0.10	0.10	0.08
	HSE	0.18	0.16	0.16	0.14
SOC-split (eV)	Conduction band	0.030	0.024	0.015	0.021
	Valence band	0.034	0.028	0.024	0.042
$m^{*}_{\Gamma K}$ (m_0)	$m^{*}_{h\_h}$	0.089	0.078	0.081	0.080
	$m^{*}_{h\_l}$	0.061	0.056	0.062	0.050
	$m^{*}_{e\_l}$	0.060	0.055	0.059	0.049
	$m^{*}_{e\_h}$	0.088	0.076	0.076	0.076
m^{*}_{KM} (m_0)	$m^{*}_{h\_h}$	0.087	0.078	0.078	0.078
	$m^{*}_{h\_l}$	0.057	0.051	0.058	0.044
	$m^{*}_{e\_l}$	0.056	0.051	0.054	0.043
	$m^{*}_{e\_h}$	0.088	0.075	0.073	0.074
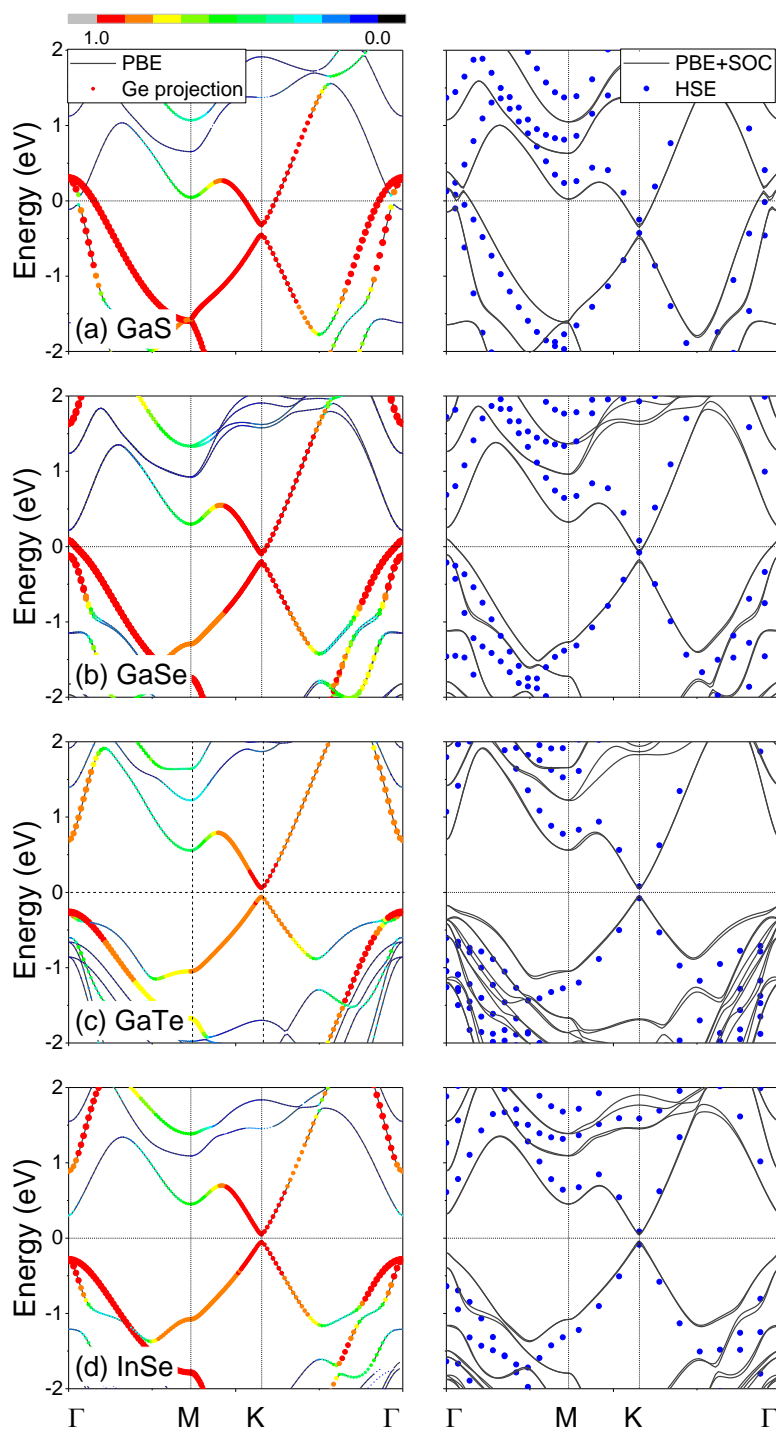
Figure 3-11: Band structures of germanene on (a) GaS, (b) GaSe, (c) GaTe and (d) InSe. The left panel is the band structures obtained using the PBE functional (black lines) and the Ge projections (size indicates the absolute projection value, and color indicates the percentage of Ge contribution in total with red standing for 90% ~ 100%), and the right panel is the band structures obtained using the PBE + SOC (black lines) and HSE without SOC (blue dots).

The size of the Dirac-gaps in germanene on different MX are summarized in Table 3-2. In general, the Dirac-gap of germanene on MX decreases in the order of GaS > GaSe > GaTe > InSe from 0.14 to 0.11 eV when estimated using the PBE functional without SOC. The opening of the Dirac-gap can be attributed to the breaking of the inversion symmetry by introducing the MX substrate, similar to the band gap opening in germanene by the vertical electric field [28]. If the SOC is considered in calculations with the PBE functional, the conduction and valence bands split into two bands by 0.02 ~ 0.04 eV (Table 3-2, Figure 3-11 and Figure 3-12), respectively, involving the Dirac-gap decrease by 0.02 ~ 0.03 eV. Moreover, it is well known that DFT can underestimate the actual band gap of semiconductors by up to 50%. The use of hybrid functional, which includes a certain amount of the Hartree-Fock exchange, can yield much improved band gap values compared with the GGA functionals.[70] As shown in Table 3-2, the Dirac-gap given by the HSE hybrid functional is about 0.16 ~ 0.18 eV, ~25% larger than the PBE cases. The actual band gap of germanene on MX should be a little smaller than the HSE band gap due to the SOC splitting. Regretfully, the HSE calculation including SOC is not feasible within out available computational resource. Assuming that the SOC splitting is the same as the PBE calculation results, we estimate the actual Dirac gap to be around 0.1 eV. In the cases of germanene on GaTe and InSe, the 0.1 eV Dirac-gap also corresponds to the band gap. If combined with other band-gap-opening techniques, such as the application of vertical electric field [28] and the surface atom adsorption [30], the band gap in these cases could possibly reach 0.4 eV, which is the minimum requirement as the channel
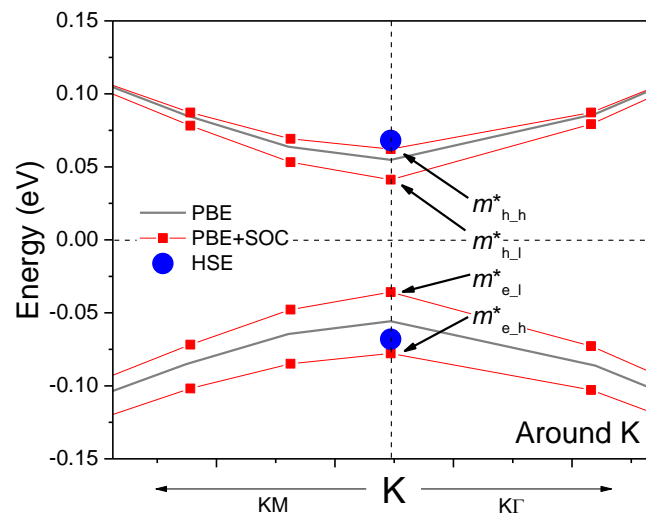
Figure 3-12: Detail of the band structure of germanene on InSe near the Fermi level (dashed horizontal line) and *K* point.

material of field effect transistors [117]. Note that contrary to the result given by the PBE functional, germanene on GaSe is predicted to be also semiconducting by the HSE calculation with a band gap of 0.16 eV. The reason is that the valence band at the Γ point is lowered to about 0.2 eV below the Fermi level in the HSE calculation, while the same band in the PBE calculation is above the Fermi level. Such a phenomenon of the lowered valence band at the Γ point in HSE calculations can also be found in other MX substrates (right panel of Figure 3-11).
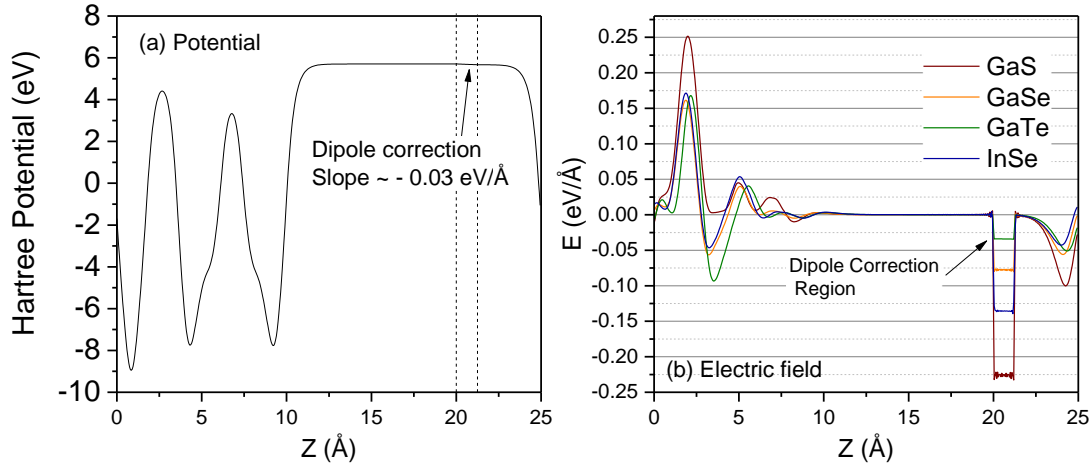
Figure 3-13: (a) Potential diagram averaged in the XY-plain along Z-direction of the germanene-GaTe system. (b) Electric field diagram of averaged in the XY-plain along Z-direction of the germanene-MX system. The electric field is the differential of the differential potential, i.e.

$$\frac{d(P_{germanene\text{-}MX} - P_{germanene} - P_{MX})}{dZ} \; .$$

Although a band gap opens, germanene still has ultrahigh carrier mobility on GaTe and InSe as shown below. The SOC splitting introduces extra effective masses compared to non-SOC cases, namely the heavy hole/electron masses $m^*_{h\_h}/m^*_{e\_h}$ and light hole/electron masses $m^*_{h\_l}/m^*_{e\_l}$ along KM and KΓ direction (Figure 3-12). The calculated effective masses are listed in Table 3-2. The light m^* along KM remains as small as ~0.05 m_0, where m_0 is the free electron mass, on GaTe and ~ 0.04 m_0 on InSe, and the heavy m^* are just about 0.01 m_0 higher. The m^* along KΓ is only 0.004~0.006 m_0 larger than the corresponding m^* along KM, so they can be treated as almost the same. Given that the relaxation time τ is the same as that of the free-standing germanene, about 5.3 ps, [33] the mobility in germanene calculated by $\mu = e\tau / m^*$ can be up to 1.5 and 2.2 $\times 10^5$ cm^{2}V^{-1}s^{-1} for light carriers, and still above 1.2 $\times 10^5$ cm^{2}V^{-1}s^{-1} for heavy carriers. The light carrier

mobility is close to the best value of graphene obtained in suspended samples in experiment, around 2×10^5 cm^{2}V^{-1}s^{-1} [118], and the intrinsic carrier mobility of free-standing graphene ($3.2 \sim 3.5 \times 10^5$ cm^{2}V^{-1}s^{-1}) and silicene ($2.2 \sim 2.6 \times 10^5$ cm^{2}V^{-1}s^{-1}) by theory. [33] Without suitable substrate, for example when graphene is put on substrate like SiO$_2$, its carrier mobility will drop to 10^4 cm^{2}V^{-1}s^{-1} or lower. [119] In addition, the high mobility in graphene and silicene will degrade significantly if a band gap of over 0.1 eV is opened. [120,121]
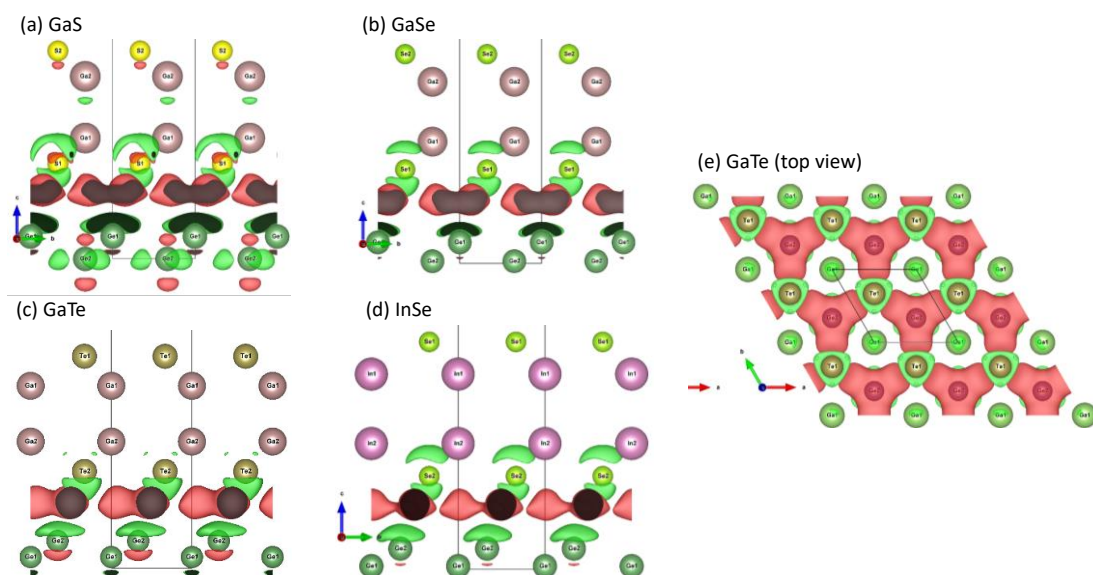
Figure 3-15: Differential charge density of germanene-MX systems. Ge atoms are in the bottom part of each figure and are colored in dark green. The isosurface is chosen as 0.0025. Red and green colors indicate positive and negative values, respectively.
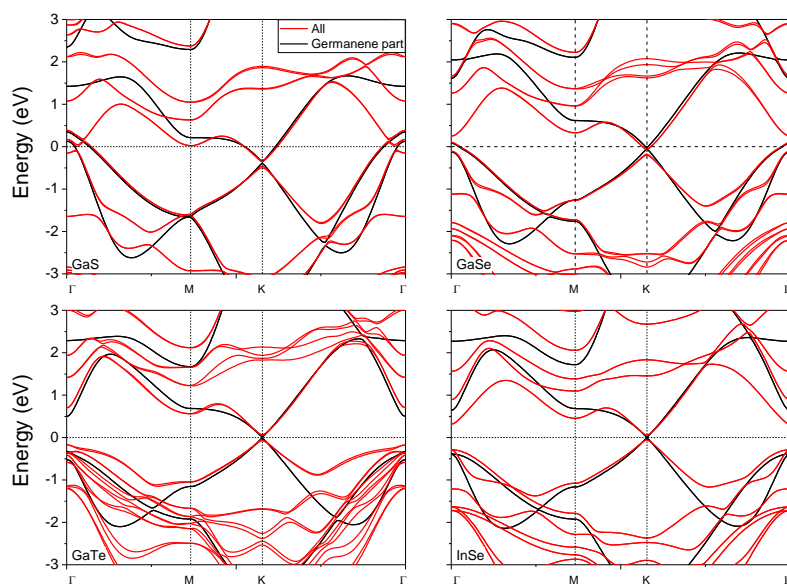
Figure 3-14: Band structure of Germanene-MX systems and the germanene parts only. The band structure of the corresponding germanene part is calculated by simply removing the MX part to see the effect of deformation on germanene.

3.3.3. Discussion on the effect of temperature

Admittedly, we have ignored the possible increase of relaxation time induced by phonon in our previous analysis of effective masses in germanene. The effect of phonon is not negligible at room temperature. As shown in Figure 3-16, molecular dynamics simulation at 500K reveals that germanene can preserve its 2D order in the *xy*-plane and its hexagonal lattice well on GaTe. On the contrary, germanene's buckling in the *z* direction, shown in Figure 3-16c, will oscillate irregularly with an amplitude of around 0.5 Å from the equilibrium position, indicating that the effect of electron-phonon interaction of ZA and ZO phonon should not be neglected at high temperature. The relaxation time of germanene Nevertheless, at low temperature the effect of phonon could be negligible. Since phonon obeys the Bose-Einstein distribution that the average number of phonon of frequency ω equals $\langle n \rangle = \dfrac{1}{\exp\left(\frac{\hbar\omega}{k_b T}\right)-1}$, the number of phonon will approach zero as the temperature approaches zero. We believe it is meaningful to show the ideal properties of germanene on these substrates at low temperature limit to reveal its great potential for electronic devices.
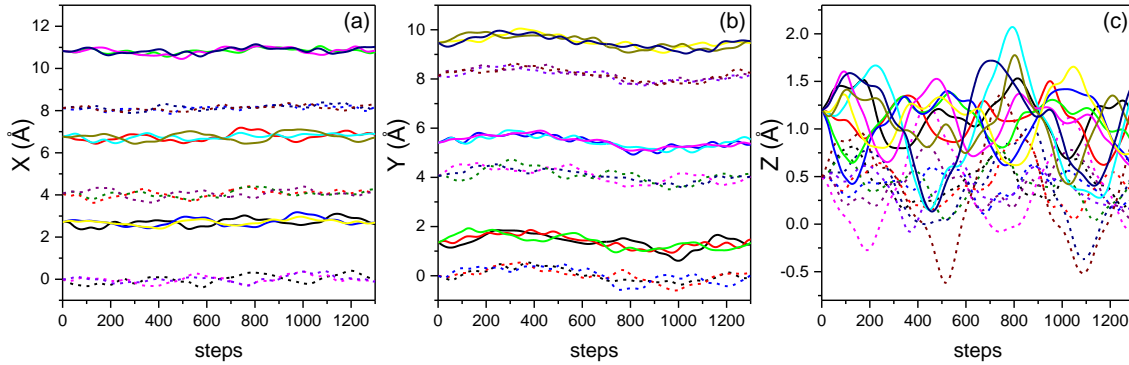
Figure 3-16: (a) *x*, (b) *y*, and (c) *z* coordinates of all Ge atoms at every step of molecular dynamics simulation of germanene on GaTe at 500K. A 3 x 3 supercell is used in the simulation, so there are 18 Ge atoms in total. Solid lines stands for those Ge atoms that start at a lower Z position ("bottom" Ge), while dashed lines for those at a higher Z position ("top" Ge). One step is 1.5 fs. Note that the X and Y positions of Ge atoms oscillates around their initial positions, indicating a rather stable configuration. On the other hand, the Z position of Ge atoms changes more greatly and sometimes local flipping of "top" and "bottom" Ge happens. Although the non-local flipping (flipping of all "top" and "bottom" Ge) is proved to have large energy barrier of 0.3 eV previously,

local flipping engages less atoms and experiences much lowered energy barrier, making it possible to happen. The molecular dynamics simulation is performed by VASP in a 3×3 supercell under 500 K using the Nosé–Hoover canonic thermostat.

3.4. Conclusion

In conclusion, for the first time by using the density function theory, we predict that germanene can preserve its low-buckled honeycomb structure and the Dirac-cone-like band structure similar to the free-standing case. Furthermore, germanene is predicted to be semiconducting on GaTe and InSe with a band gap of over 0.1 eV, while an ultrahigh carrier mobility estimated up to 2.2×10^5 cm^{2}V^{-1}s^{-1} at low temperature limit is preserved. The band splitting caused by the SOC can be up to 42 meV. Hence, we believe germanene on GaTe and InSe, which has <1 % lattice mismatch with germanene, has potential in electronic and spintronic applications. On the other hand, GaS and GaSe will induce the metallic transition of 1×1 stacked germanene due to their larger lattice mismatch of 12% and 8%, respectively. Our research would stimulate the synthesis of high-performance germanene and its FET in the future.

4. 2D substrates for germanene and stanene by materials search

4.1. Introduction

As mentioned previously, germanene still lacks suitable semiconducting substrates that can preserve their bulked honeycomb structure, Dirac-cone and semiconducting nature. Besides, stanene also has such substrate problem. For example, the stanene synthesized on Bi_2Te_3 is metallic instead of semiconducting (Figure 1-5g). Using 2D layers from 3D layered materials as the substrate can be a possible solution and has several advantages. 3D layered materials have weaker interaction between each layer compared to three-dimensional materials, which may help in protecting the structural integrity of germanene and stanene. 2D substrates from 3D layered materials can also be directly used in the fabrication of the vertical layer-by-layer heterostructure and vertical field effect transistor.[122,123] In Chapter 3 we proposed that 2D GaTe and InSe can be potential suitable substrate for germanene, and later another group proposed that they are also suitable for stanene.[124,125] Nevertheless, such human selection of substrate candidates by experience, both in experimental and theoretical researches, is of less efficiency. If an automatic substrate searching routine can be developed, it will not only speed up the substrate exploration of germanene, but also be widely applicable to other 2D targets similar to germanene like stanene.

Another problem is that the effect of substrate on the electronic state and Z_2 topological indexes of supported germanene and stanene remain to be investigated systematically. Germanene and stanene should be supported or protected by solid substrates in practice, so substrate effect should be thoroughly investigated. Nevertheless, currently only the Z_2 invariant of germanene on MoS_2, h-BN, and Al_2O_3, and that of stanene on InSe, GaTe, and Ge(111) have been studied.[20,37,39,125,126] The researches are quite separated without generating any universal rule for the substrate effect. Whether germanene and stanene have different topological phases on other substrates and how to explain the interaction between germanene/stanene and 2D substrates in general are still open questions.

In this work, for the first time by using density functional theory (DFT) and materials informatics, we have dug out several suitable 2D semiconducting substrates for germanene and stanene, including some of the CdI2-type materials, GeI$_2$, CuI and GaGeTe, from the Inorganic

Crystal Structure Database (ICSD).[95] After mining and screening by our home-made program, the structural and electronic behaviors of monolayer germanene/stanene on the selected candidate substrates are investigate by using DFT. On these suitable substrates, germanene and stanene are found to be able to preserve quasi-free-standing geometries and Dirac-cone-like band structures with a band gap of 0.002~0.185 eV opened. The stability of the supported germanene and stanene is examined by phonon calculations. In addition, we have performed systematic investigation on the Z_2 topological index of the supported germanene and stanene, and have found that they can even preserve their non-trivial Z_2 topological index on CuI and CaI_2, respectively. On the other substrates, germanene and stanene become trivial band insulators, even though the interaction with substrates are van-der-Waals-like. Furthermore, we have demonstrated that the interaction between germanene/stanene and the substrates can be well explained by the low energy Hamiltonian of free-standing germanene/stanene under uniform external fields.

4.2. Methodology

The procedure of the selection of suitable substrate candidates is shown in Figure 4-1. On the basis of the experience gained in Chapter 3, we select the substrates that:

(1) exist in experiment at room temperature and atmospheric pressure;

(2) have similar symmetries (hexagonal lattice) and lattice constants (mismatch < 6%) with those of germanene/stanene;

(3) are likely to be 2D materials or 3D layered materials judged by our home made program explained below.

(4) does not contain heavy and magnetic elements, including Co, Cr, Fe, Mn, Mo, Ni, V, W and La-Ac series elements. This criterion is added in order to simplify the DFT examination procedure. Heavy elements and magnetic elements sometimes require case-by-case treatment like DFT+U and correct initial guess of magnetism, so they are not suitable for uniform automatic DFT calculations.

We use our home-made program to filter out such materials from ICSD and get the Crystallographic Information Framework (CIF) structure files, where CIF is a standard file structure for crystallographic information developed by the International Union of Crystallography Working Party on Crystallographic Information. [127] Then, inspired by the idea of data mining of 2D materials in ICSD,[91] we use our home-made program to filter out suitable 2D substrate candidates from ICSD for germanene and stanene. In Ref. [91], the authors first filter out

the materials with > 2.4 Å gap between crystallographic planes along the *c* axis (*z*-direction). Then in the next step, the authors further check whether there is covalent bond within the gap by comparing the distance between atoms on both sides of the gap with the sum of covalent radii of corresponding elements. In this work, the first step is similar; we use an interlayer distance criterion of 3.2 Å to select those materials with large vacuum in the z-direction. The larger criterion of the vacuum is to enhance the chance to find layered materials with weaker interlayer interaction. In the second step, we do not only check the atoms on both sides of the vacuum. The candidate of suitable substrate found in the first step is doubly checked by another algorithm: first, we make the bonding check between all atom pairs in the material to build a connection table. The bonding check is made by comparison of the distance between two atoms and the sum of the covalent radii of the elements from the database in Mathematica times 1.33 (an empirical
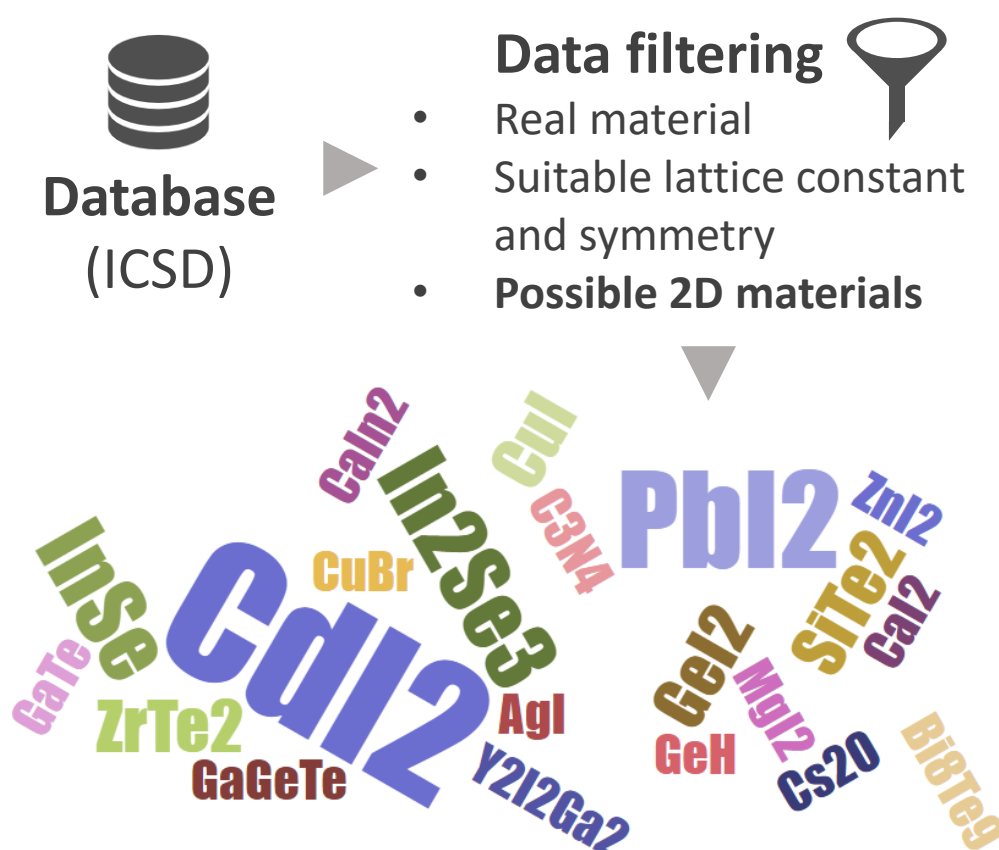
Figure 4-1: Schematic of the selection of the substrates for germanene and stanene from ICSD to be examined by DFT. The whole selection is done automatically. Size of formulas in the figure below indicates the number of entries found in ICSD (Table 4-1), which we believe is related to the commonness of the material.

coefficient to count all ambiguous interatomic distances as connected); then, we separate the atoms into groups based on whether they are connected or not and determine its dimensionality by the comparison between the number of groups in the primitive cell and the 3×3×3 supercell. The second step in this work can be used alone to filter out any layered material whose stacking direction is not necessarily oriented at the c axis. The bulk structures of the suitable substrates found in this work are shown in Figure 4-4, which are all likely to be 3D layered materials.

Table 4-1: Number of ICSD entries found by datamining. Grey cells are unsuitable substrates.

Germanene	ZnI_2	CdI_2	GeI_2	GaGeTe	MgI_2	CuI	GaTe	InSe
ICSD entries	1	214	2	1	1	2	1	5
Germanene	CuBr	$ZrTe_2$	$Y_2I_2Ga_2$	In_2Se_3	$SiTe_2$	Cs_2O	GeH	
ICSD entries	1	2	1	5	2	1	1	
Stanene	PbI_2	CaI_2	AgI	Bi_8Te_9	$CaIn_2$			
ICSD entries	23	1	1	1	1			

After selection, the DFT method implemented in Quantum ESPRESSO is used to examine the properties of germanene and stanene on their corresponding substrate candidates,[107] and a home-made program is used for the automation of extensive DFT calculations. Projector augmented wave (PAW) pseudopotentials from PSlibrary are employed in geometry optimization, band structure and phonon dispersion calculations.[111,128] For each element, we select the pseudopotential with the highest suggested energy cutoff and use such cutoff in our calculation. The optB86b-vdW exchange-correlation functional is used in geometry optimization to take the van der Waals interaction into account.[78,80–82] The generalized gradient approximation (GGA) exchange-correlation functional of the Perdew, Burke, and Ernzerhof (PBE) parametrization is utilized in electronic structure calculations with spin-orbit coupling (SOC).[69] A Monkhorst-Pack (MP) k-point grid of $21 \times 21 \times 1$ is chosen for all systems after test,[109] since our target systems have similar lattice constants. The energy and force convergence tolerant are set to 1×10^{-5} Ry and 2×10^{-4} Ry/Å, respectively. We do not perform variable-cell optimization, so the pressure convergence is not necessary. Dipole correction is applied and found to have negligible influence in our systems.[110] Phonon calculations are performed by using density functional perturbation theory (DFPT) implemented in Quantum ESPRESSO with a q-point grid of $5 \times 5 \times 1$.[107] Norm-conserving pseudopotentials generated by Optimized Norm-Conserving (NC) Vanderbilt PSeudopotential (ONCVPSP) using SIG15 dataset are employed in Z_2 invariant calculations

implemented in Z2pack supported by Wannier90 after test.[88,129–133] In the test, band structures of germanene on CuI and CdI_2 by using NC pseudopotential (PP) are found to be almost identical to those calculated by ultra soft (US) PP (Figure 4-2).
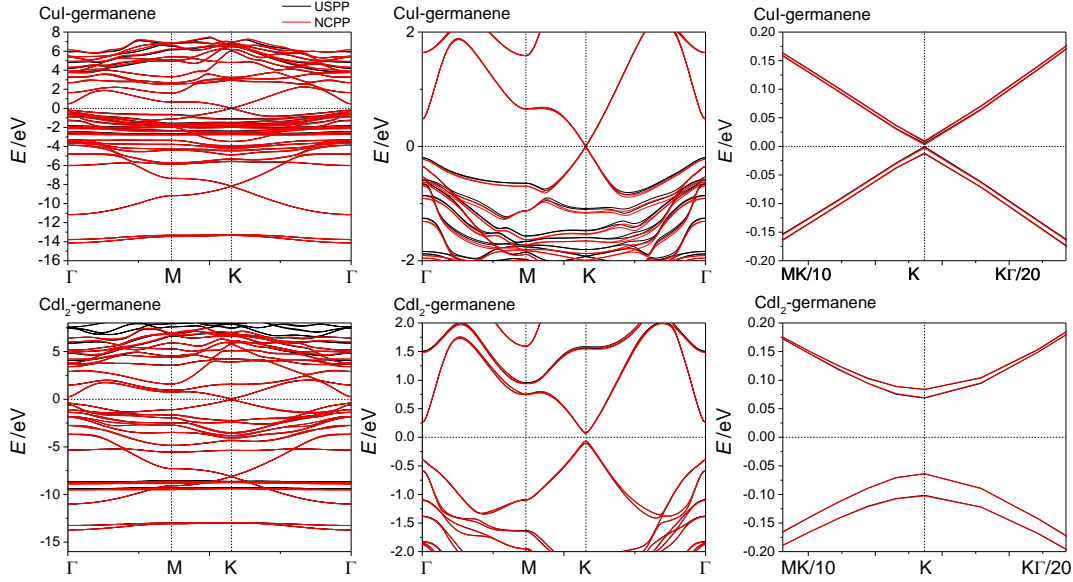
Figure 4-2: Comparison of band structures of supported germanene by using USPP and NCPP. Here germanene on CuI and CdI_2 are studied. In this work, NCPPs are used in the Z_2 invariant calculations.

To illustrate the research routine applied to each substrate candidate, let us take CdI_2, a typical substrate candidate for germanene, as an example. One type of bulk CdI_2 (Figure 4-3 (b) & (d), ICSD: 6066) has a hexagonal lattice with a lattice constant of 4.24 Å. The lattice constant is similar to that of the free standing germanene (4.02 Å, Figure 4-3 (a) & (c)), so we adopt a 1×1 stacking configuration (Figure 4-3 (e)) for the germanene-CdI_2 system. Such 1×1 configuration is applied to all other cases for the same reason. Monolayer substrate is chosen to reduce the overall computational cost and generally should yield similar results as the corresponding bulk substrate according to Chapter 3,[124] because all candidates have layered structures. In order to search for the most energetically favorable geometry, first a randomly stacked germanene-CdI_2 system is optimized at different lattice constants (Figure 4-5) to obtain the optimal cell size. Then the most stable stacking pattern of germanene on CdI_2 is investigated. Because there are 3 high symmetric points (marked as 0, 1 and 2 below the dashed lines in Figure 4-3 (e)) in one hexagonal cell and 2 different Ge atoms in germanene, there are $\binom{3}{2} = 6$ high symmetric stacking patterns

in total. In order to make a clearer notation, we abandoned the notations used Chapter 3 like ab-M-b. Instead, the 6 stacking patterns are labeled as $Ge^i Ge^j I^k Cd^l I^m$, where i, j, k, l, m = 0, 1, 2 denoting the high symmetric points. Other non-high-symmetric stacking patterns are found to be less preferable in Chapter 3 of similar systems and thus are ignored in this work.[124] The most stable stacking pattern is found to be $Ge^1 Ge^0 I^2 Cd^0 I^1$ (Figure 4-3 (e), Figure 4-6), which is characterized by an AB-like tip-to-valley configuration with the highest atoms ("tips") in bulked germanene and CdI_2 aligned to the hollow-centers ("valleys") in each other like a pair of gears. Such a tip-to-valley configuration result in a significantly smaller inter-layer distance between germanene and CdI_2 compared to the other tip-to-tip configurations (Figure 4-6), leading to a smaller total energy. Nevertheless, the interlayer distance is still as large as ~3.2 Å, suggesting the weak interaction between the two materials. Note that although there is another tip-to-valley configuration named $Ge^0 Ge^1 I^2 Cd^0 I^1$ which is only 0.01 eV over the most stable one, the two tip-to-valley configurations are related by a space inversion operation instead of any lateral translation of the germanene part and thus actually have a much higher energy barrier between them according to Chapter 3.[124]
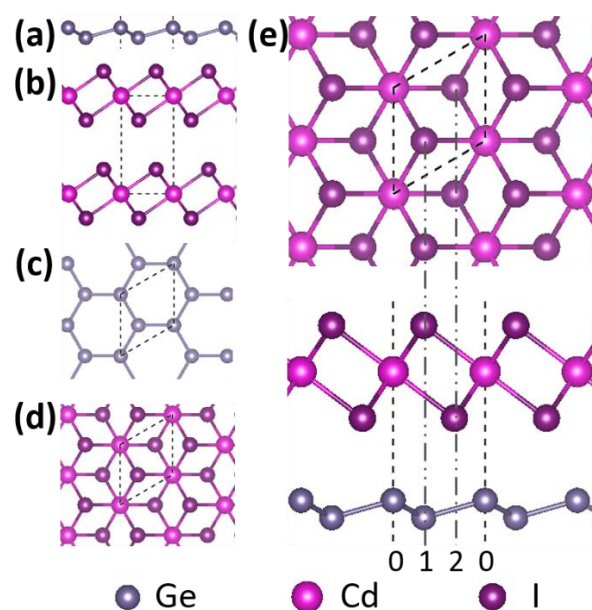
Figure 4-3: (a-d) Top- and side-view of free standing germanene and one kind of substrates, a type of bulk CdI_2 (ICSD ID: 6066). (e) Top- and side-view of the most preferable geometry of germanene on monolayer CdI_2. The numbers in the bottom ("0210") denotes the high symmetric points in the hexagonal cell.

The stability of the germanene-CdI$_2$ system is established by phonon calculations. Its phonon dispersion, shown in Figure 4-11(a), is all positive except for small (< 2 cm^{-1}) negative frequencies near the Γ point. The negative frequency is supposed to be a part of the out-of-plain acoustic (ZA) branch of germanene and can also be found in free-standing germanene.[17] Such minor negative frequency pocket can be eliminated,[134,135] for example by improving the optimization accuracy (grey lines in Figure 4-11 (a) by this group). As a result, we believe that it does not affect the stability of the system and do not further optimize the phonon calculations due to the lack of computational resource and significance.

4.3. Materials filtered out by data mining

The overall geometric data for the candidate substrates are listed in Table 4-2. Using the procedure described above, we filter out 8 2D materials from more than 185,000 entries in ICSD.
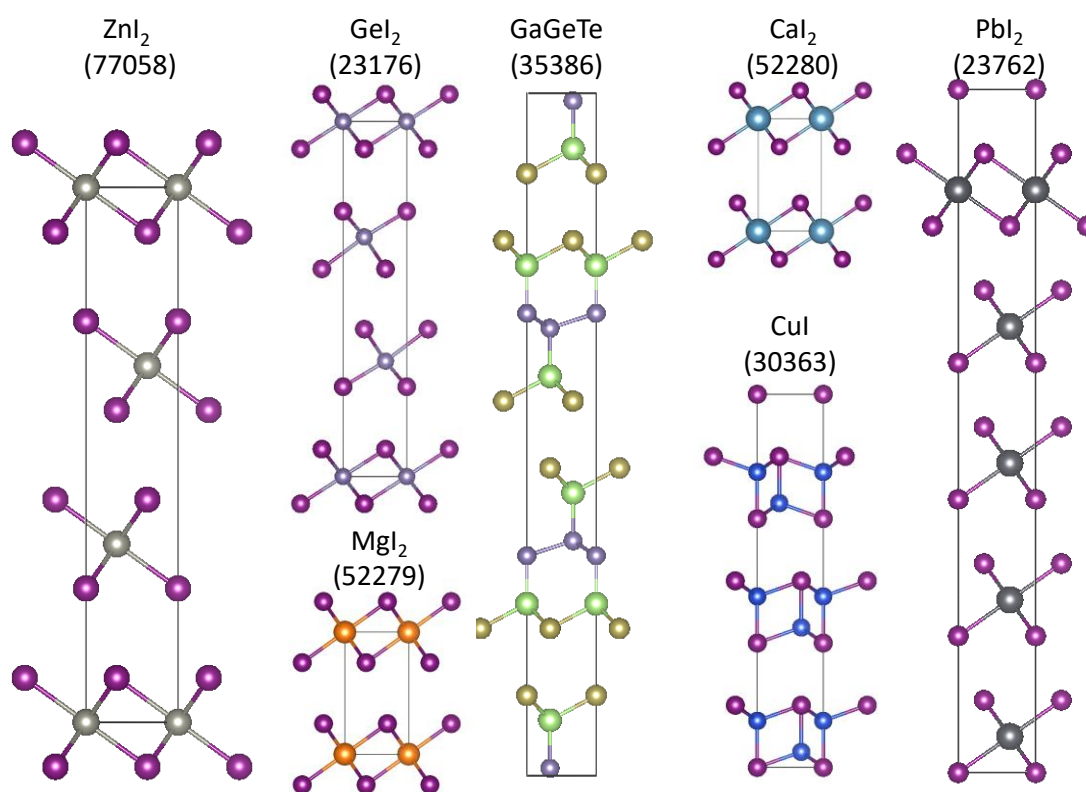
Figure 4-4: Bulk structure of suitable 2D substrates found in this work from ICSD. The ICSD id is written in the parenthesis.

Among them, we obtain 6 and 2 suitable substrate candidates for germanene and stanene, respectively, some of which are displayed in Figure 4-4. All of the substrates can be found in

experimental literature at room temperature and atmospheric pressure, and most of them are iodides. Some of them have been used as the substrate for vdW epitaxial growth before, for example CdI_2 and PbI_2.[136] Moreover, thin films of single crystal PbI_2 with a lateral scale over tens of micrometers have been successfully synthesized very recently,[137] which can serve as a planar substrate.

The optimization of lattice constant and stacking configuration is fully displayed in Figure 4-5 and Figure 4-6, respectively, and the optimized structural parameters are listed in Table 4-2. We have avoided variable-cell relaxation and use fixed-cell optimization with different lattice constants. Optimal lattice constants a are steadily obtained by this method as the minimum of the *E-a* curve, as shown in Figure 4-5. Similarly, the optimal high-symmetry stacking patterns are obtained by energy comparison, and they all have smaller interlayer distance z between germanene and the substrate compared to other stacking patterns, as shown in Figure 4-6, which will be explained below. In Table 4-2 one can find that the optimized lattice constants are almost between the bulk lattices of the substrates and those of the free-standing germanene (4.02 Å) and stanene (4.67 Å). The majority of the most preferable stacking patterns follows a similar pattern beginning with $A^1A^0X^2$, where A=Ge/Sn and X are the surface atoms of the substrate. The substrates that do not follow this rule are found to be unstable in their phonon dispersion. The $A^1A^0X^2$ stacking patterns, as described above, have tip-to-valley configurations with a much reduced interlayer distance compared to the other type of configurations. The buckling distance of germanene/stanene on substrates generally becomes smaller if the optimized system has larger lattice constant. For germanene on substrate, 1% lattice mismatch causes roughly 1.5% change in the buckling distance, similar to and slightly larger than the value of ~1.2% for free-standing germanene under 1% strain.[138] The vertical distance between germanene/stanene and substrates are almost all above 3 Å, and the binding energies between the layers are as small as 14.8 ~ 29.3 meV Å^{-2}, which can be treated as a sign of weak vdW interaction. In contrast, germanene-CuBr system has a small interlayer distance and large binding energy of 162.5 meV Å^{-2}, suggesting that the two materials are actually bonded.

Phonon calculations demonstrate that the presence of substrates only has minor effect on the phonon dispersion of germanene and stanene, if the system is stable. As shown in Figure 4-7, all of the stable phonon dispersions seem to be the combination of the substrate part and the germanene/stanene part. The acoustic and the Γ point out-of-plain optical (ZO) modes of the

phonon dispersions of the germanene/stanene part remain nearly the same as those of the free-standing cases. Nevertheless, the existence of substrate still lead to a small shift of the in-plain longitudinal and transverse optical (LO, TO) and K point ZO frequencies, the magnitude of which generally increases with lattice mismatch (Figure 4-8).[133] The phonon dispersions of germanene on $ZrTe_2$, $Y_2I_2Ga_2$ and CuBr (Figure 4-10) have large (>50 cm^{-1}) negative frequencies away from the Γ point and thus are marked as unstable.[133] However, it might be a result of the relatively lower accuracy in our choice for the parameters used in the automatic phonon calculations compared to manually fine-tuned calculations. Further calculation might be required to confirm their stability. Unless specified, we will exclude these unstable substrates in our discussion below. The infrared (IR) activity of germanene on suitable substrates are also calculated to assist the identification of these systems in experiment and can be used as fingerprints (Figure 4-9). Most systems have IR peaks around 70, 175 and 280 cm^{-1}.

Table 4-2: Structural properties, including the lattice constant of bulk substrate (a_{sub}) and system of monolayer substrate with germanene/stanene (a_{sys}), final lattice mismatch a_{mis} between the system and free standing germanene/stanene, stacking pattern, buckling Δ, vertical distance between substrate and germanene/stanene d_z, binding energy E_b, and phonon stability, of the systems of germanene/stanene supported by different 2D substrates. [a] Stanene substrates.

Name	ICSD ID	a_{sub} (Å)	a_{sys} (Å)	a_{mis} (%)	Stacking pattern	Δ (Å)	d_z (Å)	E_b (meV/Å^2)	Phonon Stability
ZnI_2	77058	4.25	4.03	0.2	$Ge^1Ge^0I^2Zn^0I^1$	0.695	3.185	15.7	Stable
CdI_2	6066	4.24	4.11	2.2	$Ge^1Ge^0I^2Cd^0I^1$	0.672	3.182	14.8	Stable
GeI_2	23176	4.13	4.05	0.7	$Ge^1Ge^0I^2Ge^1I^2$	0.694	3.133	16.0	Stable
GaGeTe	35386	4.048	4.06	1.0	$Ge^1Ge^0Te^2Ga^1Ge^1Ge^0Ga^0Te^2$	0.698	3.028	19.4	Stable
MgI_2	52279	4.15	4.08	1.5	$Ge^1Ge^0I^2Mg^0I^1$	0.684	3.310	15.5	Stable
CuI	30363	4.25	4.06	1.0	$Ge^1Ge^0I^2Cu^1Cu^2I^1$	0.691	3.152	16.3	Stable
CuBr	30091	4.096	4.02	0.0	$Ge^1Ge^0Cu^1Br^2$	0.821	1.716	162.5	Unstable
$ZrTe_2$	653213	3.952	3.99	-0.7	$Ge^1Ge^0Te^0Zr^2Te^1$	0.782	3.010	29.3	Unstable
$Y_2I_2Ga_2$	417149	4.179	4.12	2.5	$Ge^1Ge^0I^2Y^1Ga^0Ga^2Y^1I^0$	0.666	3.273	15.0	Unstable
PbI_2[a]	23762	4.56	4.61	-1.3	$Sn^1Sn^0I^2Pb^1I^0$	0.890	3.164	23.2	Stable
CaI_2[a]	52280	4.49	4.57	-2.1	$Sn^1Sn^0I^2Ca^1I^0$	0.906	3.349	22.5	Stable
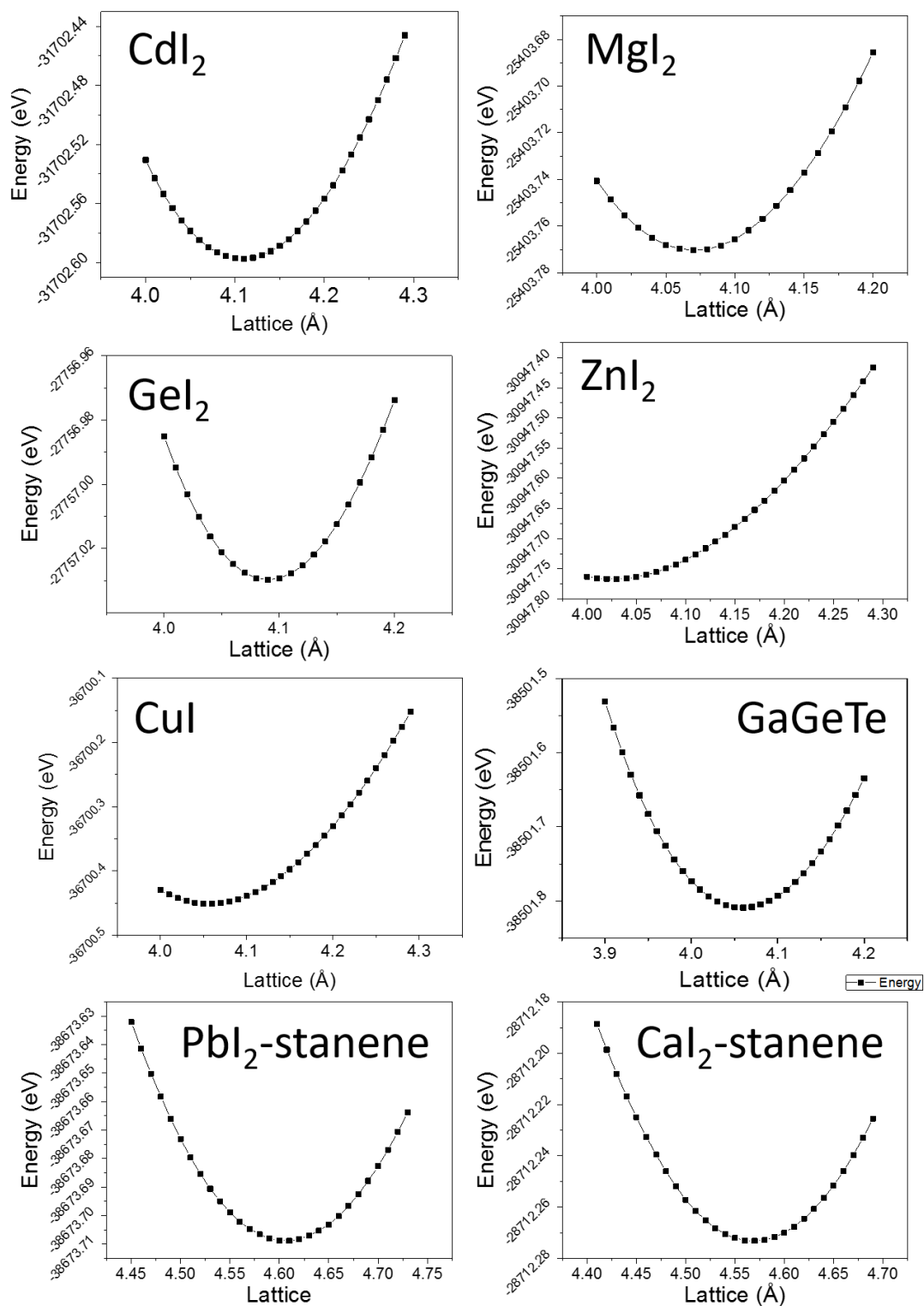
Figure 4-5: Total energy *E* vs. lattice constant *a* of the supported germanene/stanene on different substrates.
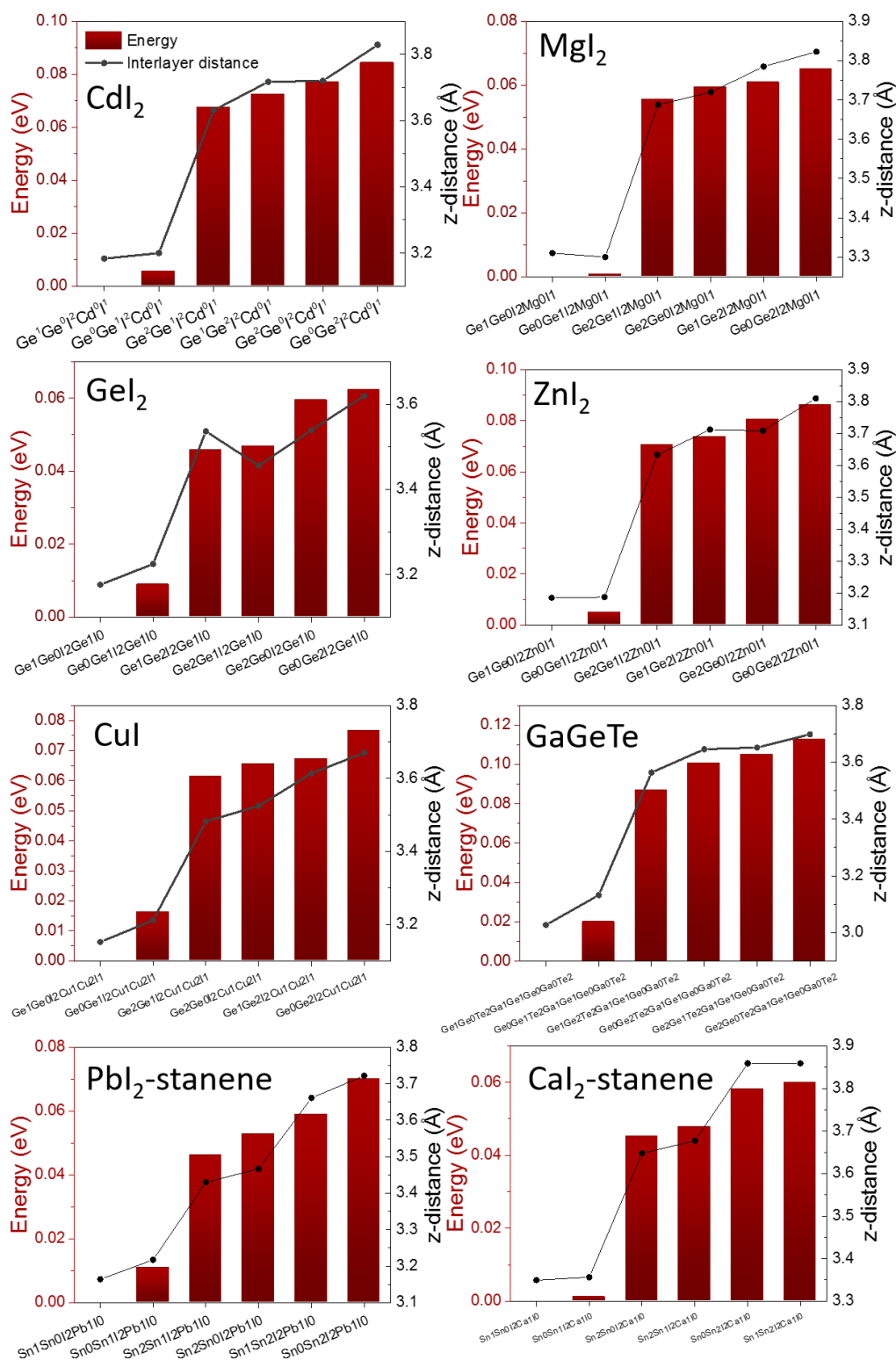
Figure 4-6: Total energy E and interlayer distance d_z of germanene/stanene on 2D substrates with different stacking patterns. The right scale is for columns (E) and the left scale is for line (d_z).
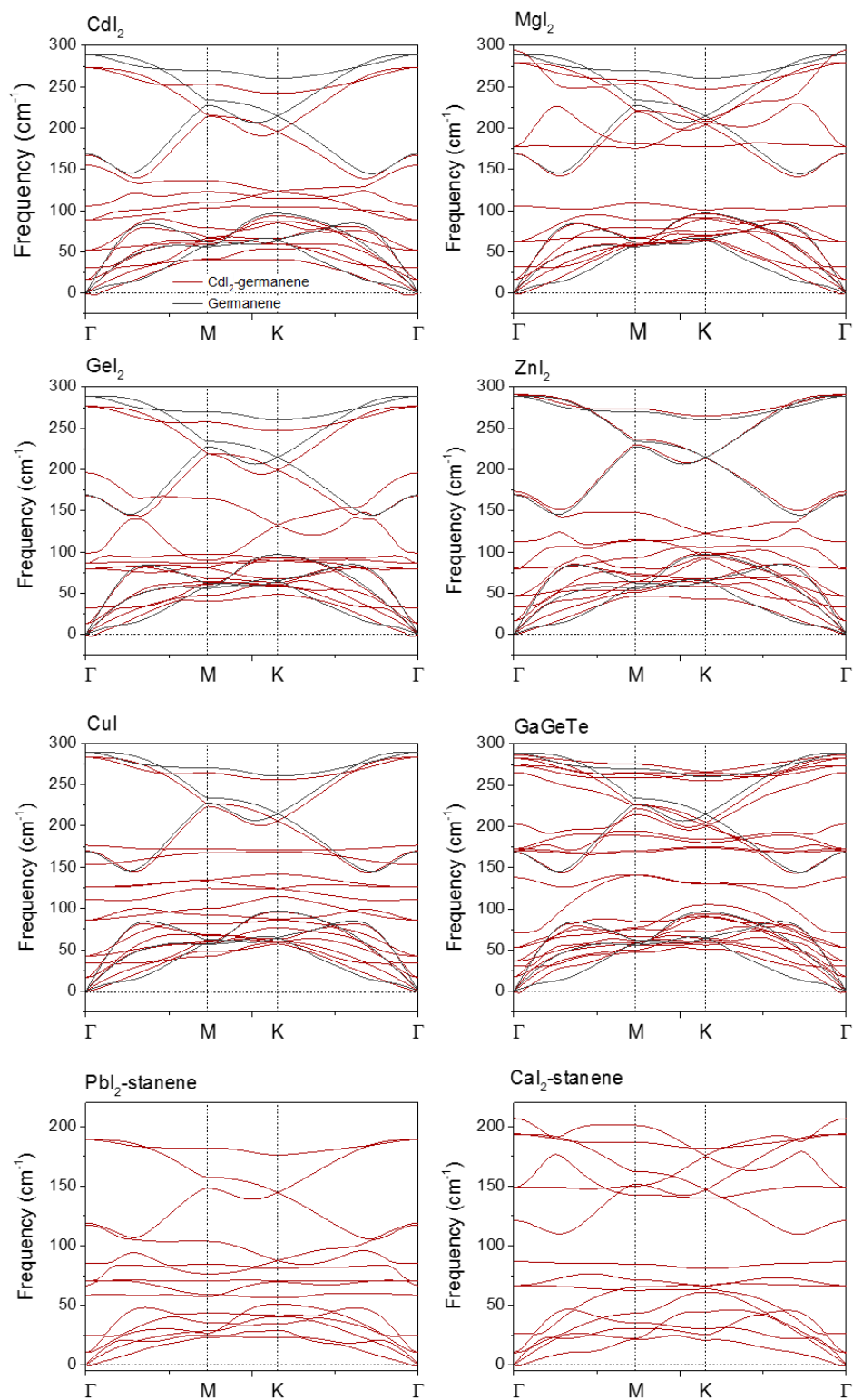
Figure 4-7: Stable phonon dispersions of germanene/stanene on 2D substrates. Light grey lines are phonon dispersion of free-standing germanene provided for comparison.
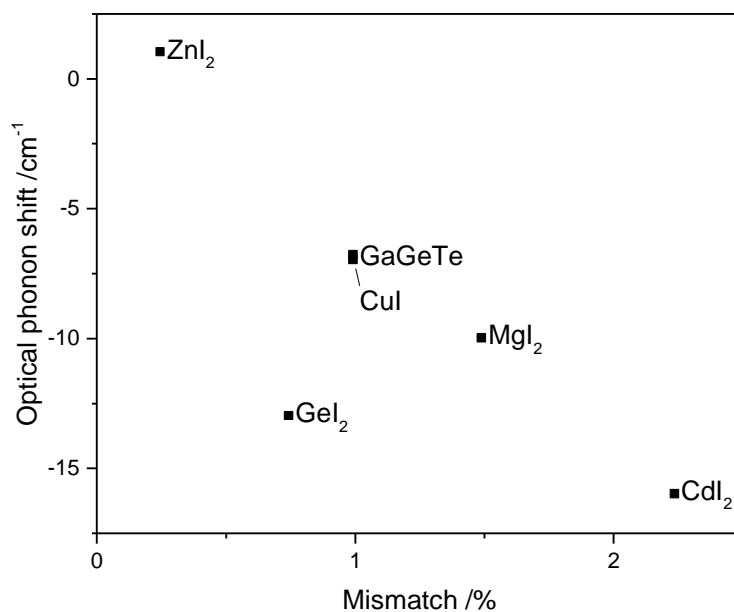
Figure 4-8: Relationship between the final lattice mismatch after optimization and the optical phonon shift of germanene at Γ point in the stable systems.
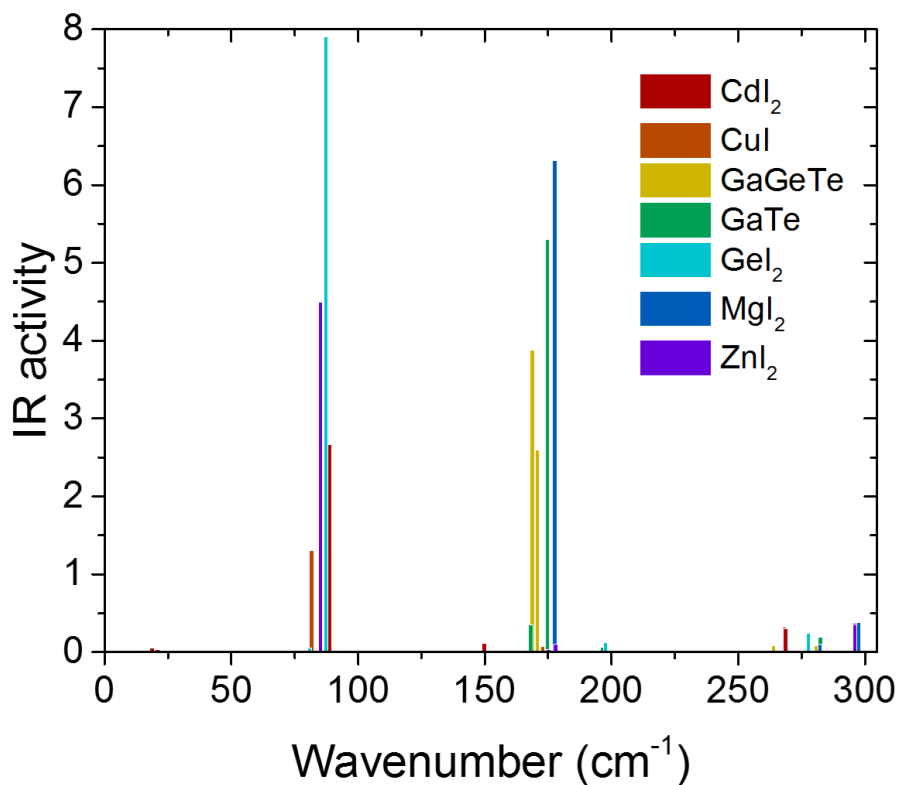
Figure 4-9: Infrared (IR) activity of germanene on suitable substrates. Most of the peaks are located around 70, 175 and 270 cm^{-1}.
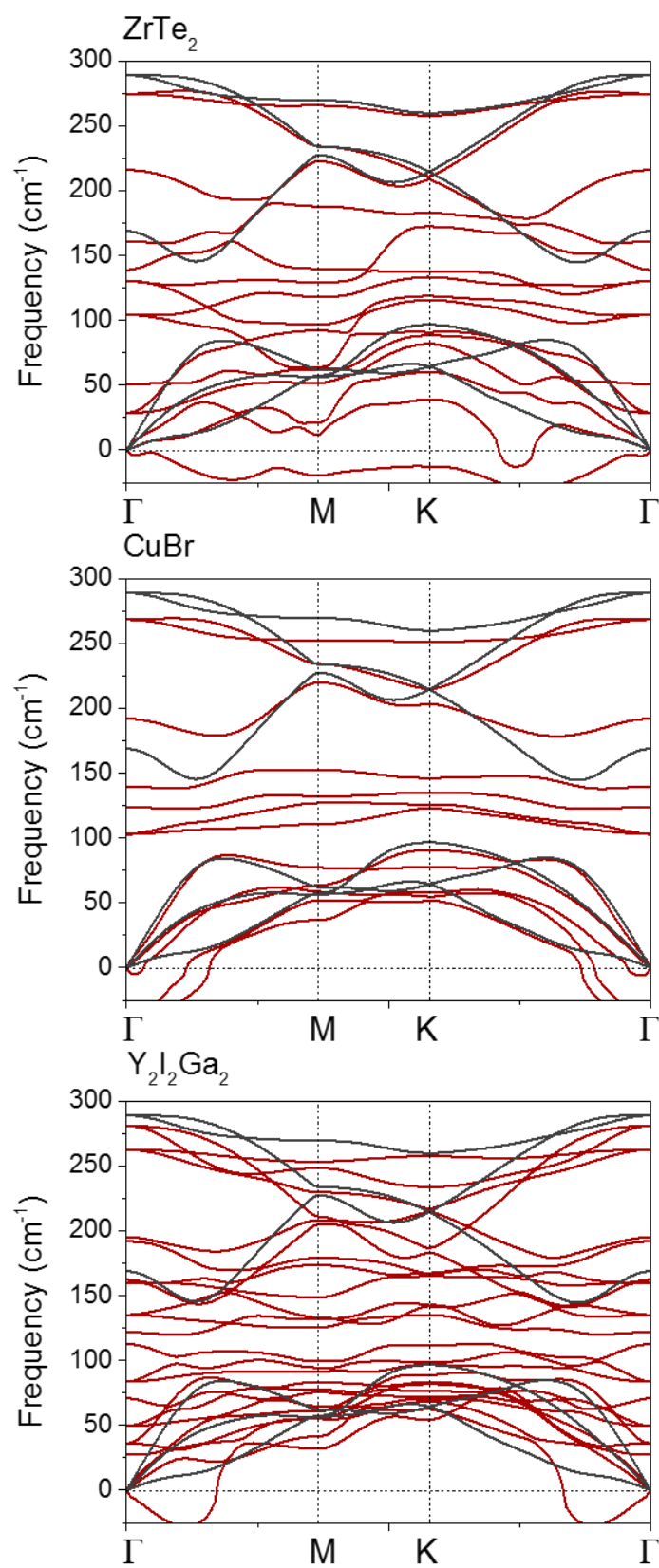
Figure 4-10: Unstable phonon dispersions of germanene on 2D substrates.

4.4. Electronic structure

After the structural investigation, the electronic properties, including the band structure, effective masses, charge transfer and Z_2 topological index, are examined for the candidate systems. Let us take the germanene-CdI$_2$ system as the example again. Figure 4-11 (b) clearly demonstrates a Dirac-cone-like band structure of germanene on CdI$_2$ with a band gap opened at the K point. Unlike the metallic germanene on MoS$_2$,[36] germanene on CdI$_2$ keeps semiconducting with a gap of 0.16 (0.13 with SOC) eV, which suggests the possibility of the fabrication of the first germanene field effect transistor (FET). The SOC split in the valence band (VB) and conduction
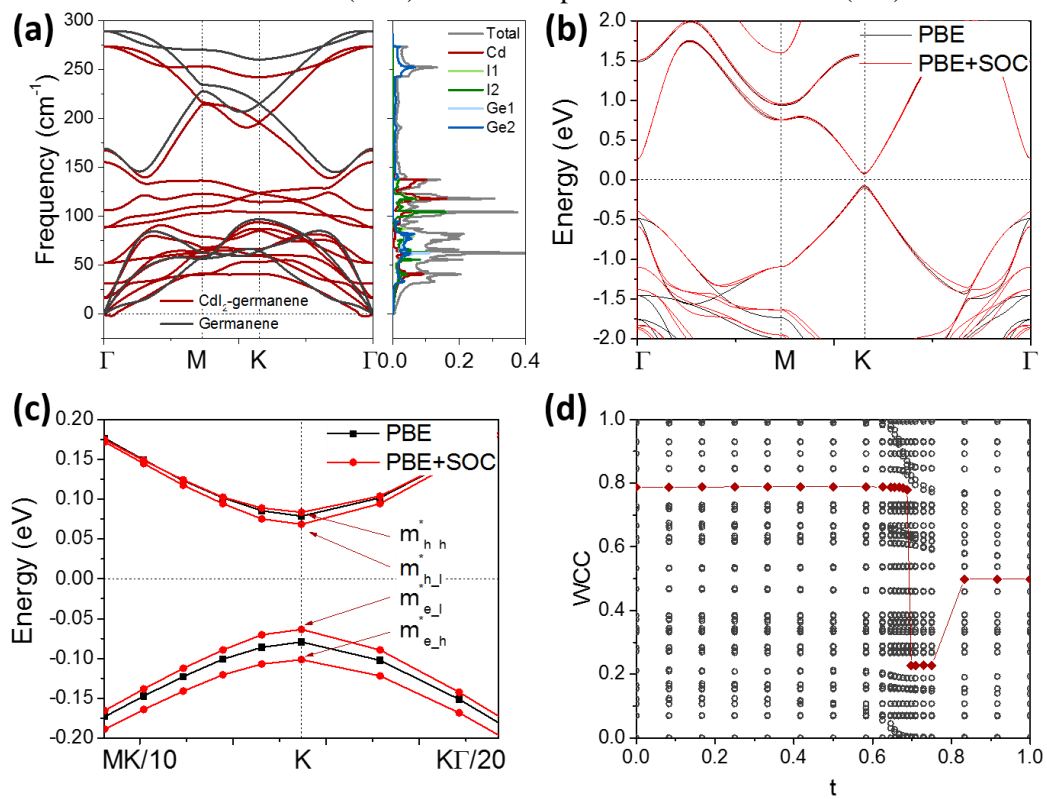
Figure 4-11: (a) Phonon dispersion (left) and partial density of states (PDOS, right) of the germanene-CdI$_2$ system. The phonon dispersion of free-standing germanene is also given as grey lines in the left figure. (b) Band structure of the germanene-CdI$_2$ system. (c) Band structure of the germanene-CdI$_2$ system in the adjacent of the K point in the reciprocal space. The SOC introduces splits in the valence band and conduction band, so there are four effective masses in germanene. (d) Evolution of Wannier charge center (WCC) over time t (k_y in 2D case) used for the calculation of the Z_2 invariant. Grey hollow circles are the positions of WCCs, and the red diamonds mark the center of largest WCC gap.

band (CB) of germanene introduces extra effective masses, namely the heavy hole/electron masses $m^*_{h\_h}/m^*_{e\_h}$ and light hole/electron masses $m^*_{h\_l}/m^*_{e\_l}$. While a band gap is opened, the calculated effective masses remain as small as 0.07 free electron mass m_e for light carriers. Since the intrinsic germanene is a topological insulator and has different phases under different external fields,[18] it is worthy of investigation on the topological state of germanene under the influence of substrate. The Z_2 topological index of germanene is calculated from the evolution of the Wannier charge centers (WCCs) shown in Figure 4-11(d).[88] In this case, the trajectory of the center of the largest WCC gap crosses over the WCC routes even times, so the Z_2 invariant is 0. Even though the interaction between CdI_2 and germanene is weak, it is large enough to be above the critical point and induce a phase transition in germanene from a topological insulator to a trivial one.

Table 4-3: Electronic parameters, including the band gap without SOC (E_g) and with SOC ($E_{g\text{-}SOC}$), average effective mass m^*_{avg}, charge transfer q from substrate to germanene, spin expectation value s in the z-direction for the VB-1 band, fitted paramters of the interaction model E_z, λ_{R1}, λ_{SO}, $\lambda_{SO\text{-}sub}$ and M, and the Z_2 invariant of the system. Note that stanene's "Z_2" on CaI_2 is unphysical due to its semimetallic nature in this case, but becomes physical when it becomes semiconducting by e.g. applying strain. [a]Stanene substrates

Name	Band gap (eV)		m^*_{avg} (m_e)		q (|e|)	s	E_z (V/nm)	λ_{R1} (meV)	λ_{SO} (meV)	$\lambda_{SO\text{-}sub}$ (meV)	M (meV)	Z_2
	E_g	$E_{g\text{-}SOC}$	Light	Heavy								
ZnI_2	0.185	0.157	0.080	0.107	-0.022	0.87	2.5	49.9	14.0	1.1	0.2	0
CdI_2	0.158	0.132	0.069	0.095	-0.023	0.89	2.2	40.7	13.3	0.4	0.6	0
GeI_2	0.101	0.085	0.052	0.060	-0.043	0.94	1.4	19.5	8.2	-4.7	-2.7	0
GaGeTe	0.100	0.078	0.041	0.062	-0.043	0.95	1.4	15.6	11.3	-1.6	-1.0	0
MgI_2	0.075	0.055	0.030	0.047	-0.031	0.96	1.1	11.0	10.3	-2.6	0.3	0
CuI	0.002	0.006	0.018	0.018	-0.058	0.53	0.1	5.2	6.9	-6.0	0.9	1
PbI_2[a]	0.069	0.020	0.021	0.101	-0.038	0.92	0.9	19.8	31.0	-5.9	7.1	0
CaI_2[a]	0.017	metal	-	-	-0.021	0.86	0.3	5.3	33.5	-3.3	2.9	"1"

In general, germanene and stanene preserve many of their free-standing electronic properties on these substrates. As demonstrated in Figure 4-12 (and Figure 4-15 for a clearer view at the Fermi level around K),[133] germanene and stanene still have their Dirac-cone-like band structures on most of the candidate substrates. Notably, they become semiconducting and keep neutral on CdI_2, MgI_2, GeI_2, ZnI_2, CuI and GaGeTe for germanene and PbI_2 for stanene, with a band gap E_g ranging from 0.002/0.006 to 0.185/0.157 eV for non-SOC/SOC cases, as listed in Table 4-3. As is known to all, the lower limit of the band gap in the channel materials of traditional FETs is around 0.4 eV. The maximum $E_{g\text{-SOC}}$ of 0.157 eV in this work is closer to such limit compared to 0.10 eV in Chapter 3 and can be enhanced by cooperation with other gap-opening techniques, such as vertical electric field and surface adsorption, for further tunability. [28,30,124] The reason of the gap-opening in germanene and stanene is the symmetry breaking effect induced by the substrates, and the gap size is related, but not simply proportional, to the interaction strength
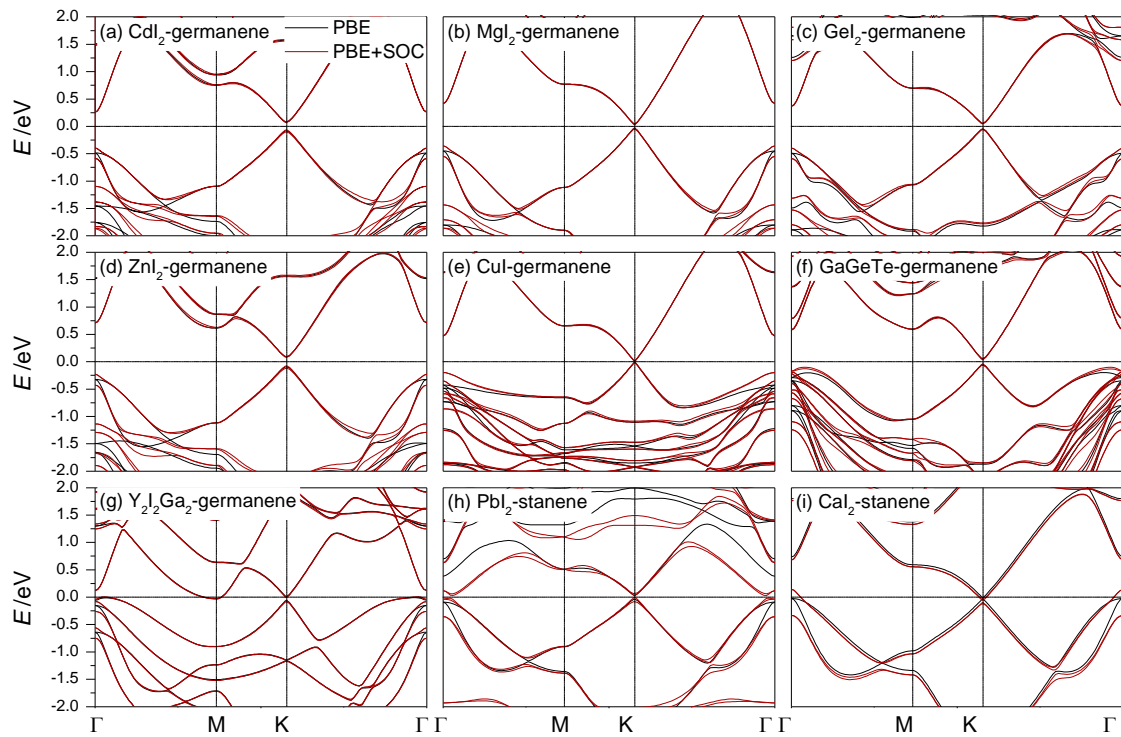
Figure 4-12: (a-g) Band structures of some germanene-substrate systems with Dirac-cone-like band structures: (a) CdI_2, (b) MgI_2, (c) GeI_2, (d) ZnI_2, (e) CuI, (f) GaGeTe and (g) $Y_2I_2Ga_2$. All systems are semiconducting except for $Y_2I_2G_2$. (h & i) Band structures of stanene-substrates systems with Dirac-cone-like band structures. Note that CaI_2-stanene system is semiconducting without SOC, but turns into metallic when SOC is employed.

between substrates and germanene/stanene. The corresponding tight-binding model will be discussed later to explain the phenomenon.

Although a band gap is opened, germanene/stanene still preserve small effective masses m^* of 0.018/0.018 ~ 0.080/0.107 m_e for light/heavy carriers, where m_e denotes the mass of free electron. Since the phonon dispersion of free-standing germanene and the supported one here are alike (Figure 4-7), we assume that the relaxation time τ in our case is similar as that of the free-standing case (τ = 5.3 ps). Then, the carrier mobility μ of germanene on our candidate substrates estimated by $\mu = e\tau/m^*$ can be 1~8 × 10^5 cm^2 V^{-1} s^{-1} for light carriers. In comparison, the theoretical intrinsic carrier mobility of free-standing graphene and silicene are ~3 and ~2 × 10^5 cm^2 V^{-1} s^{-1}, respectively, without a significant band gap.[33] Note that the maximum value can exceed the intrinsic μ of germanene, because germanene on CuI has even smaller band gap than free-standing germanene considering SOC. In this work, $E_{\text{g-SOC}}$ and m^* of germanene on substrates have a linear
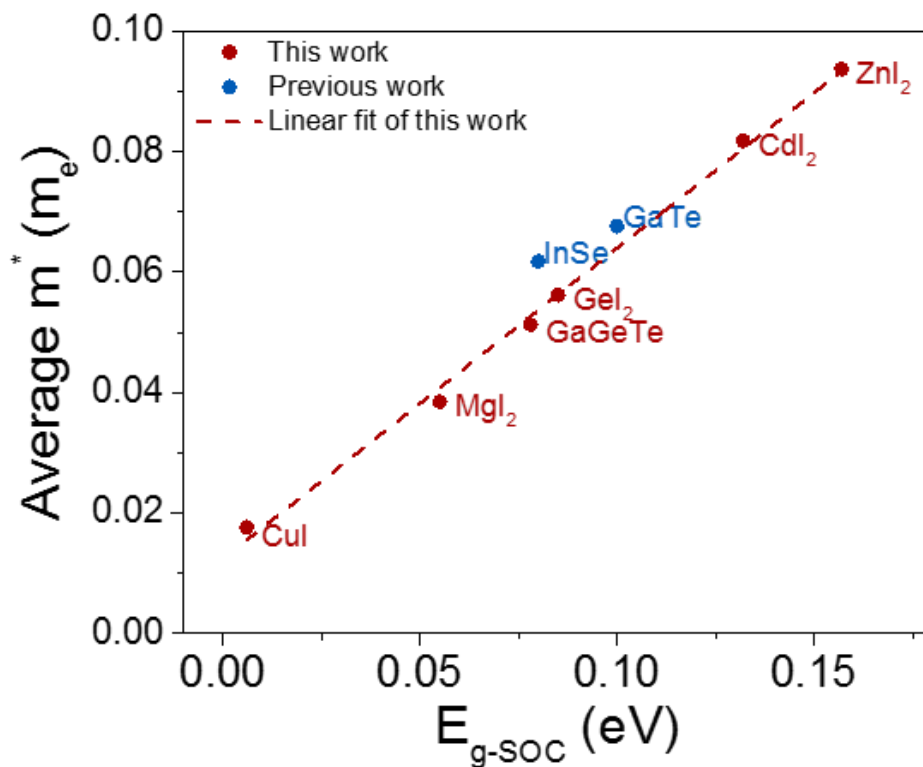
Figure 4-13: Relationship between the averaged effective mass m^*_{avg} and $E_{\text{g-SOC}}$ of germanene on different substrates. The dashed line is the linear fit of the data of this work. Some other substrates from our previous work (Light grey dots) are also shown for comparison.

relationship of $m^* \sim E_{\text{g-SOC}}/2$ (Figure 4-13), which is well known as the trade-off between the gap size and mobility. If such a trade-off rule is not violated at $E_{\text{g-SOC}} = 0.4$ eV, which is true under tight-biding model (Figure 4-14), germanene would still have a high carrier mobility over 4×10^4 cm^2 V^{-1} s^{-1}. As a comparison, the best carrier mobility reported in experiment of black phosphorus is in the order of 10^4 cm^2 V^{-1} s^{-1},[139] and that of MoS$_2$ is in the order of 10^3 cm^2 V^{-1} s^{-1}.[140] Impressively, germanene on CuI and stanene on CaI$_2$ have a non-trivial Z$_2$ topological index (see Figure 4-16 for WCC evolution diagrams). For stanene on CaI$_2$, although it is a semimetal (Figure 4-12(i)), two groups of bands are separated by an energy "gap" near the Fermi level in the whole reciprocal space, so a topological index for the lower group of bands still can be defined.[88] Although the Z$_2$ index seems to be "unphysical" here, one may apply strain on the stanene/CaI$_2$ system to turn it into a semiconductor and then Z$_2$ will become meaningful. On the rest of substrates, where germanene and stanene open a larger band gap, they transit to band insulators, even though the interaction with the substrate is as weak as the vdW interaction.
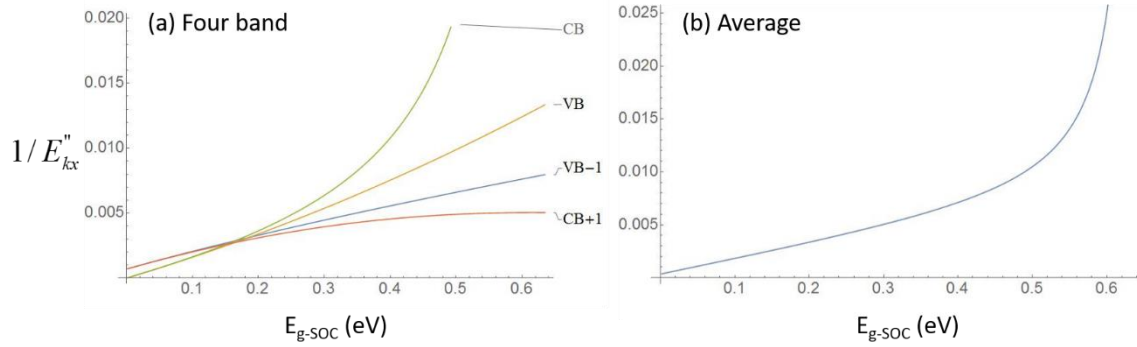
Figure 4-14: (a) Reciprocal for the second order derivative of the tight-binding eigenvalues at the K point of free-standing germanene along the k_x direction $1/E''_{kx} \equiv (\dfrac{\partial^2 E(k_x, k_y, E_z)}{\partial k_x^2})^{-1} |_{k_x=k_y=0}$ versus the SOC gap size $E_{\text{g-SOC}}$ of germanene under electric field. Here $M = \lambda_{\text{R2}} = 0$, $\lambda_{\text{R1}} = 0.17 E_z$ are used as parameters; (b) Average result of (a). Since $m^*_{K\Gamma} \propto 1/E''_{kx}$, these figures show that the average effective mass of germanene has an almost perfect linear trade-off against the band gap $E_{\text{g-SOC}}$ when $E_{\text{g-SOC}} < 0.4$ eV.
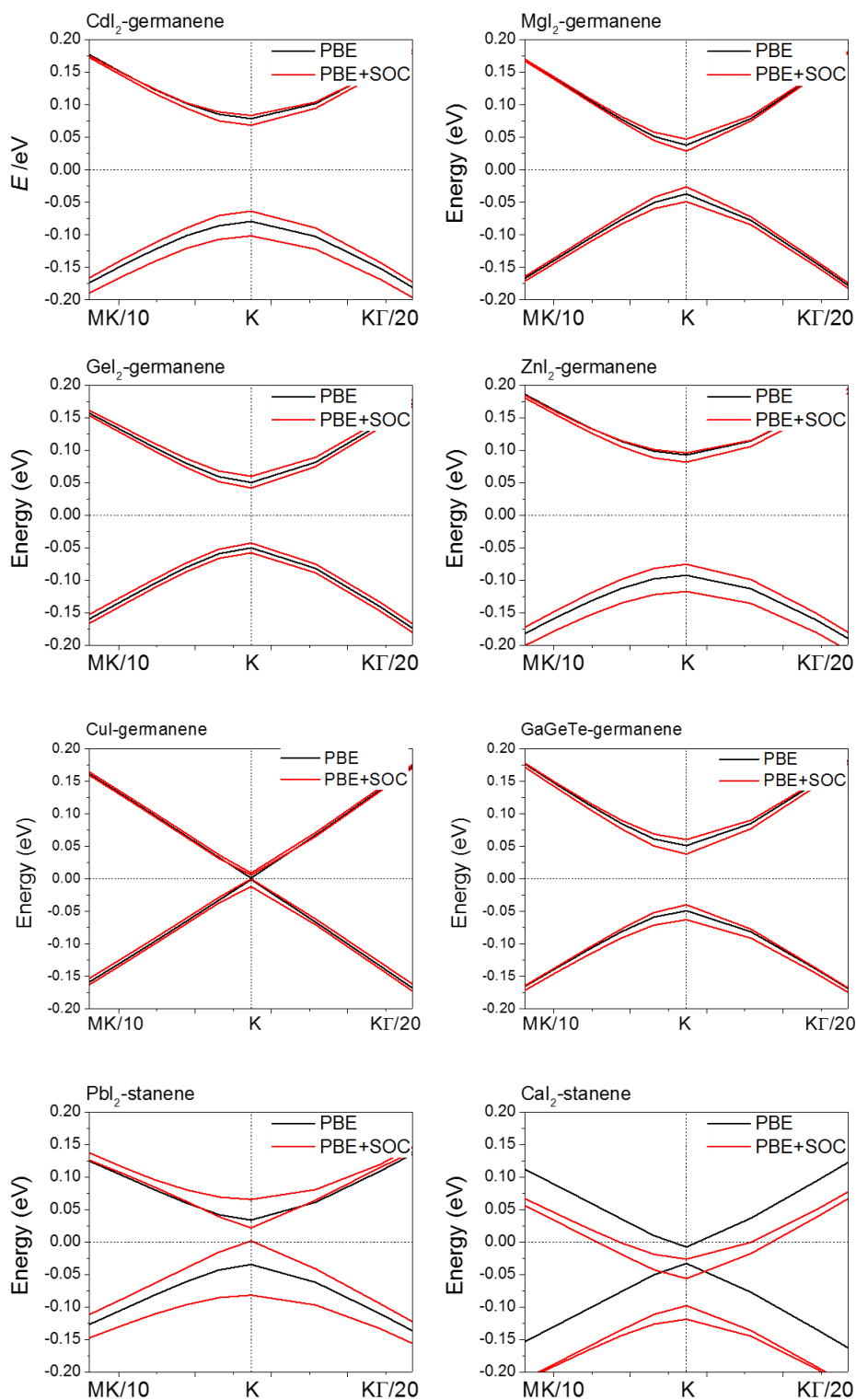
Figure 4-15: Band structure of germanene/stanene on suitable substrates in the vicinity of the K point in the reciprocal space.
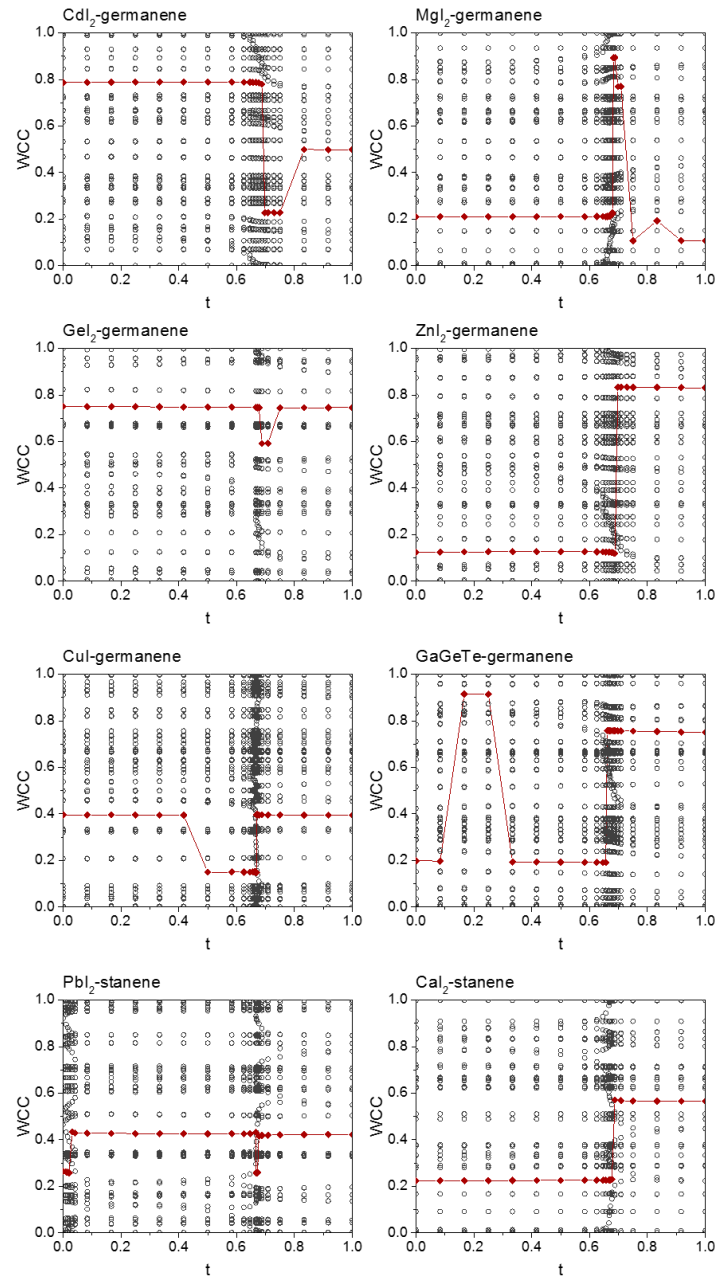
Figure 4-16: Wannier charge center (WCC) evolution of germanene and stanene on some suitable substrates. Grey circles are the fractional positions of WCCs along the x direction as the time parameter t evolves. In the 2D case, t is equivalent to k_y, i.e. the 2D band structure is considered as a 1D band structure along k_x evolve along the time t (k_y). The behavior of WCC evolution of Kramers pairs is different for $Z_2 = 0$ and 1 cases (Figure 2-5), but it is hard to distinguish in practice where there are many WCCs. Instead, the number of cross points between the WCC trajectories and the trajectory of the center of the largest WCC gap at time t (red dots and lines) is used for judging Z_2. The parity of the number of cross points is the same as Z_2.

4.5. Interaction between the substrate and germanene or stanene: pseudoelectric field

Here we will discuss the physical origin of the different properties of germanene/stanene on these substrates. The Hamiltonian in the vicinity of the K point of germanene/stanene under uniform external field can be written as:[18]

$$H_K(\vec{k}) = \hbar v_F \vec{k} \cdot \vec{\tau} - \Delta E_z \tau_z + \lambda_{SO} \tau_z \sigma_z + \tfrac{1}{2} \lambda_{R1}(\vec{\tau} \times \vec{\sigma})_z - a\lambda_{R2}\tau_z(\vec{k} \times \vec{\sigma})_z + M\sigma_z, \qquad (4\text{-}1)$$

where $\vec{k}$ is the relative reciprocal vector near K. $\vec{\sigma}$ and $\vec{\tau}$ are Pauli matrices representing the spin and the A-B sublattice pseudospin in germanene/stanene, respectively. v_f is the Fermi velocity. The second term is the staggered sublattice potential term, where Δ is half of the buckling of germanene/stanene and E_z is the vertical "pseudoelectric" field applied to germanene/stanene by the substrate. Pseudoelectric field has been reported to be generated by dynamic deformation in Dirac materials such as graphene and Cd_3As_2.[141,142] $\lambda_{SO} = \lambda_{SO-dirac} + \lambda_{SO-sub}$ corresponds to the sum of the intrinsic SOC term in the Dirac material (germanene/stanene) $\lambda_{SO-dirac}$ and the SOC term induced by the substrate λ_{SO-sub}. $\lambda_{R1} = \alpha E_z$ is the first Rashba SOC term induced by E_z. λ_{R2} is the second Rashba SOC term associated with the next-nearest neighbor hopping. M is the "pseudomagnetic" field included to better describe the symmetry-breaking effect other than "pseudoelectric" term.[37] This term is added because it is known that strain will induce pseudomagnetic field in graphene,[143] which might apply in germanene/stanene as well. At the K point, $\vec{k} = 0$ and the λ_{R2} term vanishes, so the eigenvalues become very simple:

$$\begin{aligned} \varepsilon_{1,2} &= \lambda_{SO} \pm (\Delta E_z - M) \\ \varepsilon_{3,4} &= -\lambda_{SO} \pm \sqrt{(\Delta E_z + M)^2 + \lambda_{R1}^2} \end{aligned} \qquad (4\text{-}2)$$

This is very similar to the eigenvalues given in Ref. [37], except that the sign before M is

opposite in our equations. The corresponding eigenvectors in the $\{\Psi_{A\uparrow}, \Psi_{B\uparrow}, \Psi_{A\downarrow}, \Psi_{B\downarrow}\}$ space are

$(0, 0, 0, 1)$, $(1, 0, 0, 0)$, $(0, -i(\sqrt{\beta^2+1}+\beta), 1, 0)$ and $(0, i(\sqrt{\beta^2+1}-\beta), 1, 0)$, where $\beta =$

$(\Delta \cdot E_z + M)/\lambda_{R1}$. We have to note that there are four parameters for fitting, namely E_z, M, λ_{SO} and

λ_{R1}. However, there are actually only three known values, specifically band gap with SOC $E_{g\text{-SOC}}$,

valence band split Δ_{VB} and conduction band split Δ_{CB}. Moreover, the definition of $E_{g\text{-SOC}}$, Δ_{VB} and

Δ_{CB} varies according to the strength of E_z and M, since the order of $\varepsilon_{1,2,3,4}$ is uncertain. If λ_{R1}

is ignored, germanene/stanene will close the band gap at a critical electric field E_c and undergo a

phase transition from TI to band insulator if E_z continues to increase. If we do not ignore $\lambda_{R1} =$

αE_z and let $M = 0$, there will be two critical electric fields, namely $E_c = \dfrac{2\lambda_{SO}}{\sqrt{\Delta^2 + \alpha^2} + \Delta}$,

corresponding to the flip between ε_2 and ε_3, and $E_c^{'} = \dfrac{2\lambda_{SO}}{\sqrt{\Delta^2 + \alpha^2} - \Delta}$, corresponding to the flip

between ε_1 and ε_3.

To fit all parameters, one can use the expectation value of spin in the z-direction $s = <\sigma_z>$ of

the lowest band. With the eigenvector given above, the relationship between s and β can be

derived as $\beta = s/\sqrt{1-s^2}$, providing the forth equation for the parameter fitting. All of the four

parameters can be given as follows:

$$
\begin{pmatrix} \lambda_{SO} \\ |\lambda_{R1}| \\ E_z \\ M \end{pmatrix} = \begin{pmatrix} \overset{E_z < E_c}{\frac{2E_{g\text{-SOC}} + \Delta_{VB} + \Delta_{CB}}{4}} \\ \frac{\Delta_{VB}}{2}\sqrt{1-s^2} \\ \frac{\Delta_{CB} + s\Delta_{VB}}{4\Delta} \\ \frac{-\Delta_{CB} + s\Delta_{VB}}{4} \end{pmatrix} \text{ or } \begin{pmatrix} \overset{E_c < E_z < E_c^{'}}{\frac{\Delta_{VB} + \Delta_{CB}}{4}} \\ \frac{E_{g\text{-SOC}} + \Delta_{VB}}{2}\sqrt{1-s^2} \\ \frac{(1+s)E_{g\text{-SOC}} + \Delta_{CB} + s\Delta_{VB}}{4\Delta} \\ \frac{(s-1)E_{g\text{-SOC}} - \Delta_{CB} + s\Delta_{VB}}{4} \end{pmatrix} \text{ or } \begin{pmatrix} \overset{E_z > E_c^{'}}{\frac{\Delta_{VB} - \Delta_{CB}}{4}} \\ \frac{E_{g\text{-SOC}} + \Delta_{VB} + \Delta_{CB}}{2}\sqrt{1-s^2} \\ \frac{(1+s)E_{g\text{-SOC}} + s\Delta_{CB} + s\Delta_{VB}}{4\Delta} \\ \frac{(s-1)E_{g\text{-SOC}} + s\Delta_{CB} + s\Delta_{VB}}{4} \end{pmatrix} \quad (4\text{-}3)
$$

In addition, the Z_2 invariant can be used to determine whether $E_c < E_z$ or not, since germanene

will become trivial band insulator when $E_c < E_z$.[18] We estimate E_c' to be above 6.5 V nm^{-1} for

germanene using our fit results below and the values of Δ and λ_{SO} of free standing germanene. Since this field strength is not easy to achieve in practice, we assume that all effective E_z are weaker than E_c' in this work. We find that all fit parameters are reasonable under this assumption. The fitted parameters for supported germanene are presented in Table 4-3. Several interesting relationships can be found between them. First, λ_{R1} should be proportional to E_z in theory for free standing graphene and germanene,[144–146] which is found to be true also for supported germanene under a pseudoelectric field E_z induced by the substrate in our cases, as shown in Figure 4-17. The fitted α in $\lambda_{R1} = \alpha E_z$ is around 0.17 Å with a Pearson's product-moment correlation coefficient
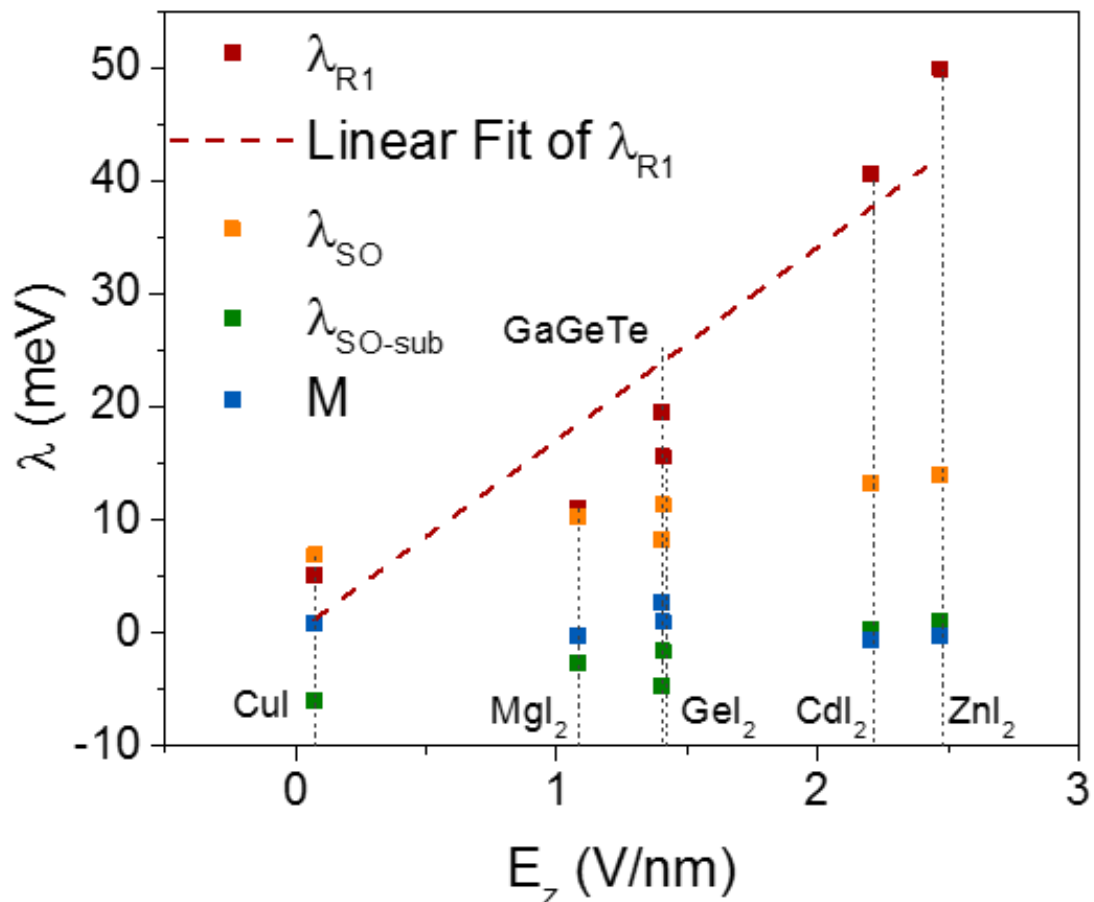
Figure 4-17: Relationship between E_z and the fitted λ_{SO}, $\lambda_{SO\text{-}sub}$, λ_{R1}, and M. Red dashed line is the linear fit between E_z and λ_{R1}.

r above 0.97. The *α* of germanene is above 2 orders of magnitude larger than $\alpha \sim 6 \times 10^{-4}$ Å in silicene,[18] partly due to the larger intrinsic λ_{SO} and Δ in germanene. The inclusion of *α* causes a 5% change in the value of E_c in germanene. Furthermore, if *α* becomes larger and gets closer to the value of Δ, which is possible to happen in stanene considering its even larger λ_{SO}, the correction of λ_{R1} on E_c would be significant, and the second critical electric field E_c' might be observable in practice.

Second, the charge transfer between germanene and the substrate, as well as the charge transfer between the two Ge atoms in germanene, is also proportional to Ez, as shown in Figure 4-18. It can be understood in two ways: either the vertical electric field Ez drives the electrons to redistribute from substrate to germanene and inside germanene, or E_z is actually a result of such
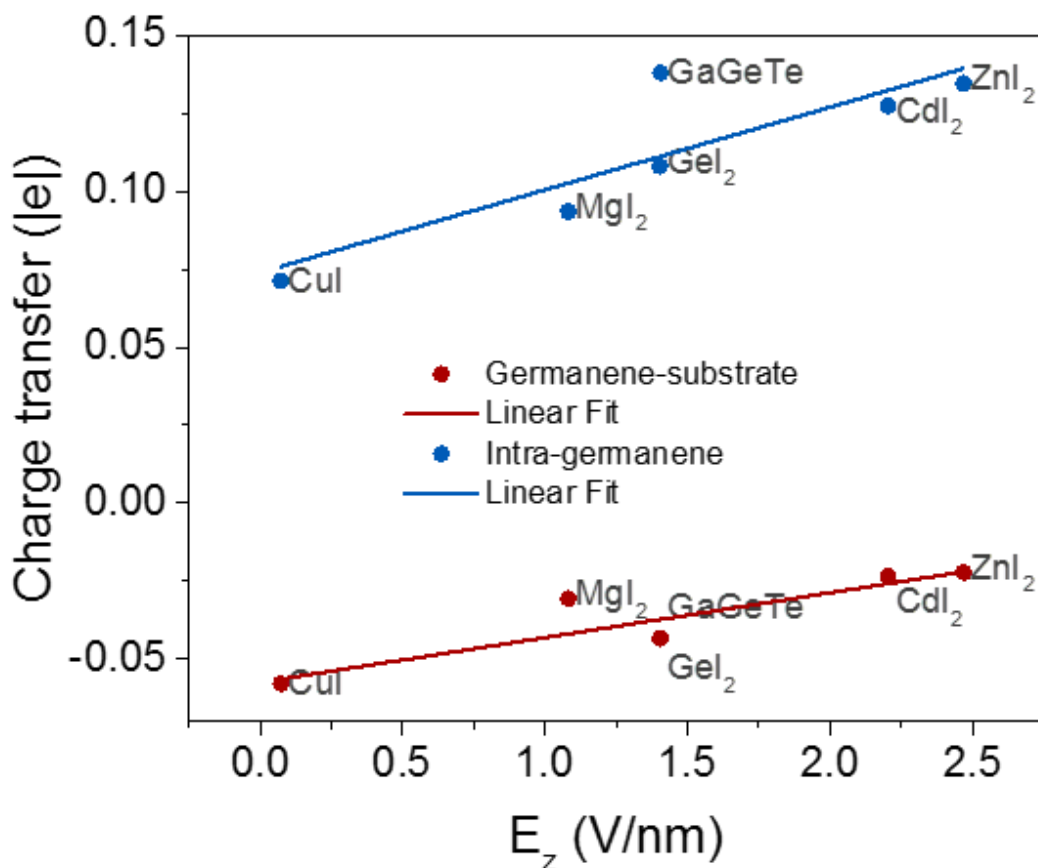
Figure 4-18: Charge transfer *q* between germanene and substrate (red) and Ge atoms inside germanene (blue) as a function of E_g, the band gap without SOC. Solid lines are corresponding linear fits.

charge redistribution. In any case, E_z should be linear to the charge transfer, which is confirmed by the good linear fitting displayed in Figure 4-18 with a Pearson's r above 0.86.

Finally, the perfect trade-off between $E_{\text{g-SOC}}$ and the average m^* shown in Figure 4-13 can also be explained by this model. Using the fermi velocity of free-standing germanene $v_f = 8.8 \times 10^5$ m s^{-1},[147] we calculate the reciprocal for the second order derivative of the bands at the K point

$$1/E_{kx}^{''} \equiv (\partial^2 E(k_x, k_y, E_z)/\partial k_x^2)^{-1}\,|_{k_x=k_y=0}$$ under the assumption of $M = \lambda_{R2} = 0$ and $\lambda_{R1} =$

$0.17 E_z$ (Figure 4-14).[133] Since $m_{K\Gamma}^* \propto 1/E_{kx}^{''}$, Figure 4-14 can also demonstrate the relationship

between $m_{K\Gamma}^*$ and $E_{\text{g-SOC}}$.[133] Although the individual effective masses of the four bands does not have very good linear dependency on $E_{\text{g-SOC}}$, the average effective mass of the four bands is almost perfectly proportional to $E_{\text{g-SOC}}$ when $E_{\text{g-SOC}} < 0.4$ eV. Note that germanene on all suitable substrates in this work satisfy the condition. All of the correlations found above can be viewed as a cross-validation for the correctness of the model and support the opinion that the different behaviors of germanene on substrates are the result of the external fields, mainly electric field, applied by the substrate.

4.5.1. Additional discussions

In this work we have focused on the 1x1 stacking mode for germanene on substrates. There may be two concerns about 1x1 stacking configuration. First germanene is possible to take a rotated configuration on the substrate with less strain. For example, germanene on MoS_2 can have a 27.8° rotated configuration with 0.7% strain proposed in theory;[37] Nevertheless, we have to note that even if such unit cell is made for germanene on other substrates with very small mismatch below 1%, it is probably still not realistic. For example in experiment, germanene on MoS_2 takes the non-rotated 5x5 supercell on 6x6 MoS_2 instead of the configuration proposed in theory with less strain.[36] Specifically, germanene on MoS_2 (a~3.18 Å) has a lattice constant of ~ 3.8 Å,[36] which is 5% smaller than the value of free standing germanene predicted in theory (~ 4.06 Å). It is probably a sign that germanene is trying to fit the lattice constant of MoS_2 due to their interaction. The substrates investigated in this work have small lattice mismatch (<6%) with germanene or stanene, so it is possible for them to fit to each other with the same lattice constant. We also have develop a program to search for the best-fit rotated supercell (under a certain tolerance) for germanene/stanene on an arbitrary substrate. By using it, we get the best-fit

supercell for germanene on CuI, which is $\sqrt{21} \times \sqrt{21}R72.656°$ for germanene and $\sqrt{19} \times \sqrt{19}$ for CuI with a lattice mismatch of about 0.4% (Figure 4-19). The average interlayer distance and buckling are 3.43 Å and 0.71 Å, respectively, slightly enlarged from 3.15 Å and 0.69 Å in the 1x1 case. We can see that CuI still can preserve the structure of germanene and serve as good substrate with the rotated configuration.
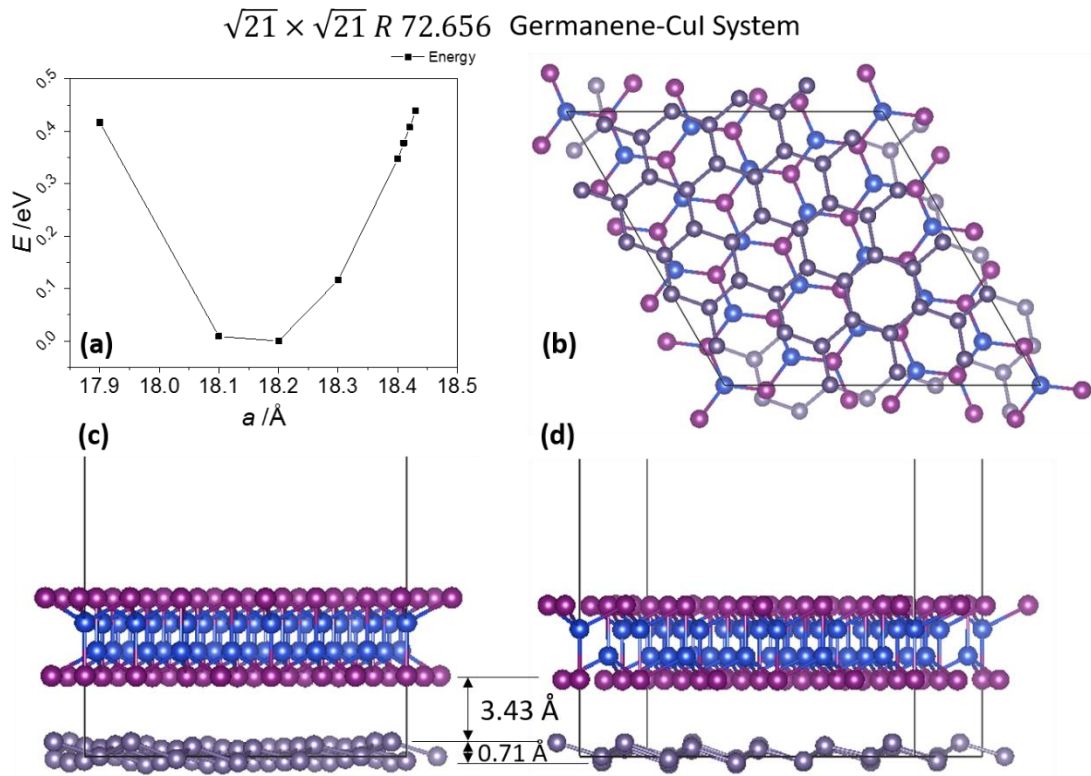
Figure 4-19: Rotated stacking of $\sqrt{21} \times \sqrt{21}R72.656$ germanene on $\sqrt{19} \times \sqrt{19}$ CuI with a lattice mismatch of about 0.4%. (a) Lattice constant a vs. total energy E in fixed-cell optimizations. The lowest energy is set to 0. (b-d) Structures of the optimized geometry: (b) top view; (c) side view along supercell axis; (d) side view along germanene's own axis.

Second, the 1x1 stacking itself is a constraint that might stabilize the structures that may be unstable otherwise. We have test a 5x5 supercell of the 1x1 stacking configuration and did not find any significant change in the geometry, interlayer distance and buckling. To further validate the stability of the structure at finite temperature, we have performed molecular dynamics (MD) simulation for 3x3 germanene-CuI supercell of the 1x1 stacking configuration at 400 K and 800 K, respectively. As shown in Figure 4-20, the hexagonal ring of germanene can be almost preserved at 400 K, but will be significantly distorted at 800 K. On the other hand, the z

coordinates of Ge atoms can no longer preserve the free-standing pattern both at 400 and 800 K. The MD results show that germanene can be stable on CuI at room temperature, but it is better to measure it at low temperature for a structure closer to the free-standing case. The above MD results are similar as germanene on GaTe discussed in Chapter 3.

Note that the PBE functional usually underestimate the bandgap size, which can be improved
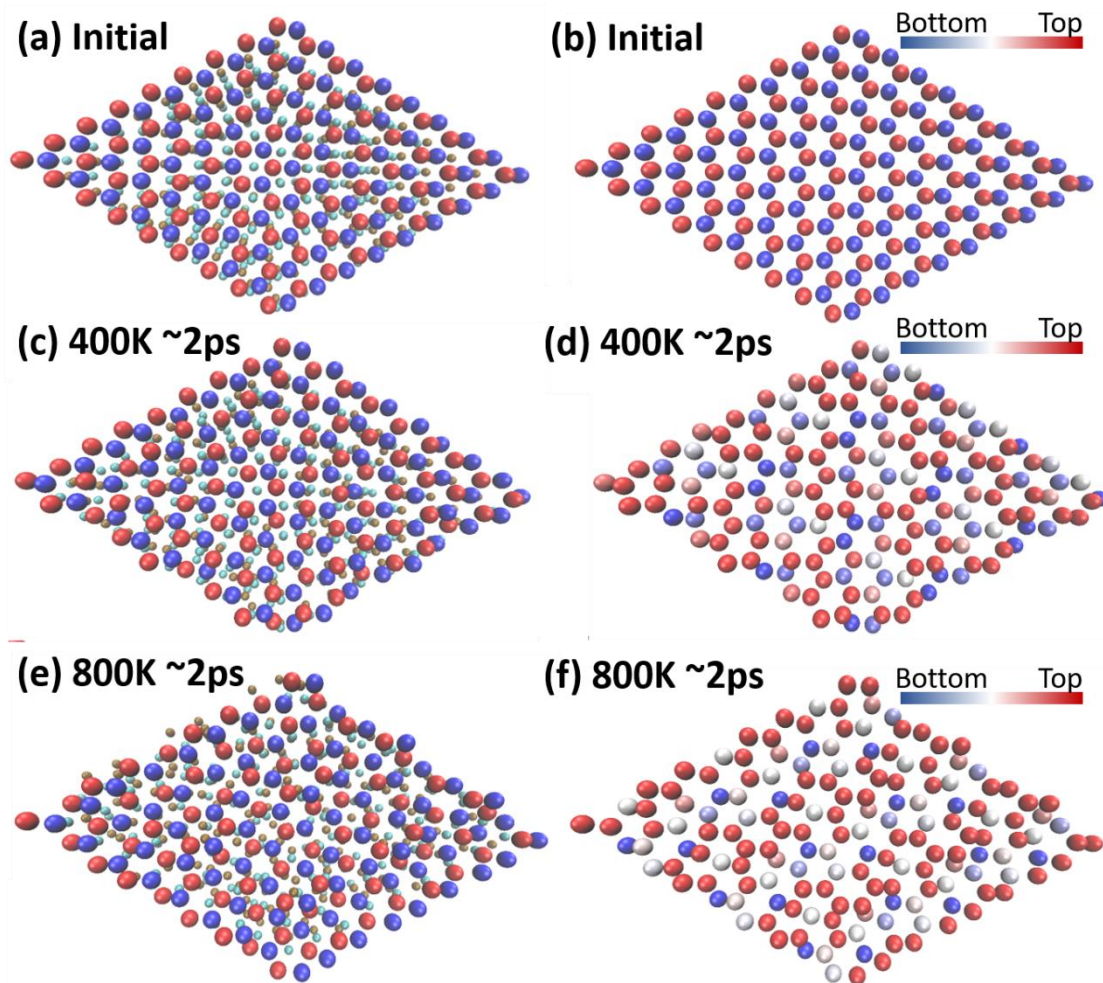
Figure 4-20: Molecular dynamics simulation of germanene-CuI system. The time scale is ~2 ps, consisting of around 2000 steps. Note that the simulated cell is of 3x3 size, while the structure displayed here is 9x9 for a clearer view. (a, b) initial structure; (c, d) final structure after 2ps at 400K; (e, f) final structure after 2ps at 800 K. Green and brown balls in the left column, (a, c, e), are I and Cu, respectively. Red and blue balls in the left column are top- and bottom-Ge in germanene, respectively, defined by the initial structure. In the right column (b, d, f), the substrate is not shown and the Ge atoms are re-colored by their current z coordinates.

by using hybrid functionals like HSE06 instead.[70,71,73] However, we do not expect that such replacement would affect the above general conclusion for suitable substrates, because we previously found in Chapter 3 that using HSE06 only enlarges the gap size by ~30% compared to the PBE functional without SOC and does not change the shape of the Dirac-cone for germanene on suitable substrates.[124] Moreover, the SOC effect will almost cancel such an increase of band gap in germanene,[124] so the HSE06+SOC bandgap might be similar to the PBE bandgap without SOC in germanene. For example, the bandgaps of germanene on GaTe and InSe are 0.12/0.10/0.16 eV and 0.11/0.08/0.14 eV, respectively, for PBE/PBE+SOC/HSE06 calculations.[124] Furthermore, HSE06 calculation of germanene on CuI, which is chosen due to its non-trivial Z_2 predicted with PBE functional, is performed as a test with a k-grid of 3x3x1 and the same q-grid. The band gap predicted by HSE06 at the K point is 10 meV, similar to the value of PBE+SOC (6 meV). Since the use of the HSE06 will not have significant impact on our conclusions about the selection of suitable substrates, we decide to leave it for future research, considering the expensive computation cost of the hybrid functional. Applying many-body GW correction[148] may give similar or better band gap, but we cannot afford the heavy computational cost, so we have to leave it for future research as well.
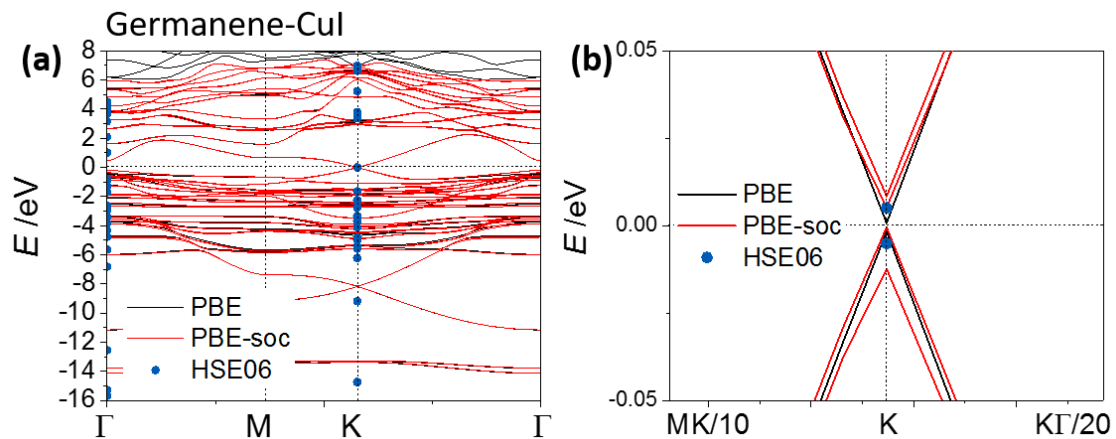
Figure 4-21: (a) Band structure of the germanene-CuI system using PBE, PBE with SOC, and HSE06 functionals. (b) Zoomed band structure of the same system around the K point in the reciprocal space.

In addition to be the substrate guide for experimentalists, our research might lead to at least two types of future study. First, one can make a vertical heterojunction, i.e. sandwiched germanene/stanene by different types of substrates, to tune their electronic properties and protect

them from ambient environment. The superimposition of the effect of the two capping layers may either cancel or enhance each other. If germanene is sandwiched between two substrates similar to ZnI_2 that have a E_z ~ 2.5 V nm^{-1} with an enhanced effect, it is possible to double the band gap in germanene to ~ 0.4 eV to make it suitable for FET application. In contrast, two substrates with a canceled effect may lead to small or zero electric field, resulting in a non-trivial Z_2 invariant in germanene. Second, it is interesting to put germanene on the junction of two types of the substrates, say CuI and ZnI_2, to see whether it will have the topological edge state in germanene/stanene at the boundary of two substrates (or "topological domain wall"[20]). Note that in such a system, germanene can be intact without any geometric boundary.

4.6. Conclusions

We have found several suitable 2D substrate candidates, including some of the CdI_2-type materials, CuI, and GaGeTe, for germanene and stanene by using the combination of density functional theory and materials informatics. We have succeeded in finding more candidates than previous manual searches in Chapter 3, and some of them show better properties, like larger band gaps, than those previously found. The suitable substrates can preserve the quasi-free-standing geometry and the Dirac-cone-like band structure of germanene and stanene with a band gap of 0.003 ~ 0.185 eV opened at the Dirac-point. Germanene on CuI and stanene on CaI_2 are found to have odd Z_2 invariant, and the former one is a topological insulator. In addition, we have found that the interaction between germanene and the substrates can be well described by the tight binding Hamiltonian of germanene under uniform external fields. The analysis using the Hamiltonian shows that suitable substrates mainly act like a "pseudoelectric" field on germanene, whose field strength dominates the band gap and topological phase of germanene. The linear trade-off between the band gap and the average effective mass can be well reproduced when the band gap is below 0.4 eV. The fitted extrinsic Rashba coefficient is found to be almost linear to the "pseudoelectric" field, similar to its behavior under real electric field. We hope our research can shed light on the first synthesis of germanene and stanene with semiconducting Dirac-cone-like band structure and open up new areas of research for them.

5. Surface relaxation of tungsten ditelluride

5.1. Introduction

Generally speaking, surface reconstruction and relaxation of crystals widely exist with very rare exemptions due to the break of periodic condition and the change of the atomic dynamics at the surface of the crystal.[149] Reconstruction is significant change of the surface structure with respect to the bulk structure, including the change in periodicity and rotation angles, while relaxation is mild rigid shifts of atomic planes at the surface. [149] Surface relaxation are common in metals, characterized by the inward shrinking of the distance between the outermost atomic layer and the layer below compared to the bulk configuration. [150] Surface reconstructions and relaxations can be measured by several experimental techniques: (1) scattering experiments, including low-energy electron diffraction (LEED) and reflection high-energy electron diffraction (RHEED); (2) atomic scale microscopy, including scanning tunneling microscopy (STM) and atomic force microscopy (AFM).

As mentioned in Chapter 1, WTe_2 has a variety of exotic properties calling for further investigations, such as the non-saturating magneto resistance (MR) and the type-II Weyl cone[50,53,151,152]. An accurate structure of WTe_2 is the foundation of the investigation over its other properties. However, while the structure of bulk WTe_2 has been extensively investigate under various conditions,[47,48] the quantitative analysis of surface relaxation in WTe_2 has not been performed yet, which is crucial in obtaining better understanding of the exotic properties. Due to the 2D nature of WTe_2 with its layered structure, the carrier density, the ratio of electron and hole carrier densities and the transport properties strongly rely on the layer-resolved Fermi surface topology. The geometric structure at surface and subsurface regions may also influence MR and the Lifshitz transition[52] induced by temperature. Therefore, it is an urgent issue to determine the surface structure of WTe_2.

In this study, the surface structure of WTe_2 is determined by using LEED, STM and DFT calculations in cooperation with experiment group. Surface relaxation is found in the outermost WTe_2 layer by both experimental measures and theoretical simulations. Furthermore, the non-negligible impact of such relaxation on the Fermi surface topology is demonstrated by DFT calculations.

5.2. Methodology

All experiments were carried out by Kazuaki Kawahara *et al.* in Prof. Noriaki Takagi's group. Measurements are done in two ultrahigh vacuum (UHV) systems with a base pressure of 5.0×10^{-9} Pa for LEED and STM, respectively. Clean (001) surfaces were prepared in the UHV chamber by the exfoliation of WTe_2 crystals with adhesive tape. The LEED measurements were conducted at room temperature. The LEED I-V curves are functions of intensity of diffraction spot and incident electron energy, acquired by changing the incident electron energy with a step of 1 eV and further averaged over all symmetrically equivalent diffraction spots. Six I-V curves in total were obtained and analyzed by the Barbieri-Van Hove symmetrized automated tensor LEED package.[153] I-V curves of three phase shifts were used as theoretical comparison to the experimental ones, and the agreement are evaluated by using the Pendry R-factor (R_p).[154] The imaginary part of the inner potential was set to -5.0 eV. The STM topographic images were obtained in constant current mode with an electrically-etched W tip at 5K.

All DFT calculations were done by using Vienna Ab initio Simulation Package (VASP) [108,111] with the projected augmented wave (PAW) method.[54] Exchange and correlation functional was described at the level of generalized gradient approximation (GGA) parametrized by Perdew-Burke-Ernzerhof.[69] The cut off energy of the plane wave expansion used was 500 eV in variable-cell optimization and 400 eV in other calculations. We first determined the lattice constant of a 5-layer WTe_2 slab model by using various calculation setups including vdW interaction and spin polarization. The force tolerance was 0.001 eV/ Å. The lattice constants are determined to be $a = 3.49$ and $b = 6.28$ Å, which are in good agreement with the experimental values. [47,48] Using these lattice constants, we constructed a 7-layer slab model and optimized the geometric structure. All atoms were relaxed until the residual force constraints decrease below 0.01eV/Å. The opt-B86b functional was used to take the vdW interaction into account.[80–82,85]

5.3. Experimental part

The typical STM image of clean WTe_2 surface is presented in Figure 5-1 with clear array of lines. No steps and grain boundaries are found, and only very few defects are present in Figure 5-1b, indicating the high quality and homogeneity of the surface. High-resolution STM image, shown in Figure 5-1c, is well correlated with the expected STM image from the bulk termination. AA and BB lines in Figure 5-1c are consist of higher and lower Te atoms, respectively. The

periodicity of the surface structure is $a = 3.5$ and $b = 6.3$ Å, consistent with previous bulk unit cell X-ray diffraction[47,48] and surface STM measurements. [155,156] The tensor LEED analysis based on the bulk structure shows that the surface structure is closest to the Td structure, i.e. same category as the bulk part. Furthermore, the height difference of atoms in the outmost layer, i.e. $z_1 \sim z_6$ in Figure 5-1a, is slightly different from the bulk counterparts, as listed in the first column of Table 5-1. Specifically, the buckling of the outermost Te atoms (z_1) reduces to 0.57 ± 0.04 Å from that of the bulk (0.61 Å), while the underneath buckling (z_2) increases to 1.41 ± 0.07 Å from 1.36 Å in the bulk. $z_3 \sim z_6$ are almost identical to the bulk value within the error bar of experiment.
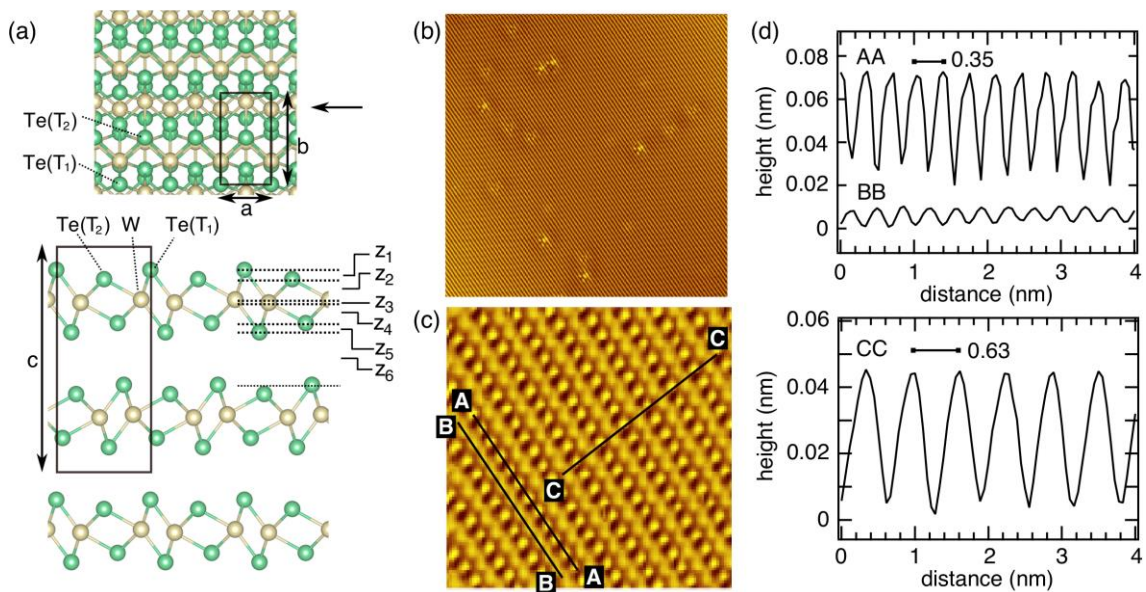
Figure 5-1: (a) Schematic structural model of WTe$_2$. The unit cell is indicated by black rectangles. The corresponding lattice constants are a, b and c. The lower figure is the side view along a. $z_1 \sim z_6$ are the height differences of atoms, i.e. the distance between atomic planes in the (001) direction. (b) 50 nm × 50 nm topographic STM image of WTe$_2$ with sample voltage of 0.58 V and tunneling current of 0.1 nA. (c) 6 nm×6 nm high-resolution STM image of WTe$_2$ with sample voltage of 51 mV and tunneling current of 0.1 nA. (d) Height profiles along with the lines of AA, BB and CC shown in (c).

5.4. Theoretical part

To validate the results given by experiment, DFT optimizations are performed for a 7-layer WTe$_2$ slab to obtain the most preferable surface structure. The surface relaxation observed in the DFT calculations is consistent with the LEED results. The values of $z_1 \sim z_6$ in the optimized

structure are summarized in Table 5-1. Although the differences from the bulk, i.e. the absolute values of $z_1 \sim z_6$, are smaller than those determined by the LEED analysis in the first column, the tendency of the structural variations in respective atomic layers matches well with the LEED results, namely z_1 reduces and z_2 extends. Furthermore, the DFT calculations also find structure variations in $z_3 \sim z_6$; the buckling between two W atomic layers (z_3) reduces, the distance between the lower W and the bottom Te atomic layers (z_4) is almost preserved, the buckling in the lower Te atomic layer (z_5) increases, and the interlayer distance between the outermost WTe$_2$ layer and the layer beneath (z_6) decreases. The contraction and extension of the buckling distance occur alternatively with a gradually reduced magnitude as it goes into deeper layers. Such a damped oscillating behavior is commonly found in metallic surfaces from clean to adsorbate-covered ones.[157] The characteristic point in WTe$_2$ is that the relaxation is almost localized in the topmost or bottommost WTe$_2$ layer in the whole 7-layer slab, as shown in Figure 5-2. The vdW interaction between layers in WTe$_2$ is not strong, preventing relaxation to prevail into the inner layers.

Table 5-1: $z_1 \sim z_6$ in the WTe$_2$ surface determined by LEED and DFT calculations. The bulk counterparts [47] are also provided for comparison. In the DFT calculation results, the values in the 4th layer are regarded as the bulk values.

	WTe$_2$ surface (LEED)	Bulk[47]	WTe$_2$ surface (DFT)	Bulk (DFT)
z_1	0.57 ± 0.04 Å	0.61 Å	0.62 Å	0.64 Å
z_2	1.41 ± 0.07 Å	1.36 Å	1.37 Å	1.35 Å
z_3	0.19 ± 0.05 Å	0.21 Å	0.22 Å	0.22 Å
z_4	1.36 ± 0.05 Å	1.36 Å	1.35 Å	1.35 Å
z_5	0.65 ± 0.08 Å	0.61 Å	0.64 Å	0.64 Å
z_6	2.85 ± 0.08 Å	2.88 Å	2.90 Å	2.91 Å

It is intriguing to compare the surface relaxation of WTe$_2$ with the other members of the TDMC family. Surprisingly, the surface structure analysis for the TDMCs are scarce despite of the high research interest focused on them globally. Nevertheless, the surface structures of MoS$_2$

and NbSe$_2$ determined by LEED are available for comparison. Although these two materials take the H structure instead of the Td structure of WTe$_2$, the comparison with the present results can still provide a good opportunity to investigate the surface relaxation caused by termination of periodic boundary, or more specifically the disappearance of the weak vdW interaction at the vacuum-solid interface. Small surface relaxation are also found for MoS$_2$.[158] The buckling distance between the topmost S layer and the Mo layer underneath shrinks by several percent from the bulk value. In contrast, the surface structure of NbSe$_2$ is almost identical to the bulk within the experimental accuracy.[158] Such presence/absence of the relaxation may be related to their own electronic structures. The magnitude of the surface relaxation has the sequence of MoS$_2$ > WTe$_2$ > NbSe$_2$. At the same time, the metallicity of them are semiconducting, semimetallic and metallic, representing an increasing conductivity. The surface relaxation in WTe$_2$ is more similar to semiconducting MoS$_2$ rather than metallic NbSe$_2$, possibly due to the low density of state at the Fermi level in WTe$_2$.
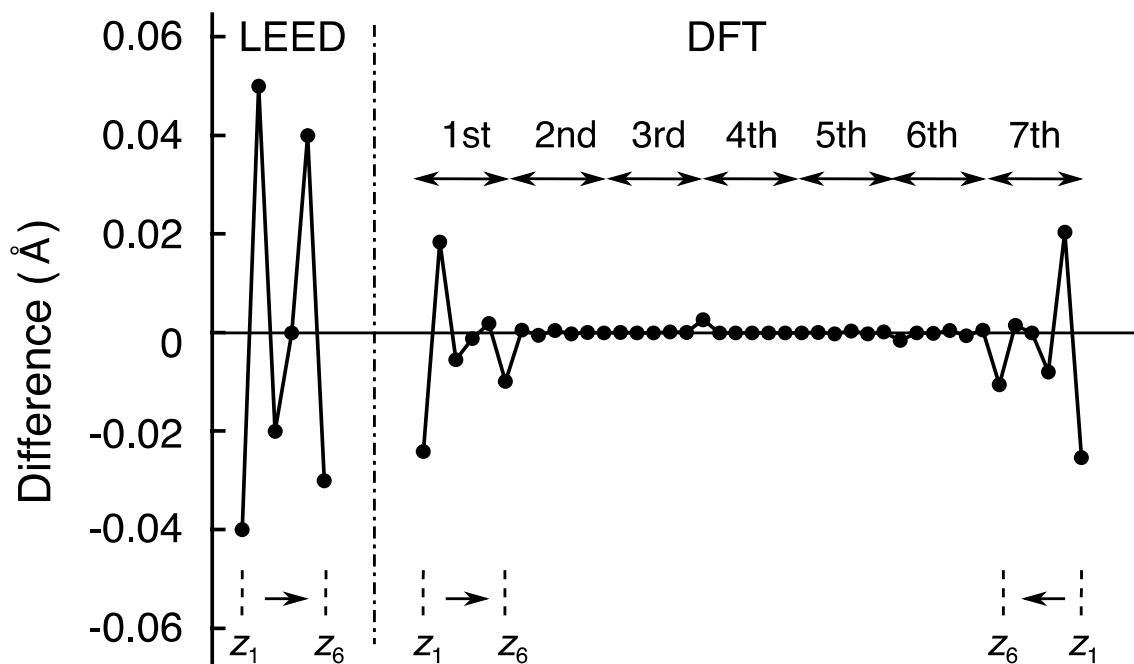
Figure 5-2: Differences of $z_1 \sim z_6$ in each layer from the bulk counterparts obtained by the DFT calculations for the 7-layer slab model together with the LEED results. The values in the second and forth columns of Table I are used as the bulk counterparts for the LEED and DFT results, respectively. Note that the differences in the bottommost layer (7th layer) are in the sequence of z-coordinate from bottom to top.
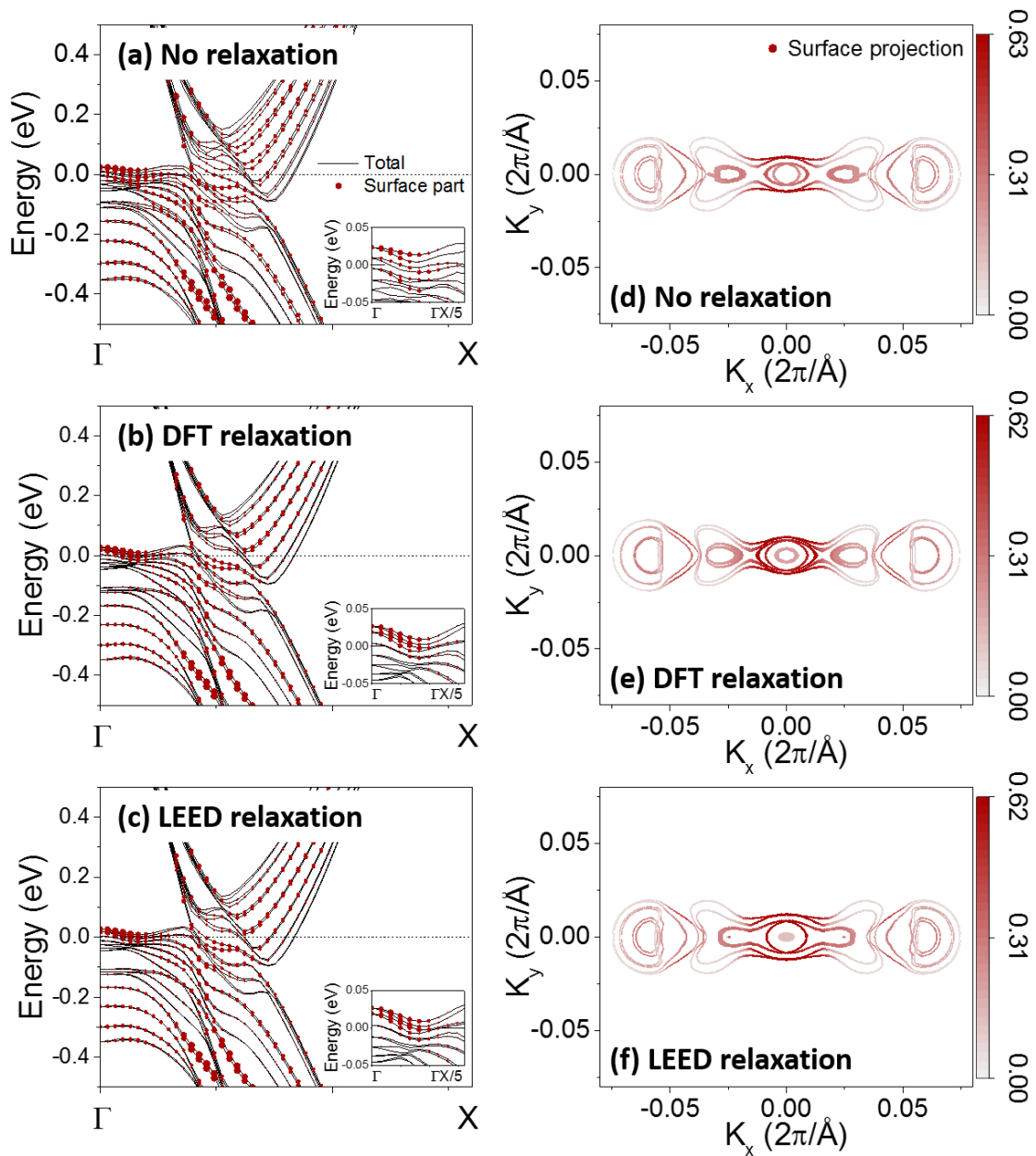
Figure 5-3: Variations of (a-c) band structure along the ΓX line and (d-f) Fermi surface topology with the surface relaxation calculated for the 7-layer WTe₂ slab. The length of the ΓX line is 0.14 (2π/Å). The insets in (a-c) show magnified band structures around the Γ point along the ΓX line around the Fermi level. The calculations were done for (a, d) the bulk structure, (b, e) one optimized by DFT, and (c, f) one which surface is relaxed according to the LEED results with holding the other atoms in the bulk positions. Red filled circles in (a-c) and the color bar in (d-f) indicate the contribution from the 1st and 7th layers, i.e. the surface layers.

Finally, the effect of the surface relaxation on the Fermi surface topology and electron/hole (n/p) ratio is discussed here. The band structures of WTe_2 slabs with different surface relaxations given by bulk structure (no relaxation), DFT and LEED analysis are displayed in Figure 5-3. Note that the amplitude of relaxation given by DFT is smaller than that given by LEED analysis, Figure 5-3 can also be viewed as the band structure of WTe_2 slab when the surface relaxation is gradually introduced. Figure 5-3a shows the band structure calculated for the 7-layer slab without surface relaxation, where Te and W atoms are placed in the same positions as those in the bulk. The band structure mainly consists of two downward- and upward-convex branches derived from the bulk. These branches are split due to interlayer-hopping and SOC. They cross the Fermi level to form the electron and hole pockets, respectively. The overall feature nicely agrees with previous studies.[53,159] In addition to these features, the surface state appears around the Γ point near the Fermi level indicated by large red dots in Figure 5-3a. The band dispersion calculated for the structure optimized by the DFT shows slight upward shift of the surface state compared to that of the bulk (Figure 5-3b and inset). With the surface relaxation determined by the LEED analysis, the surface state moves upward further compared to the DFT structure (Figure 5-3c and inset), so we conclude that the amplitude of upward shift in the surface state at the Γ point is positively proportional to the degree of surface relaxation within our studied range. Even though the upward shift in the band structure seems to be minute, it induces a remarkable change in the Fermi surface topology. Comparing Figure 5-3d, e and f, the topology evolves in accordance with the variation of the surface state. The hole-pockets around the Γ point and $K_x = \pm 0.025$ enlarge and merge with each other from Figure 5-3d to e and f.

The variation of the Fermi surface topology would change the ratio of the electron (n) and hole (p) carrier densities responsible for the exotic transport properties. The n/p ratio can be calculated by the band-decomposed density of states, and can further be projected to each layer by using local density of states through atomic orbital projections. We use a 100×100 k-point grid to calculate the high-accuracy n/p ratio of the 7-layer WTe_2 slab. The result is shown in Figure 5-4. Both the structure given by DFT and LEED analysis has a total n/p ratio near 1.5, which is in good agreement with previous experiment result of few-layer WTe_2.[160] Impressively in both cases, the 7th layer is rich in the electron carrier with $n/p > 1$, while the 1st layer is much richer in the hole carrier with n/p around 0.5. The 6th layer has the highest n/p, which is attributed to the

result of surface dipole and needs further investigation. The amplitude of relaxation does not affect the total *n/p* very much, but significantly affects the surface *n/p* ratio as expected. The *n/p* ratio of the surfaces layers in the DFT structure is 0.5 (L1) and 1.2 (L7), much closer to 1.0 compared to 0.4 (L1) and 1.5 (L7) the structure from LEED analysis. Note that in the LEED structure the n/p ratio of the 7th layer is almost the same as the total *n/p* value, so currently we cannot judge whether the experimentally measured *n/p* ratio belongs to the whole slab or just one side of the surface layer.
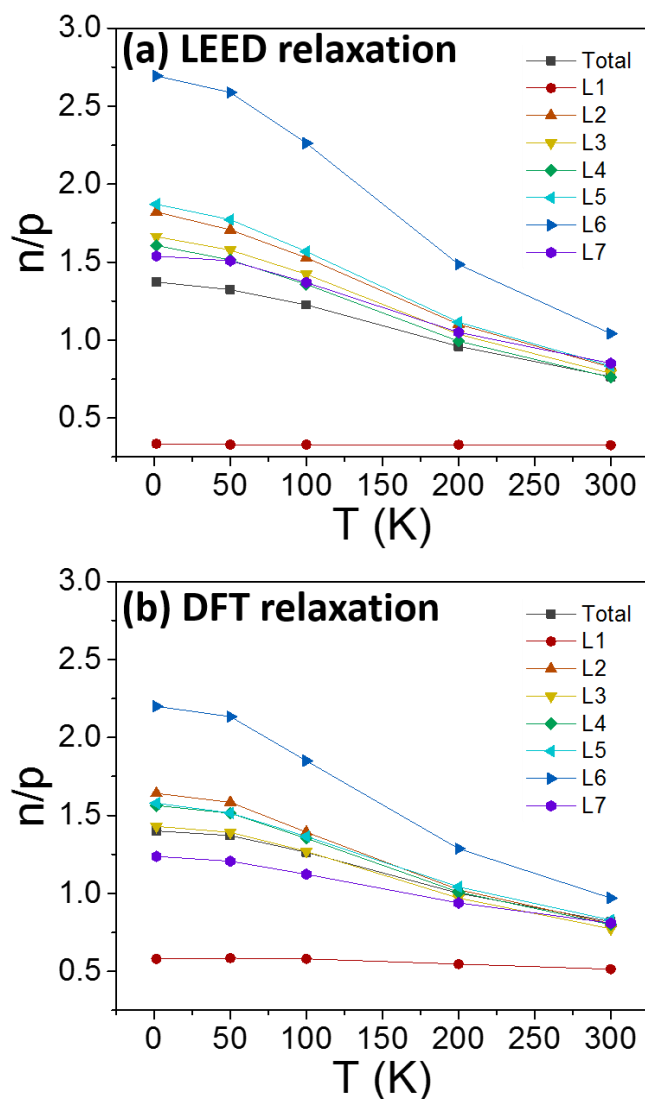
Figure 5-4: Layer projected electron/hole ratio of the 7-layer WTe2 with surface relaxation from (a) LEED and (b) DFT optimization. L1-L7 indicate layer 1~7, respectively. Total denotes the *n/p* ratio of the whole 7-layer WTe$_2$ slab.

5.5. Conclusions

In summary, we have investigated the atomic structure of the WTe_2 surface by combining tensor LEED, STM and DFT calculations. We find a small but non-negligible surface relaxation in the outermost monolayer of WTe_2. The tensor LEED analysis reveals that the buckling in the outermost Te layer reduces to 0.57 ± 0.04 Å from that of the bulk (0.61 Å). At the same time, the distance between the outermost Te layer and the W layer underneath slightly extends. The DFT calculations can reproduce similar relaxation trend gradually decaying in an oscillatory manner inside the first WTe_2 layer. In addition, the DFT calculations reveal that the Fermi surface topology and the layer-wise *n/p* ratio is dependent on the surface relaxation. The total *n/p* ratio is around 1.5 and is not strongly affected by the surface relaxation, while the surface *n/p* ratio is further away from 1.0 with larger relaxation magnitude. These results are helpful for the better understanding of the exotic properties of WTe_2 such as MR.

6. Summary and prospects

In this dissertation, we use the first principle calculations to investigate the surface/interface properties of novel 2D materials, including germanene, stanene and WTe_2, and use materials informatics to explore the optimal interface to preserve the geometry and exotic properties of germanene and stanene. The word "optimization" in the title means both geometric optimization of surface/interface structure (by DFT) and selection of optimal interfaces (by materials search).

In Chapter 1, a brief introduction about Moore's law, novel 2D materials in general, germanene and stanene, WTe_2, and topological insulators is given. We point out that germanene and stanene are more suitable for spintronic devices compared to graphene due to their larger spin-orbit coupling (SOC), but they still lack semiconducting substrates that can preserve their Dirac-cones and band gaps in experiment. We also point out that WTe_2 has unsaturated magneto resistance at an external magnetic field over 50 T, but the surface relaxation and its impact still remain untouched.

In Chapter 2, the methodologies used in this work are introduced, including the density functional theory (DFT), Z_2 topological invariant calculation, and materials search by data mining.

In Chapter 3, the research about group III monochalcogenides (MX) as suitable substrates for germanene is presented. By using DFT, we find that germanene can preserve its low-buckled geometry and Dirac-cone-like band structure on MX like in its free-standing case in the most energetically preferable configuration considering the van der Waals (vdW) interaction. Furthermore, germanene on GaTe and InSe is semiconducting with a band gap of 0.14 ~ 0.16 eV predicted by hybrid functional calculations. The effective masses at the Dirac point of germanene remain as small as 0.05 ~ 0.06 times the free electron mass, leading to an ultrahigh carrier mobility estimated to be up to 2.2×10^5 $cm^2V^{-1}s^{-1}$. The band splitting caused by the SOC can be up to 42 meV, which suggests that this system may have potential for room temperature quantum spin Hall material. Molecular dynamics calculations show that germanene's structure on MX will not be destroyed under 500K. In addition, we find that multilayer MX can also serve as a suitable substrate for germanene, so the (001) surface of bulk MX may be a good candidate.

In Chapter 4, the materials search for the suitable substrates for germanene and stanene is presented. We use data mining to filter out suitable 2D substrate candidates for germanene and stanene that can preserve their geometric structures and Dirac-cones. After that, DFT calculations are performed to examine whether the substrate is truly suitable. According to our calculation,

germanene can preserve its Dirac-cone on CdI_2, ZnI_2, GeI_2, MgI_2 and GaGeTe with stable quasi-free-standing structures. We have also found two suitable substrates for stanene, namely PbI_2 and CaI_2, using the same method. The discovered substrates are all real materials, some of which has been used before as the substrate for vdW epitaxial growth, like CdI_2 and PbI_2. Moreover, atomically thin film of PbI_2 has been synthesized experimentally. We have performed geometry optimization and then investigate the phonon dispersions, band structures and Z_2 invariants of the germanene-substrate system. The distance between suitable substrates and germanene is rather large (>3 Å) after optimization with a very small binding energy of 15 ~ 20 meV/Å^2. On suitable substrates, supported germanene preserves Dirac-cone-like band structure near the K point with a small band gap opened, whose size ranges from nearly zero to about 0.18 eV. Interestingly, the effective mass of germanene has almost perfect linear relationship with the band gap size, and the Z_2 invariant of germanene is also changed from 1 to 0 on most substrates, indicating the occurrence of a topological phase transition of germanene, although the interaction is vdW-like. To explain the above phenomenon and the different Z_2 on different substrates, we fit the DFT bands of the supported germanene by the tight binding Hamiltonian of freestanding germanene under external fields and find that the substrate acts mainly like a pseudoelectric field. The external Rashba coefficient and the charge transfer between germanene and the substratate are found to have linear relationship with the pseudoelectric field strength.

In Chapter 5, the surface relaxation of WTe_2 is investigated. In experiment, which is not a part of this dissertation but is introduced briefly, tensor low-energy electron diffraction (LEED) analysis determines that WTe_2 has finite surface relaxation with a damped oscillation in the buckling of crystallographic atomic planes. In this work, such damped oscillation is verified by the DFT calculation of a 7-layer WTe_2 slab. Furthermore, the presence of the surface reconstruction will affect the band structure, Fermi surface and the ratio of electron and hole carriers of the surface of WTe_2. The surface-projected bands at the Γ point with surface reconstruction are slightly left up compared to bulk-like structure. Corresponding to the evolution of the band structure, the topology of the rings at the Fermi surface differs as well. The ratio between electron and hole carriers is also changed by the surface relaxation. One of the surface is electron-rich, while the other is hole-rich. With the surface relaxation, the electron-rich surface will have higher ratio, i.e. more electron-rich, and the hole-rich one will have lower ratio, i.e. more hole-rich. These results demonstrate that the surface relaxation has non-negligible impact

on the electronic structure and possibly also on the magnetoresistance according to the two-band model.

In summary, we have theoretically investigated the surface/interface optimization and property of novel 2D materials with substrate interaction or surface relaxation. *First*, suitable substrates, like group III monochalcogenides by intuitive guess and more by data mining, have been filtered out for germanene and stanene to preserve their exotic properties in order to speed up their practical application. Further research can be conducted in the following ways: (1) The materials search is possible to be expanded to other novel 2D materials, like phosphorene and arsenene. (2) The substrates found for germanene and stanene can be used to form vertical sandwiched heterostructure, which can further protect germanene and stanene from ambient environment and tune their properties. It might be important for practical application, especially for improving the life time of germanene and stanene devices. (3) Further improvement in the materials search procedure might be possible. The selection method for 2D materials still contains an empirical coefficient. Materials with non-1×1 stacking can also be taken into account. 3D materials, although less possible to be suitable for germanene and stanene, can also be taken into account. *Second*, finite surface relaxation in WTe_2 is found, and its impact on the electronic structure and carrier compensation of WTe_2 is investigated. Further research can be done such as investigation of how the surface relaxation and carrier compensation change as the number of layers in WTe_2 slab decrease to monolayer. We expect future development for the content of this dissertation in the above directions.

Reference

1.   Waldrop, M.M. *Nature* **530**, 144–147 (2016).

2.   Ieong, M. *Science* **306**, 2057–2060 (2004).

3.   Farmer, D.B. et al. *Nano Lett.* **9**, 388–392 (2009).

4.   Bin Yu et al. *Dig. Int. Electron Devices Meet.* 251–254 (2002).doi:10.1109/IEDM.2002.1175825

5.   Geim, A.K. & Novoselov, K.S. *Nat. Mater.* **6**, 183–191 (2007).

6.   Lu, C.-P., Li, G., Mao, J., Wang, L.-M. & Andrei, E.Y. *NANO Lett.* **14**, 4628–4633 (2014).

7.   Pei, J. et al. *Nat. Commun.* **7**, (2016).

8.   Kang, J., Liu, W., Sarkar, D., Jena, D. & Banerjee, K. *Phys. Rev. X* **4**, 31005 (2014).

9.   Bhimanapati, G.R. et al. *ACS Nano* **9**, 11509–11539 (2015).

10. Schwierz, F. *Proc. IEEE* **101**, 1567–1584 (2013).

11. Novoselov, K.S. et al. *Nature* **438**, 197–200 (2005).

12. Kane, C.L. & Mele, E.J. *Phys. Rev. Lett.* **95**, 226801 (2005).

13. Qi, X.L. & Zhang, S.C. *Rev. Mod. Phys.* **83**, (2011).

14. Moore, J.E. *Nature* **464**, 194–8 (2010).

15. Qi, X.L. & Zhang, S.C. *Phys. Today* **63**, 33–38 (2010).

16. Service, R.F. *Science* **348**, 490–492 (2015).

17. Cahangirov, S., Topsakal, M., Aktürk, E., Šahin, H. & Ciraci, S. *Phys. Rev. Lett.* **102**, 236804 (2009).

18. Ezawa, M. *Phys. Rev. Lett.* **109**, 55502 (2012).

19. Liu, C.C., Feng, W. & Yao, Y. *Phys. Rev. Lett.* **107**, 76802 (2011).

20. Wang, M., Liu, L., Liu, C.-C.C. & Yao, Y. *Phys. Rev. B - Condens. Matter Mater. Phys.* **93**, 155412 (2016).

21. Xu, Y. et al. *Phys. Rev. Lett.* **111**, 136804 (2013).

22. Yao, Y., Ye, F., Qi, X.L., Zhang, S.C. & Fang, Z. *Phys. Rev. B - Condens. Matter Mater. Phys.* **75**, 41401 (2007).

23. Ezawa, M. *J. Supercond. Nov. Magn.* **28**, 1249–1253 (2015).

24. Li, L. et al. *Adv. Mater.* **26**, 4820–4824 (2014).

25. Dávila, M.E., Xian, L., Cahangirov, S., Rubio, A. & Lay, G. Le *New J. Phys.* **16**, 95002 (2014).

26. Derivaz, M. et al. *Nano Lett.* **15**, 2510–2516 (2015).

27. Zhu, F. et al. *Nat. Mater.* **14**, 1020–1025 (2015).

28. Ni, Z. et al. *Nano Lett.* **12**, 113–118 (2012).

29. Ni, Z. et al. *Nanoscale* **6**, 7609–18 (2014).

30. Ye, M. et al. *Phys. E Low-Dimensional Syst. Nanostructures* **59**, 60–65 (2014).

31. Drummond, N.D., Zólyomi, V. & Fal'Ko, V.I. *Phys. Rev. B - Condens. Matter Mater. Phys.* **85**, 75423 (2012).

32. Ezawa, M. *New J. Phys.* **14**, 33003 (2012).

33. Ye, X.-S., Shao, Z.-G., Zhao, H., Yang, L. & Wang, C.-L. *RSC Adv.* **4**, 21216–21220 (2014).

34. Yan, J.-A., Stein, R., Schaefer, D.M., Wang, X.-Q. & Chou, M.Y. *Phys. Rev. B* **88**, 121403 (2013).

35. Bishnoi, B. & Ghosh, B. *RSC Adv.* **3**, 26153–26159 (2013).

36. Zhang, L. et al. *Phys. Rev. Lett.* **116**, 256804 (2016).

37. Amlaki, T., Bokdam, M. & Kelly, P.J. *Phys. Rev. Lett.* **116**, 256805 (2016).

38. Kaloni, T.P. & Schwingenschlögl, U. *J. Appl. Phys.* **114**, 184307 (2013).

39. Chen, M.X., Zhong, Z. & Weinert, M. *Phys. Rev. B* **94**, 75409 (2016).

40. Kappera, R. et al. *Nat. Mater.* **13**, 1128–1134 (2014).

41. Mak, K.F., Lee, C., Hone, J., Shan, J. & Heinz, T.F. *Phys. Rev. Lett.* **105**, 136805 (2010).

42. Xiao, D., Liu, G.-B., Feng, W., Xu, X. & Yao, W. *Phys. Rev. Lett.* **108**, 196802 (2012).

43. Gong, Z. et al. *Nat. Commun.* **4**, 2053 (2013).

44. Xu, X., Yao, W., Xiao, D. & Heinz, T.F. *Nat. Phys.* **10**, 343–350 (2014).

45. Jones, A.M. et al. *Nat. Phys.* **10**, 130–134 (2014).

46. Lu, P. et al. *Phys. Rev. B* **94**, 224512 (2016).

47. Brown, B.E. *Acta Crystallogr.* **20**, 268–274 (1966).

48. Mar, A., Jobic, S. & Ibers, J. a *J. Am. Chem. Soc.* **114**, 8963–8971 (1992).

49. Das, P.K. et al. *Nat. Commun.* **7**, 7 (2016).

50. Ali, M.N. et al. *Nature* **514**, 205–8 (2014).

51. Kang, D. et al. *Nat. Commun.* **6**, 7804 (2015).

52. Wu, Y. et al. *Phys. Rev. Lett.* **115**, 166602 (2015).

53. Soluyanov, A.A. et al. *Nature* **527**, 495–8 (2015).

54. Blöchl, P.E. *Phys. Rev. B* **50**, 17953–17979 (1994).

55. Hasan, M.Z. & Kane, C.L. *Rev. Mod. Phys.* **82**, 3045–3067 (2010).

56. (Springer New York: New York, NY, 1990).doi:10.1007/978-1-4612-3350-3

57. Klitzing, K. V., Dorda, G. & Pepper, M. *Phys. Rev. Lett.* **45**, 494–497 (1980).

58. Thouless, D.J., Kohmoto, M., Nightingale, M.P. & den Nijs, M. *Phys. Rev. Lett.* **49**, 405–408 (1982).

59. Chern, S. *Ann. Math.* **47**, 85 (1946).

60. Xiao, D., Chang, M.C. & Niu, Q. *Rev. Mod. Phys.* **82**, 1959–2007 (2010).

61. Fu, L. & Kane, C.L. *Phys. Rev. B* **74**, 195312 (2006).

62. Bernevig, B.A., Hughes, T.L. & Zhang, S.-C. *Science* **314**, 1757–1761 (2006).

63. Born, M. & Oppenheimer, R. *Ann. Phys.* **389**, 457–484 (1927).

64. Ferrario, M., Ciccotti, G. & Binder, K. (SPRINGER: New York, 2006).doi:10.1007/b11604457

65. Hohenberg, P. & Kohn, W. *Phys. Rev.* **136**, B864–B871 (1964).

66. Mermin, N.D. *Phys. Rev.* **137**,   (1965).

67. Jones, R.O. & Gunnarsson, O. *Rev. Mod. Phys.* **61**, 689–746 (1989).

68. Kohn, W. & Sham, L.J. *Phys. Rev.* **140**,   (1965).

69. Perdew, J.P., Burke, K. & Ernzerhof, M. *Phys. Rev. Lett.* **77**, 3865 (1996).

70. Heyd, J., Scuseria, G.E. & Ernzerhof, M. *J. Chem. Phys.* **118**, 8207–8215 (2003).

71. Heyd, J., Scuseria, G.E. & Ernzerhof, M. *J. Chem. Phys.* **124**, 219906 (2006).

72. Krukau, A. V., Vydrov, O.A., Izmaylov, A.F. & Scuseria, G.E. *J. Chem. Phys.* **125**, (2006).

73. Heyd, J. & Scuseria, G.E. *J. Chem. Phys.* **121**, 1187–1192 (2004).

74. Berland, K. et al. *Reports Prog. Phys.* **78**, 66501 (2015).

75. Kganyago, K.R. & Ngoepe, P.E. *Phys. Rev. B* **68**, 205111 (2003).

76. Rydberg, H. et al. *Surf. Sci.* **532–535**, 606–610 (2003).

77. Berland, K. & Hyldgaard, P. *Phys. Rev. B - Condens. Matter Mater. Phys.* **87**, 1–15 (2013).

78. Klime, J. et al. *Phys. Rev. B - Condens. Matter Mater. Phys.* **83**, 195131 (2011).

79. Lundqvist, B.I., Andersson, Y., Shao, H., Chan, S. & Langreth, D.C. *Int. J. Quantum Chem.* **56**, 247–255 (1995).

80. Dion, M., Rydberg, H., Schröder, E., Langreth, D.C. & Lundqvist, B.I. *Phys. Rev. Lett.* **92**, 246401 (2004).

81. Thonhauser, T. et al. *Phys. Rev. B - Condens. Matter Mater. Phys.* **76**, 125112 (2007).

82. Román-Pérez, G. et al. *Phys. Rev. Lett.* **103**, 1–4 (2009).

83. Lee, K., Murray, É.D., Kong, L., Lundqvist, B.I. & Langreth, D.C. *Phys. Rev. B - Condens. Matter Mater. Phys.* **82**, 3–6 (2010).

84. Hamada, I. *Phys. Rev. B* **89**, 121103 (2014).

85. Klimeš, J. et al. *J. Phys. Condens. Matter* **22**, 22201 (2010).

86. Vydrov, O.A. & Van Voorhis, T. *Phys. Rev. Lett.* **103**, 7–10 (2009).

87. Wang, Z., Selbach, S.M. & Grande, T. *RSC Adv.* **4**, 4069–4079 (2014).

88. Soluyanov, A.A. & Vanderbilt, D. *Phys. Rev. B* **83**, 235401 (2011).

89. Fu, L. & Kane, C.L. *Phys. Rev. B - Condens. Matter Mater. Phys.* **76**, 1–17 (2007).

90. Zhang, H. et al. *Nat. Phys.* **5**, 438–442 (2009).

91.   Lebègue, S., Björkman, T., Klintenberg, M., Nieminen, R.M. & Eriksson, O. *Phys. Rev. X* **3**, 31002 (2013).

92.   Klintenberg, M., Derenzo, S.E. & Weber, M.J. *Nucl. Instruments Methods Phys. Res. Sect. A Accel. Spectrometers, Detect. Assoc. Equip.* **486**, 298–302 (2002).

93.   Ortiz, C., Eriksson, O. & Klintenberg, M. *Comput. Mater. Sci.* **44**, 1042–1049 (2009).

94.   Klintenberg, M. (2010).at <http://arxiv.org/abs/1007.4838>

95.   Belsky, A., Hellenbrandt, M., Karen, V.L. & Luksch, P. *Acta Crystallogr. Sect. B Struct. Sci.* **58**, 364–369 (2002).

96.   Kokott, S., Matthes, L. & Bechstedt, F. *Phys. Status Solidi - Rapid Res. Lett.* **7**, 538–541 (2013).

97.   Matusalem, F., Bechstedt, F., Marques, M. & Teles, L.K. *Phys. Rev. B* **94**, 241403 (2016).

98.   Martínez-Pastor, J., Segura, A., Valdés, J.L. & Chevy, A. *J. Appl. Phys.* **62**, 1477–1483 (1987).

99.   Late, D.J., Liu, B., Matte, H.S.S.R., Rao, C.N.R. & Dravid, V.P. *Adv. Funct. Mater.* **22**, 1894–1905 (2012).

100.   Hu, P. et al. *Nano Lett.* **13**, 1649–1654 (2013).

101.   Lei, S. et al. *Nano Lett.* **13**, 2777–2781 (2013).

102.   Koma, A. *J. Cryst. Growth* **201**, 236–241 (1999).

103.   Lei, S. et al. *ACS Nano* **8**, 1263–1272 (2014).

104.   Zhuang, H.L. & Hennig, R.G. *Chem. Mater.* **25**, 3232–3238 (2013).

105.   Ding, Y. & Wang, Y. *Appl. Phys. Lett.* **103**, 43114 (2013).

106.   Scalise, E. et al. *2D Mater.* **1**, 11010 (2014).

107.   Giannozzi, P. et al. *J. Phys. Condens. Matter* **21**, 395502 (2009).

108.   Kresse, G. & Furthmüller, J. *Phys. Rev. B* **54**, 11169–11186 (1996).

109.   Pack, J.D. & Monkhorst, H.J. *Phys. Rev. B* **16**, 1748–1749 (1977).

110.   Bengtsson, L. *Phys. Rev. B* **59**, 12301–12304 (1999).

111.   Kresse, G. & Joubert, D. *Phys. Rev. B* **59**, 1758–1775 (1999).

112.   Ohno, K., Esfarjani, K. & Kawazoe, Y.**129**,   (Springer Berlin Heidelberg: Berlin, Heidelberg, 1999).

113.   Tang, W., Sanville, E. & Henkelman, G. *J. Phys. Condens. Matter* **21**, 84204 (2009).

114.   Henkelman, G., Arnaldsson, A. & Jónsson, H. *Comput. Mater. Sci.* **36**, 354–360 (2006).

115.   Sanville, E., Kenny, S.D., Smith, R. & Henkelman, G. *J. Comput. Chem.* **28**, 899–908 (2007).

116.   Wang, Y. & Ding, Y. *Solid State Commun.* **155**, 6–11 (2013).

117.   Schwierz, F. *Nat. Nanotechnol.* **5**, 487–496 (2010).

118. Bolotin, K.I. et al. *Solid State Commun.* **146**, 351–355 (2008).

119. Chen, J.-H., Jang, C., Xiao, S., Ishigami, M. & Fuhrer, M.S. *Nat. Nanotechnol.* **3**, 206–209 (2008).

120. Lin, M.W. et al. *Phys. Rev. B - Condens. Matter Mater. Phys.* **84**, 125411 (2011).

121. Wang, J., Zhao, R., Yang, M., Liu, Z. & Liu, Z. *J. Chem. Phys.* **138**, 84701 (2013).

122. Yu, W.J. et al. *Nat. Nanotechnol.* **8**, 952–8 (2013).

123. Britnell, L. et al. *Science* **335**, 947–950 (2012).

124. Ni, Z., Minamitani, E., Ando, Y. & Watanabe, S. *Phys. Chem. Chem. Phys.* **17**, 19039–19044 (2015).

125. Ding, Y. & Wang, Y. *J. Phys. Chem. C* **119**, 27848–27854 (2015).

126. Fang, Y. et al. *Sci. Rep.* **5**, 14196 (2015).

127. Otwinowski, Z. & Minor, W. *Int. Tables Crystallogr.* **G**, (International Union of Crystallography: Chester, England, 2006).

128. Dal Corso, A. *Comput. Mater. Sci.* **95**, 337–350 (2014).

129. Hamann, D.R. *Phys. Rev. B* **88**, 85117 (2013).

130. Schlipf, M. & Gygi, F. *Comput. Phys. Commun.* **196**, 36–44 (2015).

131. Mostofi, A.A. et al. *Comput. Phys. Commun.* **178**, 685–699 (2008).

132. Mostofi, A.A. et al. *Comput. Phys. Commun.* **185**, 2309–2310 (2014).

133. See Supplemental Materialat <See Supplemental Material at webpage for further information>

134. Scalise, E. et al. *Nano Res.* **6**, 19–28 (2013).

135. Huang, L.-F., Gong, P.-L. & Zeng, Z. *Phys. Rev. B* **91**, 205433 (2015).

136. Takeyama, S., Watanabe, K., Ichihara, M., Suzuki, K. & Miura, N. *J. Appl. Phys.* **68**, 2735–2738 (1990).

137. Wang, Y., Sun, Y.-Y., Zhang, S., Lu, T.-M. & Shi, J. *Appl. Phys. Lett.* **108**, 13105 (2016).

138. Yan, J.-A., Gao, S.-P., Stein, R. & Coard, G. *Phys. Rev. B* **91**, 245403 (2015).

139. Qiao, J., Kong, X., Hu, Z.-X., Yang, F. & Ji, W. *Nat. Commun.* **5**, 4475 (2014).

140. Lee, H.S. et al. *ACS Nano* **9**, 8312–8320 (2015).

141. Pikulin, D.I., Chen, A. & Franz, M. *Phys. Rev. X* **6**, 1–20 (2016).

142. Sasaki, K.I., Gotoh, H. & Tokura, Y. *Phys. Rev. B - Condens. Matter Mater. Phys.* **90**, 1–8 (2014).

143. Levy, N. et al. *Science* **329**, 544–547 (2010).

144. Tse, W.-K., Qiao, Z., Yao, Y., MacDonald, A.H. & Niu, Q. *Phys. Rev. B* **83**, 155447 (2011).

145. Sheng, D.N., Weng, Z.Y., Sheng, L. & Haldane, F.D.M. *Phys. Rev. Lett.* **97**, 36808

(2006).

146. Min, H. et al. *Phys. Rev. B* **74**, 165310 (2006).

147. Trivedi, S., Srivastava, A. & Kurchania, R. *J. Comput. Theor. Nanosci.* **11**, 781–788 (2014).

148. Strinati, G., Mattausch, H.J. & Hanke, W. *Phys. Rev. Lett.* **45**, 290–294 (1980).

149. Zieliński, P. *Acta Phys. Pol. A* **89**, 251–263 (1996).

150. Methfessel, M., Hennig, D. & Scheffler, M. *Phys. Rev. B* **46**, 4816–4829 (1992).

151. Pletikosi??, I., Ali, M.N., Fedorov, A. V., Cava, R.J. & Valla, T. *Phys. Rev. Lett.* **113**, (2014).

152. Feng, B. et al. *arXiv* 1–5 (2016).at <http://arxiv.org/abs/1606.00085>

153. Van Hove, M.A. et al. *Surf. Sci. Rep.* **19**, 191–229 (1993).

154. Pendry, J.B. *J. Phys. C Solid State Phys.* **13**, 937 (1980).

155. Crossley, A., Myhra, S. & Sofield, C.J. *Surf. Sci.* **318**, 39–45 (1994).

156. Hla, S.W., Marinković, V., Prodan, A. & Muševič, I. *Surf. Sci.* **352**–**354**, 105–111 (1996).

157. Titmuss, S., Wander, A. & King, D. a. *Chem. Rev.* **96**, 1291–1306 (1996).

158. Mrstik, B.J., Kaplan, R., Reinecke, T.L., Van Hove, M. & Tong, S.Y. *Phys. Rev. B* **15**, 897–900 (1977).

159. Bruno, F.Y. et al. *Phys. Rev. B* **94**, 121112 (2016).

160. Wang, L. et al. *Nat. Commun.* **6**, 8892 (2015).

161. Acun, A. et al. *J. Phys. Condens. Matter* **27**, 443002 (2015).

List of publications

Peer-reviewed journal papers

1. Zeyuan Ni, Emi Minamitani, Yasunobu Ando, Satoshi Watanabe, "The electronic structure of quasi-free-standing germanene on monolayer MX (M= Ga, In; X= S, Se, Te)", *Physical Chemistry Chemical Physics*, 17, 19039-19044, 2015

2. Kazuaki Kawahara, Zeyuan Ni, Ryuichi Arafune, Tetsuroh Shirasawa, Chun-Liang Lin, Emi Minamitani, Satoshi Watanabe, Maki Kawai, Noriaki Takagi, "Surface structure of novel semimetal WTe_2", *Applied Physics Express*, 10, 045702, 2017

3. Zeyuan Ni, Emi Minamitani, Yasunobu Ando, Satoshi Watanabe, "Germanene and stanene on two-dimensional substrates: Dirac cone and Z_2 invariant", *submitted* (under peel view) 2017

International conferences

1. Zeyuan Ni, Emi Minamitani, Yasunobu Ando, Satoshi Watanabe, "Electronic Structure of Quasi-free-standing Germanene on Monolayer MX (M=Ga, In; X=S, Se, Te): Density Functional Calculations", NT15, 2015 June, Nagoya, Japan

2. Zeyuan Ni, Emi Minamitani, Yasunobu Ando, Satoshi Watanabe, "Theoretical study of the surface interaction between germanene and MX (M=Ga, In; X=S, Se, Te): towards germanene with Dirac-cone", ASIAN18, 2015 November, Kashiwa, Japan

3. Zeyuan Ni, Emi Minamitani, Yasunobu Ando, Satoshi Watanabe, "Theoretical study of the surface interaction between germanene and MX (M=Ga, In; X=S, Se, Te): towards germanene with Dirac-cone", SSVS 2015, 2015 December, Tsukuba, Japan

4. Zeyuan Ni, Emi Minamitani, Yasunobu Ando, Satoshi Watanabe, "Theoretical Search for Suitable Substrates of Germanene and Stanene: Towards the Dirac-cone and Practical Application", GRC: Two Dimensional Electronics Beyond Graphene, 2016 June, South Hadley, USA

5. Zeyuan Ni, Emi Minamitani, Yasunobu Ando, Satoshi Watanabe, "Germanene and stanene on 2D substrates: Dirac-cone and Z2 invariant", ASIAN19, 2016 November, Hsinchu, Taiwan

6. Zeyuan Ni, Emi Minamitani, Yasunobu Ando, Satoshi Watanabe, "Germanene and stanene on 2D substrates: Dirac-cone and Z2 invariant", CNT25, 2016 November, Tokyo, Japan

7. Zeyuan Ni, Emi Minamitani, Yasunobu Ando, Satoshi Watanabe, "Germanene and stanene on 2D substrates: Dirac-cone and Z2 invariant", SSVS 2016, 2016 November, Nagoya, Japan

Acknowledgement